Bulletin of Romanian Chemical Engineering Society

2 2025

ISSN 2360-4697
Edited by SICR and Matrix Rom
The journal is included in the international database
EBSCO, PROQUEST & INDEX COPERNICUS

ISSN 2360-4697

Bulletin of Romanian Chemical Engineering Society

Volume 12 2025 Number 2

Contents

SYNERGISTIC MIXTURES OF GREEN CORROSION INHIBITORS FOR STEEL ANTICORROSION COATINGS

Ioana MAIOR[1],·Elena-Alexandra DUȚĂ[2,*], Emilia-Ioana TOMA[2], Anca COJOCARU[1], Ioana-Alina CIOBOTARU[1]

[1] Department of Inorganic Chemistry, Physical-Chemistry & Electrochemistry, Faculty of Chemical Engineering and Biotechnologies, National University of Science and Technology POLITEHNICA Bucharest, 1–7 Gheorghe Polizu Str., 011061-Bucharest, Romania
[2] Faculty of Entrepreneurship, Engineering and Business Management, National University of Science and Technology POLITEHNICA Bucharest, 313 Independence Str., 060042-Bucharest, Romania

Abstract

Corrosion, a spontaneously natural process, affects metallic materials when interact with their environment; it is defined as the irreversible degradation of a metal due to chemical or electrochemical reactions with environmental factors (humidity, oxygen, salts, or acids). The objective of this work is to determine, through chemical and electrochemical methods, whether simple walnut hydroalcoholic extract (Junglas Regia JR) and in mixture with garlic extract (Allium Sativum AS), in various concentrations and ratios, could be efficiently used as inhibitor for carbon steel in corrosive acid environment. Thus, the experimental results suggest that investigated natural extracts of JR and AS acts on both partial reactions, anodic and cathodic. Based on corrosion rate evaluation by the gravimetric method, the efficiency of the simple inhibitors JR and AS, and respectively of the mixture of JR and AS, in different concentrations, in an acidic H_2SO_4 medium, on carbon steel was evaluated: the simple JR extract reaches a maximum effectiveness of 51.56% for the concentration of 500 µL, at 24 hours immersion time, respectively 77.95% for AS, while the mixture of JR : AS, at a ratio of 1000: 1000 µL, increases to an efficiency value of 85.51%.

Key words: corrosion, green plant extract, synergistic mixtures, steel, acid environment

1. Introduction

Corrosion process is a major challenge for all industries, and also for environmental protection, because it affects the safety of equipment and generates considerable economic losses annually. Consequently, current efforts to prevent and control corrosion are focused on two fundamental directions: the development of advanced monitoring methods (enable early detection and preventive intervention), and the adoption of sustainable protection solutions (use of eco-friendly corrosion inhibitors) [1-3].

Conventionally, synthetic inhibitors are used to stop corrosion, but many of these chemicals are hazardous, costly, and contaminate the environment. Although conventional inhibitors (inorganic compounds with chromium or various synthetic organic derivatives) can effectively reduce corrosion, the major disadvantage is the negative impact on the environment upon disposal. Increasingly stringent environmental

restrictions and health concerns have created the need to identify "green" alternatives – environmentally friendly, sustainable and safe inhibitors. Many natural products have been shown to be able to reduce the corrosion rate and are referred to as "green corrosion inhibitors". They have obvious advantages: environmentally friendly, less toxic to people and often more economical compared to synthetic inhibitors, being obtained from renewable sources [4-8].

In recent years, with the promotion of the concepts of "green chemistry", plant extracts have been intensively investigated as natural inhibitors due to their non-polluting character, wide availability and outstanding anti-corrosion properties. Essentially, plants provide a rich source of bioactive compounds – tannins, phenols, flavonoids, organic acids, alkaloids, catechins, terpenes, amino acids, polysaccharides, vitamins, etc. – that can act synergistically to protect metals from corrosion. Among these phytochemical classes, polyphenols (which include phenols and tannins) stand out particularly for their efficacy and low toxicity compared to other types of natural compounds (compared to some alkaloids). Thus, plant extracts rich in polyphenols meet many of the requirements of an ideal inhibitor, combining efficiency with ecological safety [9-13].

This experimental study involves specific electrochemical techniques based on weight loss measurements, in order to evaluate the corrosion rates and inhibition efficiency values, for single and synergistic mixtures of hydroalcoholic plant extracts (JR, AS). The investigations focused on comparing the effectiveness of both eco-friendly corrosion inhibitors, single and in mixtures, in protecting carbon steel immersed in acid solution. The aim was to quantify the reduction in the corrosion rate of steel under the action of these extracts and to compare the performance of the inhibitors, revealing the level of protection provided by the tested natural inhibitors and identifying the optimal usage conditions.

2. Experimental

Reagents

The chosen green corrosion inhibitors (JR, AS, and their mixture) have been used as natural plant extracts in aqueous solution of ethyl alcohol (75% vol.), version considered optimal from the point of view of polyphenols and organosulfur compounds solubility. Commercial hydroalcoholic vegetable extracts from local producers (PlantExtract and Dacia Plant, respectively) were used in experimental tests.

The walnut pulpy leaves and peels contain naphthoquinone (juglon) derivatives, flavonoids, tannins, small amounts of essential oil, and vitamin C [14]. The garlic pulp contains moderate amounts of Se, Ca, Mg, Mn, Fe, vitamins A, B and C, also K, Zn, S and P in substantial concentrations. The main bioactive components are polyphenols (apigenin, luteolin, kempferol derivatives), enzymes (myrosinase, alinase, peroxidase), polysaccharides, saponins, tannins, linalool, geraniol, fellandrene, b-felandrene, ajoene, aliin, and b-felandrene [15].

The experimental determinations were performed at a constant temperature of 25 ± 0.1°C.

Electrochemical methods

In order to evaluate the corrosion rate and the inhibition efficiency of the natural plant extracts investigated, the gravimetric method of metal samples weight loss was used, after a certain exposure time in the corrosion environment. The experiment was carried out with carbon steel metal samples, having an active surface area of 12.75 cm^2, in 1N H_2SO_4 acid solutions, with and without natural inhibitor, simple (50, 100, 500 and 1000 µL respectively) or in mixtures of different proportions (50+10, 100+40, 500+400 and 1000+1000 µL respectively). Prior to immersion in the corrosive environment, the steel plates were pre-treated by mechanical cleaning with abrasive paper, chemical degreasing with sodium carbonate, washing with water and distilled water, then drying with filter paper and weighing the initial mass with a precision analytical balance.

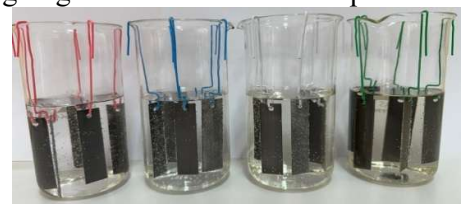

Fig. 1. Experimental set-up for the gravimetric method, at the beginning of the experiment for simple extracts of JR, AS and the mixture of JR + AS

Electrochemical studies were performed with a Voltalab 40 potentiostat/galvanostat (Radiometer Analytical), interfaced with a computer, which uses VoltaMaster 4.0 software for data acquisition and processing. A double-walled glass three-electrode electrochemical cell was used. Before each polarization experiment, the steel working electrode (WE) surface (area 0.50 cm^2) was polished with abrasive paper, washed with distilled water and dried. The counter electrode (CE) was a platinum sieve (area 2.5 cm^2), and the reference electrode (RE) was a saturated Ag/AgCl electrode, immersed directly in the working solution. All electrode potentials were measured with respect to this reference electrode.

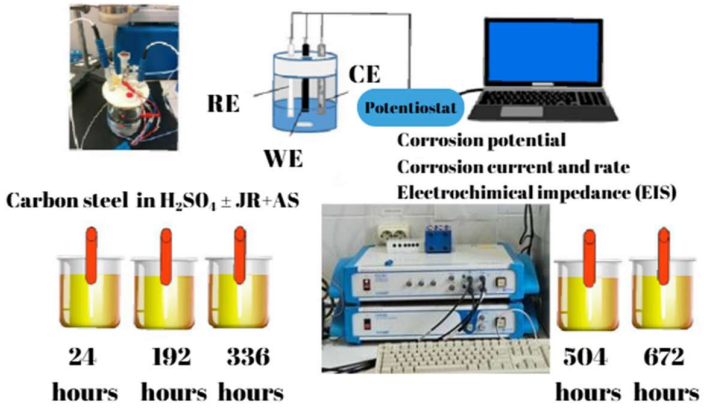

Fig. 2. The stages of the experimental process used for electrochemical techniques: installation for the gravimetric method with vessels for immersing metal samples in acid solution; the electrochemical cell and the equipment used for potentiometric methods [6]

3. Results and discussions

According to the data calculated from Table 1 and based on the resulting curves from Figure 3, the corrosion rates, expressed as penetration indices, decrease sharply in the first 14 days for the control solution and for the lower concentrations of inhibitor mixtures, while at high concentrations and proportions they tend to increase slightly. Then, in the following weeks, the corrosion rates tend to decrease slightly for all tested inhibitor concentrations, reaching a constant value.

Table 1.

Efficiency of natural inhibitors on steel corrosion in acidic environment: comparison between simple extracts of JR, AS and the mixture of JR + AS, depending on the exposure time

H_2SO_4 + JR, µL	Inhibitor efficiency, EI, %	H_2SO_4 + AS, µL	Inhibitor efficiency, EI, %	H_2SO_4 + JR + AS, µL	Inhibitor efficiency, EI, %	Time, h
500	51.56	**500**	77.95	**500 (+400)**	78.81	24
	11.32		27.17		51.38	192
	4.91		2.11		25.08	336
	2.16		10.30		12.25	504
	6.69		4.56		11.18	672
1000	48.71	**1000**	84.93	**1000 (+1000)**	85.51	24
	23.65		50.20		66.17	192
	3.06		7.96		42.71	336
	1.84		7.51		27.92	504
	3.61		2.41		25.32	672

The inhibition efficiency values for both types of simple JR and AS extracts increase with increasing inhibitor concentration, but decrease significantly with increasing immersion time. For any of the concentrations of the inhibitor mixture, a significant increase in protective efficiency is observed compared to the use of simple extracts, which shows the synergistic nature of the inhibitor mixture.

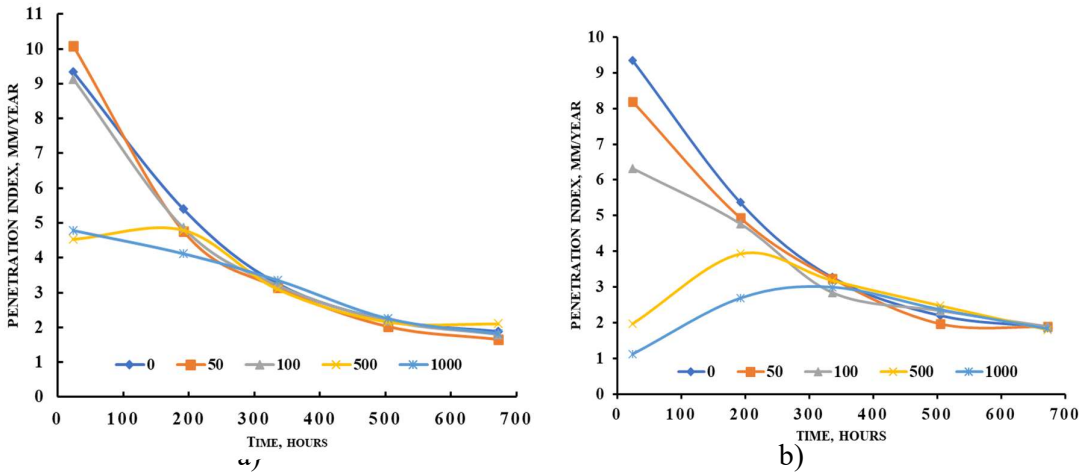

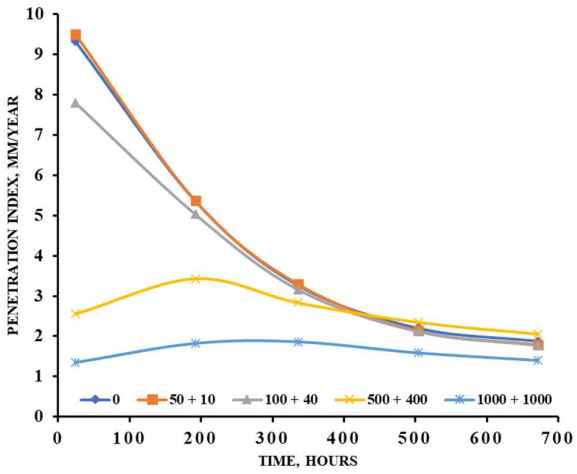

Fig. 3. Evolution of the penetration index as a function of immersion time, for different concentrations of extract (50, 100, 500 and 1000 µL respectively), compared to the control solution of acid without inhibitors: a) JR, b) AS, c) JR and AS mixture in different ratios (50+10, 100+40, 500+400 and 1000+1000 µL)

As noticed from Figure 4, regarding the appearance of solutions with mixtures of inhibitors of different concentrations of JR and AS (50+10, 100+40, 500+400 and 1000+1000 µL respectively), an important change can also be observed at the end of the experiment compared to the initial moment: the change of color of the corrosive medium and the appearance of a reddish-brown precipitate, most likely due to the formation of corrosion products, in varying quantities. Exceptions are the solutions of mixtures with high concentrations and proportions with JR and AS (500+400 and 1000+1000 µL respectively), which are clearer and more transparent, having a clearly different color, which suggests the absence of precipitation of corrosion products.

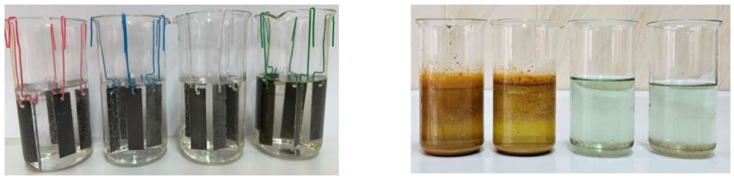

Fig. 4. Experimental set-up for the gravimetric method, at the initial and final time for the JR+AS inhibitor mixture, at different concentrations (50+10, 100+40, 500+400 and 1000+1000 µL)

In Figure 5 you can visually see the change in the appearance of the steel metal samples immersed in the corrosive medium, a continuous degradation as the immersion time increases from 24 hours to 4 weeks.

4. Conclusions

There are numerous monitoring and prevention anticorrosion methods applied to metals, among them the most used is adding inhibitor compounds, whether classic or ecological. The latter are becoming increasingly popular and have also begun to be used on an industrial scale. The advantages of these ecological inhibitors are: non-toxicity to humans, flora or fauna because they come from natural sources, raw material costs can be reduced by using biomass or plant parts that would have been discarded, biodegradability, due to their easily decomposition in the environment without leaving toxic or persistent residues.

Following the determination of the corrosion rate of the tested inhibitors, the gravimetric method evaluated the efficiency of the simple ecological inhibitors JR and AS, and the mixture of JR and AS, respectively, in different concentrations, in an acidic H_2SO_4 medium, on carbon steel samples: the simple JR extract constitutes a good inhibitor, reaching a maximum efficiency of 51.56% for the concentration of 500 µL, obtained at an immersion time of 24 hours, while the JR:AS mixture, at a ratio of 1000:1000 µL, achieves a superior efficiency of 85.51%.

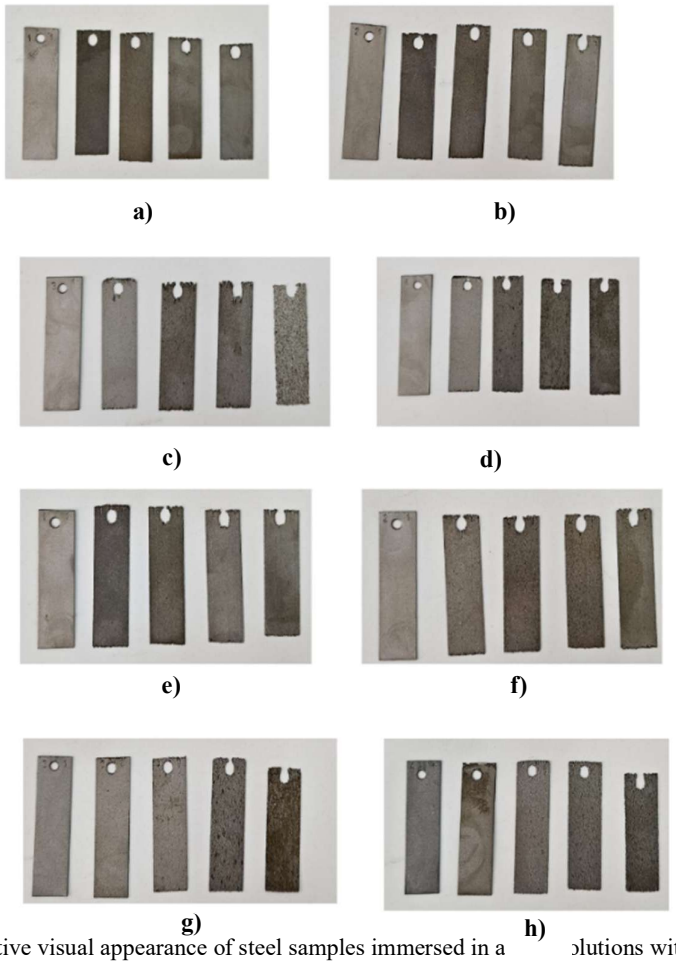

Fig. 5. Comparative visual appearance of steel samples immersed in a ɔlutions with different concentrations of JR and AS at the end of the experiment: (a) JR 50, (b) JR 100, (c) JR 500, (d) JR 1000, (e) JR+AS 50+10, (f) JR+AS 100+40, (g) JR+AS 500+400, (h) JR+AS 1000+1000

When mixing corrosion inhibitors in different proportions, three effects can be obtained: additivity, synergism or antagonism. Many inhibitors in the mixture do not behave according to the rule of additivity, but show an increase or decrease in the individual effects, which do not depend on the amount of inhibitor added. Natural walnut extract JR acts as an effective inhibitor, due to its polyphenolic compounds that can adsorb on the metal surface and form a protective film. The addition of garlic extract AS, rich in organosulfur compounds, enhances the inhibitory effect, by providing additional active compounds, with the possibility of a synergistic effect. In conclusion, a protective film is formed on the electrode surface, by the adsorption of organic compound molecules from the composition of the natural extract. The adsorption of inhibitors to the metal surface can affect the corrosion rate in two ways: by decreasing the active surface of the tested metal, due to the geometric blocking effect or by modifying the activation energy of the anodic / cathodic reactions.

REFERENCES

[1] Saxena, A., Prasad, D., Haldhar, R., Singh, G. & Kumar, A., Use of Saraca ashoka extract as green corrosion inhibitor for mild steel in 0.5 M H_2SO_4, *J. Molecular Liquids*, 258, (2018), 89–97

[2] Haldhar, R., Prasad, D. & Saxena, A., Armoracia rusticana as sustainable and ecofriendly corrosion inhibitor for mild steel in 0.5M sulphuric acid: Experimental and theoretical investigations, *Journal of Environmental Chemical Engineering*, 6, (2018), 5230–5238

[3] Dehghani, A., Bahlakeh, G., Ramezanzadehb, B. & Ramezanzadeh, M., Potential of Borage flower aqueous extract as an environmentally sustainable corrosion inhibitor for acid corrosion of mild steel: Electrochemical and theoretical studies, *J. Molecular Liquids*, 277, (2019), 895–911

[4] ElShami, A.A., Bonnet S., Makhlouf M. H., Khelidj A. & Leklou N., *Novel green plants extract as corrosion inhibiting coating for steel embedded in concrete*, Pigment & Resin Technology, Emerald Publishing Limited, (2020), pp. 501–514

[5] Subhajit Kundu, Mahuya Das, Debarati Mitra, *Current Status, Opportunities and Challenges of Green Corrosion Inhibitors* (Chapter 1) in Sustainable Corrosion Inhibitors, Materials Research Foundations, 107 (2021) p. 1-29, https://doi.org/10.21741/9781644901496-1.

[6] Payal, R. and Jain, A., *Green Corrosion Inhibitors for Coatings* (Chapter 7) in Sustainable Corrosion Inhibitors, Materials Research Forum LLC 107 (2021), pp. 147–174

[7] Kundu, S., Das, M., Mitra, D., *Green Corrosion Inhibitors from Biomass and Natural Sources* in Sustainable Corrosion Inhibitors, Materials Research Forum LLC 107 (2021), pp. 46–69

[8] Shaymaa Abbood Hussein, Anees A. Khadom, Okra leaves extract as green corrosion inhibitor for steel in sulfuric acid: Gravimetric, electrochemical, and surface morphological investigations, *Results in Chemistry*, vol. 8, (2024), 101566, https://doi.org/10.1016/j.rechem.2024.101566

[9] Singh, Ambrish, Ebenso, Eno E., Quraishi, M. A., Corrosion Inhibition of Carbon Steel in HCl Solution by Some Plant Extracts, *International Journal of Corrosion*, (2012), 897430, 20 pages

[10] B.A. Abd-El-Nabey, M.E. Mohamed, A.M. Helmy, H. Elnagar, A.M. Abdel-Gaber, Eco-friendly corrosion inhibition of steel in acid pickling using Prunus domestica Seeds and Okra stems extracts, *Int. J. Electrochem. Sci.*, 19 (8), (2024), 100695

[11] Obot, I.B., Ebenso, E.E. & Gasem, Z.M., Eco-friendly corrosion inhibitors: Adsorption and inhibitive action of ethanol extracts of Chlomolaena Odorata L. for the corrosion of mild steel in H_2SO_4 solutions, *International Journal of Electrochemical Science*, 7, (2012), pp.1997–2008

[12] Deng, S., Li X., Inhibition by Ginkgo leaves extract of the corrosion of steel in HCl and H_2SO_4 solutions, *Corrosion Science*, 55, (2012), pp.407–415

[13] Li, X., Deng, S., Fu, H., Inhibition of the corrosion of steel in HCl, H_2SO_4 solutions by bamboo leaf extract, *Corrosion Science*, 62, (2012), pp.163–175

[14] Mohammad Akbari Shahmirzadi, Mahboobeh Azadi, A new study on the corrosion inhibition

mechanism of green walnut husk extract as an agricultural waste for steel protection in HCl solution, *Heliyon*, 10 (9), (2024), e29962, https://doi.org/10.1016/j.heliyon.2024.e29962
[15] Afia L., Benali O., Salghi R., Ebenso E.E., Jodeh S., Zougagh M., Hammouti B., Steel Corrosion inhibition by acid garlic essential oil as a green corrosion inhibitor and sorption behavior, *Int. J. Electrochem. Sci.*, 9 (2014) 8392-8406

PRELIMINARY STUDY REGARDING THE ETHANOL PRODUCTION FROM A MIXTURE OF BANANA, ORANGE AND MELON PEEL

Estera VASILESCU[1], Alexandru-Cristian VÎLCICĂ[1], Edna Adriana ANTON[1], Gabriel-Marius CIOROIU[2], Liviu-Constantin STAN[2] and Doinița-Roxana TÎRPAN[1]*

[1] *Ovidius University of Constanta, Chemistry and Chemical Engineering Department, 124 Mamaia Blvd., 900527, Constanta, Romania*
[2] *Faculty of Naval Electromechanics, Department Electromechanics, Constanta Maritime University, 104 Mircea cel Batran Blvd, 900663, Constanta, Romania*

Abstract

*Bioethanol represents the biofuel extracted from biomass or from the biodegradable part of vegetable wastes. It can completely replace gasoline, more successfully than biomethanol, a solution adopted in some countries with high sugarcane production but the carbureted engine must be modified. Our study is focused on the production of second generation bioethanol from fruit waste, namely orange (Citrus sinensis), banana (Musa acuminate) and melon (Cucumis melo var. cantalupensis) peel. The process protocol was divided in three steps: physical pretreatment of the fruit peel, acid hydrolysis and anaerobic fermentation. A low-concentration acid hydrolysis (H_2SO_4, 1%) was followed by an anaerobic fermentation with Saccharomyces cerevisiae. Then, the fermented hydrolysate was introduce in a distillation apparatus. In order to investigate the effects of process factors (temperature, t; solid-to-liquid ratio, S; sulfuric acid concentration, c) a 2^3 factorial experiment was designed. The maximum yield of bioethanol obtained was **0.0912 g ethanol/g DM** proving that is a viable alternative method in biofuel production.*

Key words: fruit peel, hydrolysis, fermentation, ethanol

1. Introduction

The planet is experiencing significant global warming mainly due to the extensive use of fossil fuels [1]. The global economy relies on multiple fossil energy sources—such as oil, coal, and natural gas—which are predominantly utilized for electricity generation, transportation and industrial operations. This fuels are valuable due to their high chemical energy content and their relative ease of transportation and storage. Despite their contribution to economic development, fossil fuels entail severe environmental impacts that continue to be a major focus of global discussion [2].

Nevertheless, the combustion of fuels generates multiple greenhouse gases (GHGs), such as carbon dioxide (CO_2), carbon monoxide (CO), various sulfur and nitrogen oxides [3]. This has stimulated significant advancements in scientific research focused on biofuel products. One potential approach to enhancing energy security involves the development of bioethanol as either a substitute for gasoline or a blended

fuel, with mixing ratios of 5%, 10%, and 15%—commonly referred to as E5, E10, and E15, respectively [4]. In Romania, the maximum volumetric concentration of bioethanol in commercially distributed gasoline is set at 8%.

Bioethanol represents the biofuel extracted from biomass or from the biodegradable part of vegetable wastes which can be obtained through different conversion technologies [2, 5, 6]. Feedstocks can be categorized into four main groups:

- fermentable mono- and disaccharides, such as glucose and sucrose;
- starchy materials containing high amounts of starch;
- lignocellulosic biomass, primarily composed of 40–60% cellulose, 20–40% hemicellulose, and 15–25% lignin;
- algal biomass, which contains both starch and cellulose.

In terms of production pathways, sugar- and starch-based feedstocks are associated with the first-generation biofuels, which relies on edible biomass. Lignocellulosic biomass corresponds to the second-generation biofuels and is derived from abundant, renewable and nonedible plant materials. Algae have emerged as source for a promising third-generation biofuels attracting significant global research interest [2, 7].

This renewable biofuel has a small calorific power, an octane number 111 and freezing point -114 °C. It can completely replace gasoline, more successfully than biomethanol, a solution adopted in some countries with high sugarcane production like Brazil but the carbureted engine must be modified. Also, bioethanol can partially replace gasoline in countries with high bioethanol production from cereals [8].

Our work is focused on the production of second generation bioethanol from fruit waste, namely orange (*Citrus sinensis*), banana (*Musa acuminate*) and melon (*Cucumis melo var. cantalupensis*) peel. Figure 1 illustrates the visual representation of the sample origins, corresponding to (a) *Citrus sinensis*, (b) *Musa acuminata*, and (c) *Cucumis melo* var. *cantalupensis*.

The choice of this mixture is based on the fact that it is a relatively accessible biomass, it does not compete with other industries and it has reasonable amounts of sugars to be treated: orange peel (2,3% glucose, 3,5% sucrose, 2,7% fructose), banana peel (4% glucose, 6% sucrose, 2,7% fructose), melon waste (1% glucose, 5% sucrose, 2% fructose). However, the carbohydrates content of fruits peel is not uniform and depends on several factors: variety, degree of maturity and growing conditions [9].

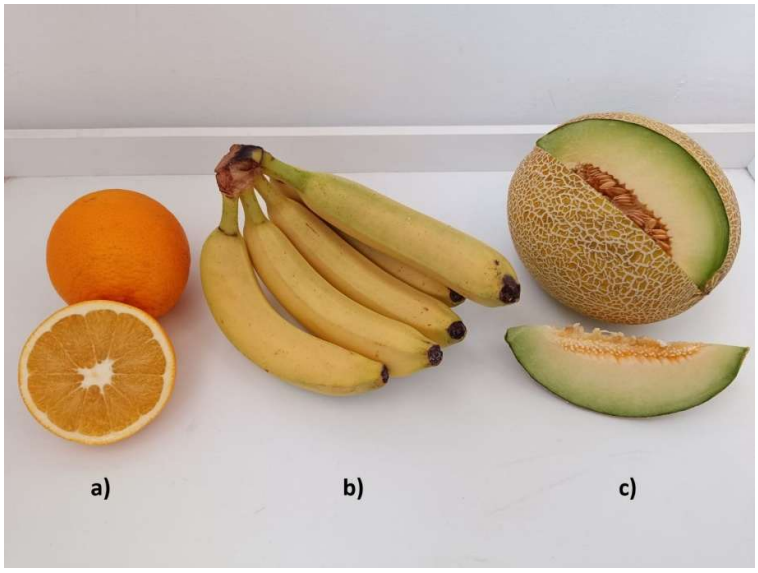

Fig. 1. Visual representation of the sample origins (a- *Citrus sinensis;* b) *Musa acuminate;* c) *Cucumis melo var. cantalupensis)*

2. Experimental

2.1. Origin of the samples

The samples that were subjected to analysis and transformation consists in a mixture of orange (*Citrus sinensis*), banana (*Musa acuminata*), and melon (*Cucumis melo var. cantalupensis*) peel. The fruits were all purchased from local markets and are of local origin (Romania). The waste was generated in our houses over a period of approximately 2 weeks and is the consequence of the direct use of the fruits. The sampling procedure was quite elementary: for the oranges and bananas we manually detached the peels, whilst for the melon we used primary kitchen cutlery in order to extract the peel, along with a part of the flesh that was not desired for consuming.

2.2. Physical pretreatment

The D.M. content was determined with the OHAUS thermobalance, model MB45, also called humidity analyzer (Figure 2). This was programmed at 180°C for 14 minutes, for wood plants, as recommended by the supplier. The mass loss of the sample allows the determination of moisture content.

Fig.2. OHAUS thermobalance (moisture analyzer)

In our process protocol, the physical treatment was divided in 3 steps: cutting the fruit peels into smaller pieces, thermically treating them in a drying oven, and grinding them into smaller pieces with an electrical chopper. The reasoning for the initial step is obvious, as it helped us manipulate the biomass easily, whilst the following steps are meant to partially deconstruct the lignocellulose into less complex substances, such as cellulose, hemicellulose and lignin.

The thermal treatment occurred at a temperature of 150 ºC for 180 minutes, time in which the biomass was observed and checked several times, in order to prevent over-cooking, procedure that could have damaged the sugar contents of the peels, therefore interfere with the yield of our next processes. The grinding was not particularly controlled, as we did not look for an exact measurement of the particles. The consistency and color obtained was similar to the one of coarse coffee grounds, as the smell of it was citrous, tangy, slightly sweet and astringent.

2.3. Acid hydrolysis

In order to perform the acid hydrolysis process, we mixed 40g of pretreated biomass with 200 ml of 1% sulfuric acid solution (v/v) into an Erlenmeyer flask. After thoroughly mixing, we introduced the product into an autoclave at a temperature of 120ºC for 30 minutes [10, 11]. The next step was to wait for the mixture to cool down and separate the solids from the liquids. After that, we washed the liquid with distilled water and dried it into an oven. The hydrolysate (the liquid) was then subjected to a pH

adjustment, to make sure that we will have a safe medium to add the yeast for the following step, the fermentation. The desired pH is around 5.

a. Anaerobic fermentation

In the fermenter we added the hydrolysate and *Saccharomyces cerevisiae* (using 80g of yeast/ L of hydrolysate). We let the fermentation occur at 30 ºC for around 24 hours. The principle of the fermentation was to expose the carbohydrates to anaerobic conditions and determine the amount of ethanol produced by measuring the amount of CO_2 formed. The fermentation reaction is briefly presented below [12].

$$\underset{\text{Glucose/Fructose}}{C_6H_{12}O_6} \longrightarrow \underset{\text{Ethanol}}{2C_2H_5OH} + \underset{\text{Carbon dioxide}}{2CO_2\uparrow}$$

b. Statistical model

We can assume that the process efficiency is predominantly **influenced by** three variables: suspension concentration, sulfuric acid concentration and fermentation temperature. In order to investigate the effects of process factors, a 2^3 factorial experiment was designed. The factors studied were: the solid-to-liquid ratio (S = 1/5 and 1/10 wt.), sulfuric acid concentration (c= 0.5% and 1%) and alcoholic fermentation temperature (t=20 and 30 ºC). The yield of ethanol was considered the response.

3. Results and discussions

At the time of the experiment, the biomass mixture has a moisture content of $83.72 \pm 0.5\%$ (w/w) based on dry matter (DM). Quantitative yields of ethanol, normalized to dry matter (g/g DM), are summarized in Table 1.

Table 1.

Ethanol yields obtained in the alcoholic fermentation from *Citrus sinensis; Musa acuminate and Cucumis melo var. cantalupensis)*

Exp	Temperature t, ºC	Solid-to-liquid ratio S, wt.	Sulfuric acid conc., c, %	Ethanol yield, E, g/g DM	Predicted y, E, g/g DM
1	20	1/5	0.5%	0.0482	0.0479
2	20	1/5	1%	0.0525	0.0527
3	20	1/10	0.5%	0.0437	0.0440
4	20	1/10	1%	0.0457	0.0455
5	30	1/5	0.5%	0.0862	0.0864
6	30	1/5	1%	0.0912	0.0909
7	30	1/10	0.5%	0.0832	0.0829
8	30	1/10	1%	0.0840	0.0842

According to the data presented in **Table 1**, the ethanol yield increased under higher fermentation temperatures (t=30 °C), lower solid-to-liquid ratios (S=1:5 w/w) and elevated concentrations of sulfuric acid (c=1%). Under these conditions, the maximum ethanol yield reached **0.0912 g ethanol/g DM,** corresponding to **9.12 kg ethanol per 100 kg dry biomass.**

Data processing and statistical analysis were conducted using the **Microsoft Excel** regression tools. The polynomial model describing ethanol yield as a function of the process parameters is given in **Equation 1:**

$$y = -0.0346 + 0.0038t + 0.0149S - 0.0013c + 0.0453S * c \quad \text{(Eq.1)}$$

For Eq.1, the correlation coefficient r^2 was 0.982, adjusted r^2 was 0.963 and the standard error was 0.0021. ANOVA revealed the null hypothesis rejection ($p < 0.05$) for all coefficients in Eq.1. Predicted yields according to the mathematical model are presented in Table 1, showing a good fitting with the experimental values.

4. Conclusions

Fruit waste valorization has proven to be a viable option for second-generation bioethanol production, offering a sustainable alternative to conventional starch- or sugar-based feedstocks. The mixture of orange, banana and melon peels represents an accessible, renewable raw material that does not compete with the food industry.

The **technological protocol** applied—consisting of physical pretreatment, dilute acid hydrolysis (H_2SO_4 1%) and anaerobic fermentation using *Saccharomyces cerevisiae*—enabled an efficient conversion of carbohydrates from fruit biomass into ethanol, demonstrating the feasibility of the process at laboratory scale.

The **2^3 factorial experimental design** confirmed the significant influence of the three main factors—fermentation temperature, solid-to-liquid ratio and sulfuric acid concentration—on the final ethanol yield. The optimal conditions were temperature, t= 30 °C, a S=1:5 (w/w) solid-to-liquid ratio and 1% sulfuric acid concentration. The **maximum ethanol yield** obtained, 0.0912 g ethanol/g dry matter (equivalent to 9.12 kg ethanol per 100 kg biomass), demonstrates the efficiency of the proposed method and supports the potential of fruit peel waste as a promising feedstock for sustainable biofuel production. The **statistical model developed** ($r^2 = 0.982$) showed a strong correlation between the experimental and predicted values, confirming the reliability of the mathematical approach for yield prediction as a function of process parameters.

Overall, the study highlights that **bioconversion of fruit waste into bioethanol** can contribute to reducing greenhouse gas emissions and improving organic waste management, representing a concrete step toward a **circular and sustainable bioeconomy**.

REFERENCES

[1] Shedrack T.M., Lewis A.M., Jovine Kamuhabwa E., Bioethanol production from pineapple fruit waste juice using bakery yeast, *Helyon,* 10, (2024), e38172.
[2]. Cesar Guimaraes C.E., Neto F.S., Castro Bizerra V., Andrade do Nascimento J.G., Valerio R.B.R *et al.*, Sustainable bioethanol production from first- and second-generation sugar-based feedstocks: Advanced bibliometric analysis, *Bioresource Technology Reports*, 23, (2023), 101543.
[3] Singh P., Kiran U., Ghosh S., Repeated batch fermentation of xylose-rich hydrolysate obtained from wheat straw in a bioreactor to produce second-generation bioethanol*, Fuel*, 387 (2025), 134383.
[4] Setiawan H., Hermawan E., Adiarso A., Setiadi S., Saputra H. *et al.,* Optimized supply chain of empty fruit bunches as feedstocks for second generation bioethanol production, *Case Studies in Chemical and Environmental Engineering*, 10, (2024), 100950.
[5] Demiray E., Karatay S.E., Deonmez G., Evaluation of pomegranate peel in ethanol production by *Saccharomyces cerevisiae* and *Pichia stipitis*, Energy, 159, (2018), 988e994.
[6] Arun K.B., Madhavan A., Anoopkumar A.N., Surendhar A., Kuriakose L.L. *et al.,* Integrated biorefinery development for pomegranate peel: Prospects for the production of fuel, chemicals and bioactive molecules, *Bioresource Technology,* 362, (2022), 127833.
[7] Dhande D.Y., Nighot D.V., Sinaga N., Dahe K.B, Extraction of bioethanol from waste pomegranate fruits as a potential feedstock and its blending effects on a performance of a single cylinder SI engine, *Renewable and Sustainable Energy Reviews,* 149, (2021), 111349.
[a] Tîrpan D-R., *Combustibili alternativi. Caiet de studiu individual,* Ovidius University Press, ISBN 978-606-060-112-8, Constanţa, (2024), 1-84.
[b] Shilpa C., Girisha M. and C., Alcohol Production from Fruit and Vegetable Wast, *International Journal of Applied Engineering Research*, 8, No 15, (2013), 1749-1756.
[c] Jacqueline P.J., Velvizhi G., Substantial physicochemical pretreatment and rapid delignification of lignocellulosic banana, pineapple and papaya fruit peels: A study on physical-chemical characterization, *Sustainable Chemistry and Pharmacy*, 37, (2024), 101347.
[d] Mgei S. T., Mero H. R., Mtashobya L. A., Emmanuel J. K., Utilizing fruit wastes as a sustainable feedstock for bioethanol production: A review, *Cleaner Energy Systems,* 10, (2025), 100188.
[e] Mgei S. T, Mtashobya L. A, Emmanuel J. K., Bioethanol production from fruit wastes juice using millet and sorghum as additional fermentable sugar, *Cleaner Energy Systems*, 10, (2025), 100177.

CHARACTERIZATION AND ANALYTICAL IDENTIFICATION OF POLYAROMATICS FROM DIESEL FUEL

Bianca SIMEDREA[1*] Nicoleta-Oana DEMOSTENE[1], Iuliana DELEANU[1], Oana PARVULESCU[1], Olga SAPUNARU[2], Tănase DOBRE[1,3]

[1]National University of Science and Technology POLITEHNICA Bucharest, 1-7 Gheorghe Polizu Str., 011061 Bucharest, ROMANIA, [2]Universitatea Ovidius Constanta, 124 Mamaia Boulevard, 900527 Constanța, ROMANIA,[3]Technical Sciences Academy of Romania,26 Dacia Boulevard,030167 Bucharest, Romania

Abstract

In this study, different diesel fuel samples were analyzed to see the effects of polyaromatics on engine combustion compared to European standards. Different diesel fuel samples from HPM and HDV plants were evaluated over 60 days to observe the variation of the aromatics content in diesel fuel over a longer time. Period. The monitoring of polyaromatics was performed using the HPLC chromatographic method and plant operating parameters.

Key words: diesel, polyaromatics, chromatography, engine, exhaust emissions, industrial plants

1. Introduction

Polynuclear aromatic hydrocarbons (PAH) are compounds containing from 2 to 7 benzene rings. Known also as polycyclic aromatic hydrocarbons these constitute a class of organic compounds with condensed aromatic rings with various specific structures. Once in the environment, PAH are persistent and can take the form of microparticles, many of which are below 10 μm (PM 10). These PM 10 results especially from the combustion of fossil fuels.

Pyrogenic, petrogenic and biological processes are processes responsible for the generation of PAHs from organic materials

Pyrogenic PAHs are formed when organic matter is exposed to high temperatures (350 ^{0}C -1200 ^{0}C), in the absence of oxygen or in the presence of low amounts of oxygen. Thermal cracking of oil refineries, coal distillation, incomplete combustion of fuels in heating systems or in vehicle engines and also the incomplete combustion of forest wood are example in this sense.

Petrogenic PAHs are represented by crude oil, formed over millions of years at low temperatures (100–150^{0}C), but also PAHs formed during the transport, storage and use of crude oil or petroleum products, the accumulation of small quantities of oil, gasoline, motor oils and substances associated with transport activities, etc [1,2].

Biological PAHs occur in plant development as well as in the aerobic or anaerobic decomposition of biomass. Similarly, the combustion of plant materials produces, in low concentrations but structured as microparticles, such compounds

Other PAHs contains observations to the fact that new heterocyclic aromatic compounds (carbazoles, acridines), as well as derivatives of PAHs (nitro-PAHs and oxygenated PAHs) can be generated by incomplete combustion and chemical reactions occurring in

ambient air. These compounds occur together with PAHs in air, water and food, the total mixture being called polycyclic aromatic compounds (PAHs).
PAH in applications subject refers to the fact that some PAHs are used as raw materials in synthesis respectively processing of an lot of manufactured materials. Some examples are: i) acenaphthene in synthesis of one's specific pigments, dyes and pharmaceuticals products, ii) anthracene as important diluent for wood bio protection agents, iii) fluoranthene for manufacturing of some specific chemicals for use in agriculture, dyes and pharmaceuticals, iv) fluorene in temperature-resistant plastics, v) phenanthrene in synthesis of thermoresistant resins and ones pesticides.
PAH classification and attributes shows that depending on the number of benzene nuclei, PAHs are classified and presents ones from the bellow attributes, So we have: i)PAHs with low molecular weight, which are less than 4 aromatic nuclei in their structure, ii) PAHs with high molecular weight that have 4 or more aromatic nuclei in their structure, iii) PAHs with 2 or 3 nuclei namely naphthalene, acenaphthene, anthracene, fluorene, phenanthrene are present in the air, predominantly, as vapor phase, iii) PAHs with four nuclei as example, fluoranthene, pyrene, chrysene, etc. exist in environment in both the vapor and particle state, iv) PAHs with 5 or more aromatic rings, as benzo perylene example, are predominantly present in particulate form (PM), v) PAHs with smaller molecules namely benzene, toluene and naphthalene are not considered as true PAHs, v) PAH compounds considered the most potent carcinogens, extensively studied are 7,12-dimethylbenzoanthracene (DMBA) and benzo(a)pyrene (BaP) [1,2].
PAH and atmospheric pollution are strongly linked to the use of fuel in car engines of all sizes. Aromatics, mono ring, two rings and three rings in a diesel with a low sulfur content influence on the exhaust emissions of diesel engines [2, 3]. The current fuel is almost entirely supplied from the petrochemical sector, so the legislation is becoming stricter for minimal pollution and that has correspondence respect to accepted composition of petroleum fuels [3]. Contribution of aromatics to diesel exhaust emissions is evident. Simultaneous addition of mono ring, two rings and three rings' aromatics into low sulfur diesel fuel has different effect on engine emission. Reduction of aromatics content in diesel fuel contributes to decrease of microparticle (PM), hydrocarbons (HC) and nitric oxides (NO_x) emissions. The intensity of aromatics effect on emission is as follows: three rings > two rings+ >mono ring aromatics [2]. The Euro 5 diesel samples from the test batches contain polyaromatic values between 2 and 5 % mass. These values are within the norms imposed by the government. The value differs depending on the components used to obtain the finished diesel such as components from refinery sources (cracking, vacuum distillation, hydrodesulphurization) each having a different aromatic value. HC, PM, NOx emissions increase with the addition of all PAH types. PM emissions are the ones that increase more than HC and NOx. The most common values in the analyzed batches are those between 2% - 3 % mass polyaromatics, which is favorable because the content should be as low as possible [4, 5]. Due to the important environmental effects of PAHs, extensive studies have been carried out over the last few years concerning the concentrations of PAHs in the particulate and gas phases [6]. Most of these studies have focused on extraction and analysis techniques for the identification of PAHs adsorbed on particulate matte. In this context, although analytical methods for parent PAHs on soot are well known, there are relatively few studies in the case of derivatives. Due to the important environmental effects of PAHs, extensive studies have

been carried out over the last few years concerning the concentrations of PAHs in the particulate and gas phases [7]. Most of these studies have focused on extraction and analysis techniques for the identification of PAHs adsorbed on particulate matte. In this context, although analytical methods for parent PAHs on soot are well known, there are relatively few studies in the case of derivatives.

PAH and health. Diesel exhaust is a major source of traffic-related air pollution, of airborne PM in urban areas. The organic fraction of diesel exhaust particles (DEP) contains large quantities of polyaromatic contaminants, including PAHs, nitrated PAHs (nitro-PAHs) and oxygenated PAHs (oxy-PAHs), which have been suggested to contribute to the adverse health effects of DEP [5]. The genotoxic and non-genotoxic of DEP and their derivates action modes have been reported, including: i) generation of oxidative stress and consequent oxidative DNA damage or formation of DNA adducts, ii) induction of inflammatory responses or cell death, iii) aberrant activation of the aryl hydrocarbon receptor (AhR)-dependent gene, signaling linked with further toxic events. These effects can be associated with carcinogenicity and/or cell transforming activity of DEP-associated pollutants. Both gaseous and PM fractions of polluted air also contain significant amounts of compounds classified as endocrine disrupting chemicals (EDCs). Induction or repression of endocrine nuclear receptor-mediated gene expression is one the major modes of action associated with endocrine-disrupting processes. Nevertheless, the nuclear receptor-associated mechanisms contributing to endocrine-disrupting effects of the complex mixtures of aromatic compounds adsorbed to DEP remain mostly poorly characterized, although they have been shown to potentially interfere with the activities of estrogen (ER) and androgen (AR) receptors [5]. The aromatics work as a precursor of multiple toxic compounds of combustion emissions, and a reduction in aromatics has been connected to a decrease in emissions toxicity. Consequently, the concentration of aromatics is of high importance and so some auto fuels has been substituted with higher ethanol-gasoline or by mixture diesel-biodiesel. Fuels produced from non-fossil sources, such as biodiesel, have been shown to have in addition of low aromatics, no sulphur, higher oxygen content, and higher cetane numbers than fossil fuels. These properties all increase engine performance and decrease emission toxicity. Moreover, the fuels produced from non-fossil sources have lower greenhouse gas emissions than fossil fuels [7].

Given the environmental effects of the presence of polycyclic aromatic hydrocarbons in fuels, especially in diesel fuel, this paper presents a method for the routine analysis of their content in a produced fuel, coupled with the monitoring of the concentration dynamics of these PAHs in the HPM and HDV hydrogenation plants of a modern refinery.

2. Experimental

Different samples of Euro 5 diesel fuel, from different batches prepared for sale, were tested to see their aromatic content using HPLC chromatography. The chromatograph used is an Agilent HPLC 1260 liquid that uses 100% heptane as solvent with a flow rate of 0.8 - 1.2 ml/min. The column thermostat being set at 30 °C. The detector used is the refractive index at a temperature of 30 °C at a positive polarity.

The analytical procedure for PAH has been integrated into the monitoring of HPM and HDV installations in refineries. HPM processes blends especially of kerosene and light DA gas oil for standardized diesel fuels, used in diesel engines. HDV processes blends from heavy gas oil from DV, gas oil from catalytic cracking, DA gas oil and DAV kerosene.
In both installations, catalytic hydrogenation takes place at pressure and temperature of the processed mixture, so that sulfur compounds, nitrogen compounds, oxygen compounds, aromatics and olefins react with the hydrogen brought into the system from the gas phase.
In both monitoring cases, the independent variables were chosen as density of the hydrofined mixture (kg/m^3), crude diesel input flow rate (m^3/h), hydrogenation temperature (^{0}C), gas low rate (Nm^3/h) and sulphur concentration in reactor input (% mass) respectively as dependent variables (process response) the reactor product sulphur concentration (ppm), the density (kg/m^3) and PAH concentration (g/l)

3. Results and discussions

The purpose of the diesel hydrofining plant abbreviated as HPM, which use hydrogenation of is to: i) remove sulfur, nitrogen and oxygen compounds from the diesel fraction, olefinic and aromatic compounds, ii) improve the stability, color and combustion properties of the final product.
The result is low-sulfur diesel fuel (Euro 5 / Euro 6), in accordance with modern environmental standards. Respect to environment the advantages of the hydrorefining process is expressed by: clean diesel fuel with reduced SO_2 and particulate emissions, increased oxidative fuel stability, improved fuel cetane number, environmental protection and compliance with European standards. With reference to the HPM and HDV installations monitoring for PAH content in hydrofined diesel, it is specified that this monitoring was carried out for a period of 60 days, the same for both installations. Tables 1 and 2 contain, for size reasons, only 3 sequences from the total period, namely the first 6 days, then from day 30 to day 36 and respectively the last 6 days. All data are considered in the graphical representations given relative to these monitoring's. As mentioned above ρ_{in}, G_{vl}, t_r, G_{vg}, and respectively c_{Si} were considered as independent variables, whereas c_{Se}, ρ_{ie} and respectively c_{PAH} are process dependent variables. The notation X_i, i = 1, 6 (X_1 is ρ_{in}, X_2 is G_{vl} and so on) was adopted for independent variables and the notation Y_i, i = 1, 3 (Y_1 is ρ_{ie} and so on) for process dependent variable. Each of the variables X_i and Y_i are in fact random variables with a normal distribution respect to the frequency of their occurrence in the monitored data. Therefore for the present analysis they were normalized [8] using in this sense the relations (1) - (6) where X_{mi} and Y_{mi} respectively are the mean of the variance and s_{dXi} and s_{dYi} are the variable dispersion respect to the mean.

$$X_{ai} = \frac{X_i - X_{mi}}{s_{dXi}} \quad i = 1, 2 \dots 5 \tag{1}$$

$$Y_{ai} = \frac{Y_i - Y_{mi}}{s_{dYi}} \quad i = 1, \ 2, 3 \tag{2}$$

$$X_{mi} = \frac{\sum_{i=1}^{N} X_i}{N} \quad (3)$$

$$Y_{mi} = \frac{\sum_{i=1}^{N} Y_i}{N} \quad (4)$$

$$s_{dXi} = \left(\frac{\sum_{i=1}^{N}(X_i - X_{mi})}{N-1}\right)^{1/2} \quad (5)$$

$$s_{dYi} = \left(\frac{\sum_{i=1}^{N}(Y_i - Y_{mi})}{N-1}\right)^{1/2} \quad (6)$$

Table 3 contains the computed data regarding the mean and dispersion of the variables X_i and Y_i relating to the HPM processing plant, where the catalytic processes follow the desulfurization of the diesel sources above mentioned.

Figure 1 shows the state during the monitoring of the dimensionless variables X_{ai} and Y_{ai} for this plant. Since it is more difficult to follow the relationship between the dependent and independent variables, in Figures 2 and 3, the dependence Y_{ai} is versus X_{ai} was given.

Table 1.

Table for monitoring the status of polycyclic hydrocarbons in Petromidia diesel fuel - HPM

Day	Density Diesel input ρ_{in} Kg/m^3	Diesel input flow G_{vl} m^3/h	Reactor Temperat. t_r ^{0}C	Gas flow rate in reactor G_{vg} Nm^3/h	Sulfur conc. reactor inlet c_{Si} %	Sulfur conc. reactor exit c_{Se} ppm	Output diesel density ρ_{ie} Kg/m^3	PAH conc. c_{PAH} g/l
1	852.5	106.22	348.1	44710.4	0.99	6.82	838.9	5.8
2	847.4	128.38	355.1	43129.13	0.93	5.55	836.5	6.0
3	850.4	127.37	354.4	41926.09	0.98	7.22	838.2	5.2
4	850.8	127.54	353.2	41224.09	0.95	10.37	838.3	4.0
5	851.7	125.60	356.0	41172.5	1.14	10.33	838.6	4.0
6	850.7	125.01	356.6	41122.89	1.01	8.27	836.6	5.1
30	841.1	109.62	343.4	43370.02	1.25	9.77	829.6	4.3
31	840.3	101.88	339.5	42658.16	0.99	9.70	828.9	4.3
32	840.5	99.984	340.3	42704.33	1.00	10.93	828.8	4.2
33	840.1	100.01	339.7	42501.6	0.99	10.51	828.9	3.6
34	839.5	100.03	339.6	42354.27	0.97	11.65	828.3	3.4
35	840.8	100.03	339.9	42334.85	1.00	10.19	829.1	3.6
36	841	101.27	341.5	42706.21	1.02	10.79	828.7	3.6
54	844.8	130.00	352.0	44494.88	0.86	13.56	832.6	3.3
55	844.9	129.99	352.2	45196.29	0.96	13.62	832.8	3.2
56	842.5	130.00	351.6	44976.35	0.96	11.62	830.5	3.4
57	842.6	130.00	351.7	44919.3	0.91	12.78	830.7	3.3
58	840.3	130.00	350.7	41886.31	0.82	9.67	830.4	4.2
59	843.2	130.01	350.3	41994.4	0.87	12.91	831.2	3.6
60	839.8	130.01	349.0	42187.76	0.80	15.06	832.7	2.5

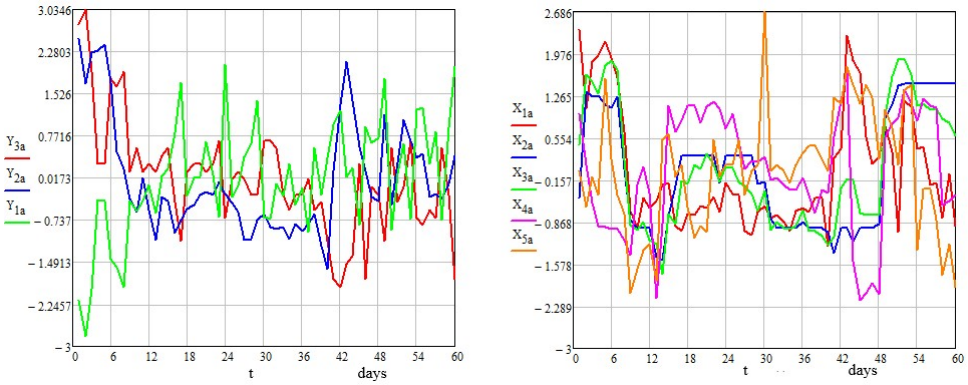

Fig. 1. Daily state of dimensionless variables Y_{ai} and X_{ai} respectively for HPM plant (Y_{a1}-normalized sulphur concentration in processed diesel, Y_{a2}-normalized density of processed diesel, Y_{a3} -normalized PAH concentration in processed diesel, X_{a1}-normalized density of crude diesel, X_{a2}- normalized reactor input crude diesel flow rate , X_{a3}-normalized temperature of hydrogenation reactions ,X_{a4}- normalized gas flow rate through reactor, X_{a5}-normalized sulphur concentration at reactor input)

Table 2.

Table for monitoring the status of polycyclic hydrocarbons in Petromidia diesel fuel- HDV

Day	Density Diesel input ρ_{in} Kg/m^3	Diesel input flow G_{vl} m^3/h	Reactor Temperat t_r ^{0}C	Gas flow rate in reactor G_{vg} Nm^3/h	Sulfur conc. reactor inlet c_{Si} %	Sulfur conc. reactors exit c_{Se} ppm	Output diesel density ρ_{ie} Kg/m^3	PAH conc. c_{PAH} g/l
1	851.1	142.0	313.8	52456.0	0.71	0.8	830.7	4.0
2	849.1	157.4	307.2	48169.1	0.70	1.4	828.8	3.5
3	847.6	171.2	304.4	48592.2	1.00	3.0	830.2	2.0
4	843.2	142.6	304.5	42073.3	0.81	5.5	835.8	2.5
5	847.3	140.0	303.5	42330.7	1.18	6.0	829.7	3.0
6	847.9	131.8	301.5	42265.7	1.18	6.0	831.4	3.0
30	862.5	146.9	306.8	89167.5	1.01	6.4	843.7	3.0
31	862.9	174.3	309.5	88341.4	1.00	6.6	842.2	3.3
32	858.9	175.0	310.3	91469.9	1.10	6.3	839.5	3.2
33	860.7	175.0	309.2	89183.2	1.00	5.1	840.1	2.7
34	859.8	175.8	308.4	88223.6	1.06	6.3	840.1	2.5
35	856.7	179.3	314.6	78680.8	1.06	7.1	839.5	1.5
36	864.2	155.4	314.9	86339.4	1.09	4.9	844.1	3.0
54	865.90	170.0	313.8	88467.7	1.18	6.4	844.2	2.4
55	866.00	55.9	196.0	77936.1	1.13	7.5	844.8	1.5
56	859.19	168.7	314.0	87450.8	0.92	23.4	844.4	0.8
57	856.20	169.4	314.6	90790.4	0.99	10.2	839.7	1.0
58	854.00	170.0	315.7	87650.2	0.72	4.3	838.5	3.0
59	857.90	169.8	314.1	88233.5	0.79	2.7	842.1	3.2
60	851.40	170.5	314.1	87509.1	0.78	3.1	841.2	3.1

$$cov(Y,X) = \frac{\sum_{i=1}^{n}(X-X_m)(Y_i-Y)}{N-1} \quad (7)$$

$$r_{YX} = \frac{\sum_{i=1}^{n}(X_i-X_m)(Y-Y_m)}{\sqrt{\sum_{i=1}^{n}(X-X_m)^2(Y-Y_m)^2}} = \frac{cov(Y,X)}{s_{dX}s_{dY}} \quad (8)$$

For a more complete characterization of the relationship between the PAH concentration variables in the product and the independent variables, the values of the covariance (7) and the correlation coefficient (8) were calculated. Table 4 presents the values obtained for the HPM installation.

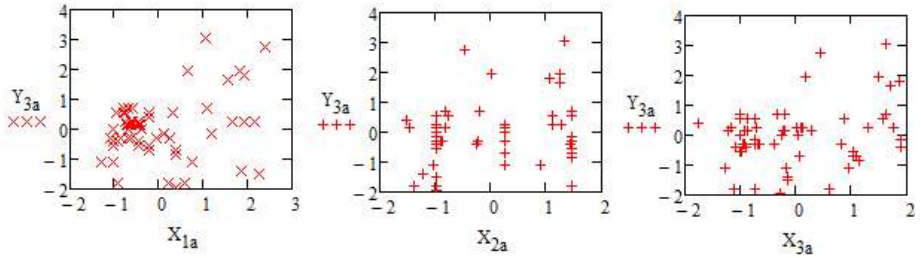

Fig. 2. Status of normalized PAH concentration according to normalized variables X_{a1} (normalized density of crude diesel), X_{a2} (normalized reactor input crude diesel flow rate) and X_{a3} (normalized temperature of hydrogenation reactions)

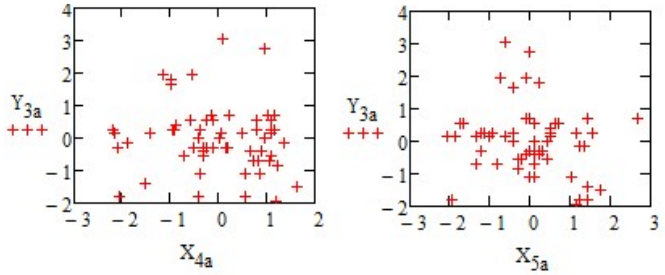

Fig. 3. Status of normalized PAH concentration (Y_{3a}) according to normalized variables X_{a4} (normalized gas flow rate) and X_{a5} (normalized sulphur concentration at reactor input)

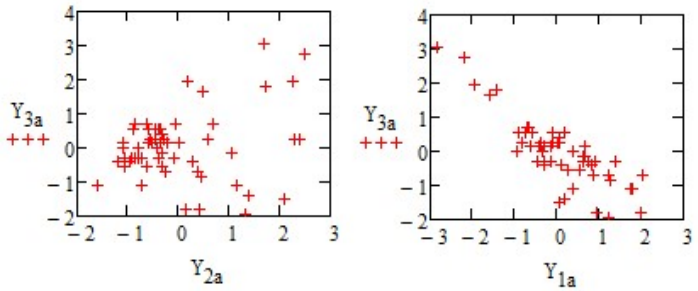

Fig. 4. Status of normalized PAH concentration (Y_{3a}) according to normalized variables Y_{a1} (normalized sulphur concentration in processed diesel) and Y_{a2} (processed diesel normalized density)

Table 3.

Mean and standard deviation of monitored variable from HPM plant

Variable	X_1	X_2	X_3	X_4	X_5	Y_1	Y_2	Y_3
m.u	Kg/m^3	m^3/h	^0C	Nm^3/h	% mass	ppm	Kg/m^3	g/l
Mean	843.4	111.9	345.5	$4.3\ 10^4$	0.99	11.1	831.4	3.81
Standard deviation	3.83	12.3	5.97	$1.85\ 10^3$	0.097	1.97	2.97	0.72

Table 4.

Covariance and correlation coefficient of Y_{3a} with normalized process variables from HPM plant

$cov(Y_{3a},X_{ia})$	$(Y_{3q}X_{1a})$	$(Y_{3q}X_{2a})$	$(Y_{3q}X_{3a})$	$(Y_{3q}X_{4a})$	$(Y_{3q}X_{5a})$	$(Y_{3q}Y_{1a})$	$(Y_{3q}Y_{2a})$
	0.769	1.855	1.763	-121.3	-0.13	-1.207	0.239
$r_{Y3a\ Xia}$	$r_{Y3a\ X1a}$	$r_{Y3a\ X2a}$	$r_{Y3a\ X3a}$	$r_{Y3a\ X4a}$	$r_{Y3a\ X5a}$	$r_{Y3a\ Y1a}$	$r_{Y3a\ Y2a}$
	0.278	0.208	0.212	-0.091	-0.13	-0.846	0.234

Compared to those presented regarding PAH monitoring in the HPM hydrodesulfurization plant, it is found that: i) the data in table 1 and figure 1 show a greater or more important variability of the process factors *(X_1 - X_5)*, facts that are also transmitted to the process responses *Y_1*, *Y_2* and *Y_3* respectively , ii) some strong increases in the gas flow rate in the plant (figure 1, *X_4* day 30) are not found as an influence in the process responses, iii) figures 2 -3 show that the normalized PAH concentration is influenced by all factors except *X_{4a}*, iv) in figure 4 a strong link is observed between the response *Y_{3a}* and *Y_{1a}* (the normalized sulphur concentration in the product).

In table 3 we find that the PAH and sulphur content in the hydrofined diesel from HPM installation has about the same dispersion compared to the average of almost +- 20%**.** It is also worth noting the extremely small dispersion of the density of the fed diesel fuel and the processed diesel fuel. By r_{Y3aX4a} near to zero Table 4 shows that the gas flow rate through the hydrodesulfurization reactor does not influence the PAH content in processed diesel fuel. Table 4 also ranks the positive and negative influences on the normalized pH concentration in the product. The diesel density determines a positive influence on PAH content with $r_{Y3a\ X1a} = 0.278$. Then follows the temperature influence $r_{Y3a\ X3a} = 0.212$ and that of the diesel flow through the reactor $r_{Y3a\ X2a} = 0.208$. It is worth noting that a relatively sulphur-rich diesel fuel at the reactor inlet slightly decreases the PAH content in the product ($r_{Y3a\ X5a}$ =-0.13). In this sense, there is also an extremely strong correlation between the sulphur content and the PAH content in the product ($r_{Y3a\ Y1a} = -0.86$). It can thus be considered that if there is an expression that links the sulphur content in the product to the process factors, then this relationship can be translated to express the PAH content in the product.

Data from Table 2, regarding PAH monitoring for HDV plant, were processed according to the same procedure. We thus find in Figure 5 the daily state of the normalized variables for the HDV facility. Respect to HDV plant the figures 6-8 present the dependences of normalized PAH concentration (Y_{3a}) versus of all normalized process variables. Table 5 gives mean and standard deviation of monitored variables from HDV plant, whereas table 6 considers the covariance and correlation coefficient of Y_{3a} with normalized variables from HDV plant.

Table 5.

Mean and standard deviation of monitored variable from HDV plant

Variable	X_1	X_2	X_3	X_4	X_5	Y_1	Y_2	Y_3
m.u	Kg/m^3	m^3/h	^0C	Nm^3/h	% mass	ppm	Kg/m^3	g/l
Mean	859.2	162.5	308.1	$7.8\ 10^4$	0.95	5.73	840.4	2.49
Standard deviation	3.83	12.3	5.97	$1.85\ 10^3$	0.097	2.99	4.27	0.69

Table 6.

Covariance and correlation coefficient of Y_{3a} with normalized process variables from HPM plant

$cov(Y_{3a},X_{ia})$	$(Y_{3q}X_{1a})$	$(Y_{3q}X_{2a})$	$(Y_{3q}X_{3a})$	$(Y_{3q}X_{4a})$	$(Y_{3q}X_{5a})$	$(Y_{3q}Y_{1a})$	$(Y_{3q}Y_{2a})$
	-0.882	1.67	1.772	-4.52	-0.048	-1.31	-0.522
$r_{Y3a\ Xia}$	$r_{Y3a\ X1a}$	$r_{Y3a\ X2a}$	$r_{Y3a\ X3a}$	$r_{Y3a\ X4a}$	$r_{Y3a\ X5a}$	$r_{Y3a\ Y1a}$	$r_{Y3a\ Y2a}$
	-0.209	0.131	0.174	-0.003	-0.324	-0.631	-0.136

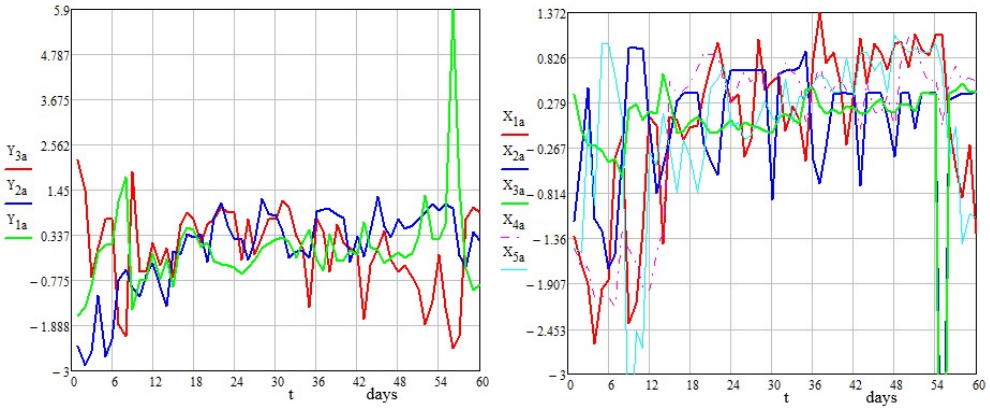

Fig. 5. Daily state of dimensionless variables Y_{ai} and X_{ai} respectively for HDV plant (Y_{a1}-normalized sulphur concentration in processed diesel, Y_{a2}-normalized density of processed diesel, Y_{a3} -normalized PAH concentration in processed diesel, X_{a1}-normalized density of crude diesel, X_{a2}- normalized reactor input crude diesel flow rate , X_{a3}-normalized temperature of hydrogenation reactions ,X_{a4}- normalized gas flow rate through reactor, X_{a5}-normalized sulphur concentration at reactor input)

Comparing the results regarding the factors influence on PAH content of diesel produced from HDV plant with those reported for HPM plant, we can note: i) the independence of Y_{3a} from X_{4a} (gas flow rate through the catalytic bed) is maintained, ii) the direction of the dependence of Y_{3a} on X_{1a} (diesel density in reactor fed) is reversed, iii) the influence of X_{2a} (normalized liquid flow rate through the bed) and X_{3a} (temperature of hydrogenation reactions in normalized expression) on Y_{3a} is somewhat less intense, iv) the extremely strong, almost linear, relationship between Y_{3a} and the normalized sulphur concentration in the diesel produced is maintained.

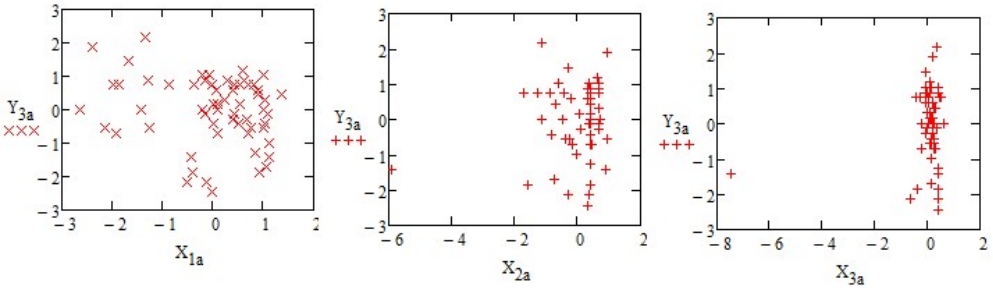

Fig. 6. Status of normalized PAH concentration according to normalized variables X_{a1} (normalized density of crude diesel), X_{a2} (normalized reactor input crude diesel flow rate) and X_{a3} (normalized temperature of hydrogenation reactions) respect to HDV plant

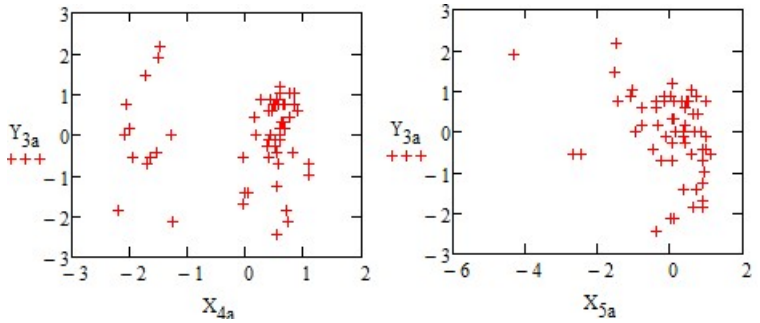

Fig. 7. Status of normalized PAH concentration (Y_{3a}) according to normalized variables X_{a4} (normalized gas flow rate) and X_{a5} (normalized sulphur concentration at reactor input) respect to HDV plant

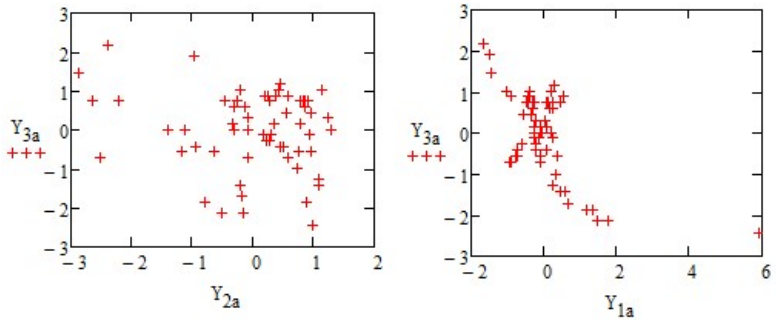

Fig. 8. Status of normalized PAH concentration (Y_{3a}) according to normalized variables Y_{a1} (normalized sulphur concentration in processed diesel) and Y_{a2} (processed diesel normalized density) respect to HDV plant

The differences mentioned above with reference to the two installations can be attributed to the differentiation, especially of the catalyst, between them, which is given in Table 7. In the case of both HPM and HDV data, the Y3a versus X1a and Y3a versus Y2a links can be considered difficult to support given the variability of the two, the dispersion of which is, as shown in Tables 3 and 5, extremely low compared to the average. For PAH concentrations in the HPM or HDV feed of 8-10 g/l, it remains that the diesel flow rate through the bed, the temperature of the catalytic hydrogenation reactions and the sulfur content in the bed, determine the PAH concentration in the diesel produced.

Table 7.

The difference between HPM and HDV

Characteristic	HDV	HPM
Raw material	Top distillate (heavy naphtha, kerosene)	Crude/semi-refined diesel fuel
Scope	Primary purification, pretreatment	Final finishing, Euro 5 diesel
Working pressure	25–70 bar	30–80 bar
Temperature	300–370°C	320–380°C
Catalyst	Co–Mo, Ni–Mo	Ni–Mo predominant
Final product	Hydrofined distillate	Hydrofined diesel fuel

Literature data [9] show that the sulphur content of diesel produced in the hydrodesulfurization process decreases with increasing of reaction temperature and the diesel flow rate through the catalytic bed. Considering the correlation coefficients

between r_{y3ay1a} (table 4 and table 6) which are negative and close to unity, it can be appreciated that the PAH content in diesel produced from HPM and HDV can increase with temperature and with diesel flow rate through reactor catalytic bed. Further observation leads to the fact that PAHs are unaffected by hydrogenation in the desulfurization process and moreover they can even be formed within it. It is worth mentioning the existence of technological solutions for removing PAHs from diesel fuel [10, 11] by extraction with dimethyl sulfoxide. And this is a consequence of the environmental requirements noted in the first part of the paper.
However, maintaining constant parameters of the installation according to the values of the last 60 days, it can be seen that the content of polyaromatics in diesel fuel is within the parameters of European standards.

4. Conclusions

The aromatic content of diesel fuel is an important factor considering the emissions, notably particulate matter (PM) concentrations. The ultra-fine particles (UFP, particles with a diameter under 100 nm are important components of engine emissions and connected to various health effects, such as pulmonary and systematic inflammation, and cardiovascular disorders.
For the determination of PAH content in diesel fuel, an analytical method based on HPLC chromatography was considered
The analysis method was implemented for monitoring the PAH content in diesel fuel resulting from PAH and HDV installations
The monitoring data were analyzed by normalizing the values of the monitored parameters and highlighting the link between the normalized PAH concentration and the process-independent factors.
The correlation analysis regarding the link between the normalized PAH concentration in the produced diesel fuel and the process factors completed the statistical analysis
No major differences were found between the results of the statistical calculation for the two installations
Based on the observation that between the sulfur content in the produced diesel fuel and the PAH content in it there is an almost linear correlation, it was concluded on the influence of temperature and diesel fuel flow through the catalytic layer on it
Overall, the present study shows that decreasing the aromatic content of the fuels could be a significant measure in mitigating traffic exhaust toxicity.

Acknowledgement: Monitoring data were obtained through the Petromidia SA support

REFERENCES

[1] Zhong Y., Zhu L., Distribution, input pathway and soil-air exchange of polycyclic aromatic hydrocarbons in Banshan Industry Park, China, *Sci Total Environ*, 444, 177-182, 2013.
[2] Radinko Glugorijevic, Jeremija Jevtic, Djuro Borak, The influence of fuel aromatics on diesel exhaust emission, *Journal of KONES*, 14, 2, 161-170, 2007

[3] Radinko Glugorijevic, Jeremija Jevtic, Djuro Borak, The influence of fuel aromatics on diesel exhaust emission *International Conference- Fuels 2005, Esslingen 2005, Proceedings*, 175, 2005
[4] Yuan –Chung Lin, Wen-Jhy, Chung – Bang Chen, Characterization of Polycyclic Aromatic Hydrocarbons from the Diesel Engine by Adding Light Cycle Oil to Premium Diesel Fuel, *Journal of the Air & Waste Management Association*, 56, 752-758, 2006
[5] Pencíkova K., Ciganek M., Neca J., Illes P., Dvorak Z., Vondracek J., Machala M., Modulation of endocrine nuclear receptor activities by polyaromatic compounds present in fractionated extracts of diesel exhaust particles, *Sci Total Environ*.10, 677, 626-636. 2019
[6]Eleni.D., Salonikidou, Karina Kowalska, Dimitrios.A. Giannakoudakis, Antigoni Margello, Evanthia Nanaki, Spyros Kiartzis, Mariusz Barczak, Piotr Borowski, Konstantinos.S. Triantafyllidis , Merging experimental and theoretical approaches towards understanding real diesel fuel desulfurization by nanoporous carbons, *Chemica Engineering Journal*, 502, 157858, 2024
[7] Lara S., Villanueva F., Cabanas B., Sagrario S., Aranda I., Soriano J., Martin P., Determination of policyclic aromatic compounds, (PAH, nitro-PAH, oxy-PAH) in soot collected from a diesel engine operating with different fuels, *Sci Total Environ*.,20,900,165755, 2023
[8]. Dobre T., Sanchez J. M., Chemical Engineering Modelling Simulation and Similitude, *Chapter 5 Statistical Models*, Wiley VCH, 2007
[9] PETRAS Laura, Dobre T., Serbanescu Nela, Pop D.F., Parvulescu Oana, Cioroiu Tîrpan Doinița-Roxana,Ionut Popa I. Characterization of monitoring data of a diesel hydrodesulfurization reactor with Langmuir-Hinshelwood model: Part 1 - reactor modelling, U.P.B. Sci. Bull., Series B,
87, 3, 252 -238, 2025
[11] Qinghua L., Guoxuan L., Chengmin G., Zhigang L., Solvents evaluation for extraction of polycyclic aromatics from FCC diesel: Experimental and computational thermodynamics, Chemical Engineering Science, 264, 118205, 2022
[12] Placido A-F., Suárez Inmaculada, Baudilio C., Liquid-liquid extraction of polyaromatic compounds with ionic liquid. A theoretical and experimental approach, Separation and Purification Technology, 303, 122160, 2022.

PYROLYSIS OF PLASTIC WASTE TO OBTAIN GASEOUS FUEL

Grigore PȘENOVSCHI [1,2*], Ioan CĂLINESCU[1], Ciprian-Gabriel CHISEGA-NEGRILĂ[1], Cristina-Emanuela ENĂȘCUȚĂ[2]

[1]NUST POLITEHNICA Bucharest, Faculty of Chemical Engineering and Biotechnologies, 1-7 Gheorghe Polizu St., 1st District, Bucharest-011061, Romania
[2]INCDCP-ICECHIM 202 Spl. Independentei, Bucharest-060021, 6th District, Romania

Abstract

Plastic waste from end-of-life vehicles (ELVs) represents a major environmental concern due to increasing generation rates and limited recovery options. This study explores the conversion of polypropylene (PP) and polyethylene (PE) waste into hydrogen-rich gas using microwave-assisted pyrolysis. A monomode microwave reactor was employed with layered configurations of plastic feedstock, silicon carbide as a microwave susceptor, and activated carbon as a catalyst. The influence of catalyst quantity, reactor arrangement, and polymer type was systematically investigated. Under optimized conditions, technical-grade PP yielded up to 81.4 wt.% gas with a hydrogen concentration of 45.2 vol.% and a hydrogen efficiency of 44.8 g/g. The produced gases exhibited high calorific values (46,941–55,087 kJ/kg) and low CO_2 emissions (4.4–6.1 × 10^{-5} kg CO_2/kJ). Comparative tests using conventional heating showed lower hydrogen yields (4.77 mmol/g vs. 19.7 mmol/g for microwave-assisted pyrolysis), highlighting the higher energy efficiency and lower carbon intensity of the microwave process.

Key words: Catalytic pyrolysis; polypropylene recycling; end-of-life vehicles (ELVs); activated carbon; waste-to-energy; environmental impact.

1. Introduction

Plastic materials, once seen as symbols of technological progress, have become major environmental challenges. In the context of the European Union's 2050 sustainability strategy, plastic waste management must evolve toward a circular economy model. End-of-life vehicles (ELVs) contain up to 200 kg of plastic, predominantly polypropylene (PP) and polyethylene (PE) [1, 2]. Mechanical recycling often leads to degradation, whereas chemical recycling-particularly pyrolysis, produces gases and oils that can substitute fossil fuels. Microwave-assisted pyrolysis combines dielectric heating and catalysis, achieving rapid and uniform heating with improved gas yields [3].

2. Experimental

Experiments were performed in a quartz reactor (17 mm inside diameter) located inside a monomode microwave cavity operating at 2.45 GHz and 600 W. Pyrolysis was carried out at 660 °C for 10 minutes under N_2 flow.

Feedstock

Silicon carbide (SiC) (2–4 mm, supplied by Sinabuddy Mineral, Zhengzhou, China) and activated carbon (AC) derived from coconut shell (6 × 12 mesh, Legend Inc., Sparks, NV, USA) were used as the microwave susceptor and catalyst, respectively. Polypropylene (PP) granules and low-density polyethylene (LDPE MI 2) granules were procured from Romcolor, Copăceni, Romania. In addition, polypropylene waste (PP_W) and two mixed polyolefin wastes composed of PP and PE, collected from dismantled automotive parts provided by SC Pieseauto Dez SRL, Constanța, Romania, were used as representative end-of-life vehicle (ELV) plastic feedstocks, denoted as PP + PE_W1 and PP + PE_W2, respectively.

Product Yield

The distribution of pyrolysis products - gas, liquid, and solid - was quantified gravimetrically. After the reaction, the condensed liquid fraction was collected and weighed, while the solid residue remaining in the reactor was measured directly. The gaseous fraction was determined by difference from the initial polymer mass according to the overall mass balance. Product yield was expressed as a percentage of the initial feedstock mass, following Equation (1):

$$Y_{gas} = \frac{m_0 - m_{liquid} - m_{solid}}{m_0} \quad (1)$$

where m_0 is the mass of the polymer feedstock, m_{liquid} is the mass of the condensed oil, and m_{solid} is the residual char after pyrolysis.

The efficiency of hydrogen generation during the pyrolysis process was assessed using the hydrogen efficiency parameter, calculated according to Equation (2):

$$\text{Hydrogen efficiency} = \frac{m_{H_2,gas}}{m_{H_2,theoretical}} \times 100\% \quad (2)$$

where $m_{H_2,\text{gas}}$ represents the mass of hydrogen produced in the gaseous fraction, and $m_{H_2,\text{theoretical}}$ denotes the theoretical hydrogen content in the initial polymer feedstock. This parameter provides a quantitative measure of the process efficiency in converting polymer-bound hydrogen into gaseous hydrogen. The actual hydrogen content in the gaseous fraction was determined based on the compositional data obtained from GC-MS analysis. The theoretical hydrogen mass contained in the polymer feedstock was considered 0.142857 g of H_2 per gram of plastic for both polyethylene (PE) and polypropylene (PP).

The hydrogen yield was determined to quantify the amount of hydrogen released per unit mass of polymer during pyrolysis. It was calculated using the molar ratio between the hydrogen produced in the gaseous fraction and the initial mass of the feedstock, as expressed in Equation (3):

$$Y_{H_2} = \frac{n_{H_2}}{m_{plastic}} \quad (3)$$

where n_{H_2} is the number of moles of hydrogen generated, and m_{plastic} is the initial mass of the polymer sample (in grams).

The yield, expressed in mmol H_2 per gram of plastic, serves as an indicator of the hydrogen productivity of each experimental configuration.

Gross Heating Value

The gross heating value (GHV) of the gaseous products was determined based on the volumetric composition of the gas mixture obtained from GC analysis. The overall calorific value was calculated as the weighted average of the individual heating values of the main gaseous components – H_2, CH_4, CO, CO_2, and light hydrocarbons—according to Equation (4):

$$GHV_{mixture} = \sum(GHV_i \times \frac{C_i}{100}) \quad (4)$$

where GHV_i represents the calorific value of component *i* (in kJ/kg), and C_i is the volumetric concentration (%) of that component in the gas mixture.

CO_2 emissions

The estimation of carbon dioxide emissions was performed to evaluate the environmental performance of the produced gases compared to conventional fuels. The total CO_2 formed during the combustion of the gaseous products was calculated from the volumetric concentration of carbon-containing components (CH_4, CO, and other hydrocarbons) using stoichiometric combustion relationships, as shown in Equations (5) and (6):

$$CO_{2,total} = \sum(CO_{2,i} \times \frac{C_i}{100}) \quad (5)$$

$$CO_{2,specific} = \frac{CO_{2,total} \times 44/22.4}{GHV_{mixture}} \quad (6)$$

where $CO_{2,i}$ denotes the theoretical CO_2 yield for each gas component, C_i is the corresponding volumetric concentration (%), and GHV_{mixture} is the calorific value of the total gas mixture (kJ/kg).

The specific CO_2 emission value expresses the amount of CO_2 (kg) released per unit of energy produced (kJ) during gas combustion.

3. Results and discussions

Experimental setups and resulting product yields

The pyrolysis experiments were carried out in a specially designed quartz tube reactor (17 mm inner diameter and 20 mm outer diameter) situated inside a monomode

microwave cavity. The experimental setup is illustrated in Figure 1. The installation consists of a microwave-assisted pyrolysis installation. 1 – Microwave Generator GMP 30K SM 56T400 FST 3 IR (Sairem – France); 2 – Standard WR340 waveguide (Sairem France); 3 – 2.45 GHz 4-Stub Automatic Tuner AI 4S A 2450/340 (Sairem – France); 4 – Single-mode cavity (Sairem - France); 5 – Sliding Short Circuit PCCMWR340L130PVMR1PE (Sairem – France); 6 – Quartz reactor; 7 – Digital mass flow controller for nitrogen - Smart-Trak® 50 Series (Sierra – USA); 8 – Liquid fraction collection vessel; 9 – 1 Liter Tedlar bag (CEL Scientific Corporation – USA) for collecting gaseous fraction; 10 – Infrared sensor Micro-epsilon (Messtechnik – Germany).

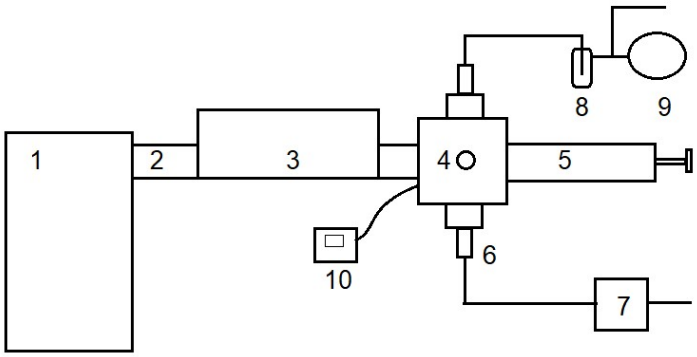

Fig. 1. Microwave-assisted pyrolysis installation.

In the monomode microwave applicator, efficient absorption of microwave energy occurs only in the presence of silicon carbide (SiC). To achieve uniform heating of the polymer material, alternating layers of plastic granules and SiC were employed within the reactor. To examine how the amount and arrangement of catalyst and susceptor influence polypropylene (PP) pyrolysis, nine experimental configurations—designated PP_T_01 to PP_T_09—were established. These setups differed in the quantities and spatial distribution of silicon carbide (SiC) and activated carbon (AC), which were arranged in alternating layers with the PP feedstock inside the reaction chamber. The schematic illustration in Figure 2 depicts the configuration layout, where light grey layers correspond to PP, dark grey to SiC, and black to AC.

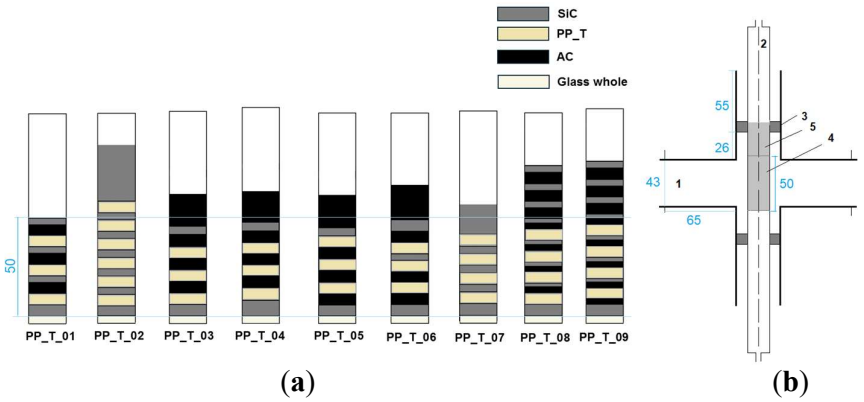

Fig. 2. Schematic illustration of the layered arrangements inside the quartz reactor: (a) representation of the alternating layers; (b) quartz reactor positioned within the single-mode microwave cavity. Legend: 1 – single-mode cavity; 2 – quartz reactor; 3 – Teflon rings coated with aluminum foil for reactor alignment; 4 – reactor filling located in the active microwave zone; 5 – additional reactor filler. The dimensions of both the monomode cavity and the quartz reactor are provided in millimeters.

Each configuration was pyrolyzed at 700 °C for 10 minutes under a nitrogen atmosphere using a monomode microwave reactor operating at a maximum power of 700W. The resulting proportions of gaseous, liquid, and solid products were determined for each experiment, and the summarized data are presented in Table 1.

Table 1.

Experimental product yields and hydrogen generation for each reactor configuration using polypropylene feedstock

Configuration	Amount (%)			Conversion %	H_2, vol.%
	Feedstock	SiC	AC		
PP_T_01	22.28	45.45	27.27	55.0	7.25
PP_T_02	28.57	71.43	0.00	66.0	16.19
PP_T_03	23.08	30.77	46.15	62.3	19.75
PP_T_04	21.43	35.71	42.86	9.5	10.41
PP_T_05	23.08	30.77	46.15	40.3	19.27
PP_T_06	21.43	35.71	42.86	57.0	25.37
PP_T_07	33.33	66.67	0.00	93.5	22.74
PP_T_08	25.00	43.75	31.25	92.8	13.87
PP_T_09	22.86	45.71	31.43	90.3	45.23

Nine experimental configurations (PP_T_01–PP_T_09) were investigated to determine the influence of catalyst loading and layer arrangement on the thermal decomposition of polypropylene (PP) under microwave irradiation. Each configuration differed in the quantity and stacking order of silicon carbide (SiC) and activated carbon (AC), which served as the microwave susceptor and catalyst, respectively. The purpose of these variations was to optimize the interaction between the polymer and the microwave field, ensuring efficient energy transfer and maximizing hydrogen generation.

For configurations with lower SiC and AC content (PP_T_01–PP_T_04), the hydrogen concentration did not exceed 20 vol.%. These setups exhibited uneven heating, leading to partial melting and localized degradation zones.

Configurations PP_T_05–PP_T_08 displayed improved hydrogen fractions (19.27-25.37 vol.%). The improved conversion efficiency was attributed to more uniform temperature distribution and increased contact between the molten polymer and the active catalytic surfaces.

Among the nine tested configurations, PP_T_09 demonstrated the most efficient performance, achieving the highest hydrogen concentration (45.23 vol.%) when 22.86 % of polypropylene was processed together with 31.43 % of activated carbon and 45.71% of silicon carbide. This particular configuration provided an optimal balance between microwave energy absorption and catalytic activity, ensuring uniform heating and extensive polymer degradation. The combined presence of SiC and AC generated strong microwave–material interactions, while the large surface area of the activated carbon promoted secondary cracking and dehydrogenation reactions.

Pyrolysis of different polyolefins

The type of plastic feedstock employed in the pyrolysis process had a notable impact on both the gas yield and the composition of the gaseous fraction, especially regarding hydrogen content. Experiments were performed using polypropylene granules (PP_T), polyethylene granules (PE_T), and plastic waste from automotive dismantling, including PP waste (PP_W) and two PP+PE waste mixtures (PP+PE_W1 and PP+PE_W2). The results are summarized in Table 2.

Table 2.

Product distribution obtained at microwave-assisted pyrolysis of various PP and PE feedstocks

Exp.	Results, wt.%			Conversion %	H_2 efficiency g/g	H_2 yield, mmol/g plastic
	solid	liquid	gas			
PE_T	12.1±0.6	9.95±1.1	77.9±1.5	93.0±0.4	20.03±1.6	14.3±0.6
PP_T	6.65±1.2	11.91±1.3	81.44±1.5	90.3±0.3	44.81±1.8	32.0±0.3
PP_W	7.72±0.7	14.39±1.5	77.89±1.8	95.0±0.2	27.5±3.5	19.7±2.4
PP+PE_W1	22.32±2.1	11.3±1.2	66.7±1.7	99.0±0.5	56.4±2.1	34.4±0.4
PP+PE_W2	4.48±0.03	7.08±2.0	87.08±1.0	96.8±0.6	8.66±0.1	6.2±0.1

Among the technical plastics tested, polypropylene granules (PP_T) showed a high hydrogen yield (32.0 mmol/g plastic) along with a substantial gas fraction (81.44 wt. %) and a hydrogen efficiency of 44.81 g/g, confirming its suitability for microwave-assisted pyrolysis aimed at producing hydrogen-rich gas.

Polyethylene granules (PE_T), although producing a similar gas fraction (77.9 wt. %), generated significantly less hydrogen (14.3 mmol/g) and had a lower hydrogen efficiency (20.03 g/g), less than half that of PP_T, indicating that PE is less favorable for hydrogen production under the same conditions.

The mixed plastic waste samples exhibited contrasting behavior. PP+PE_W1, despite a relatively low gas yield (66.7 wt. %) and the highest solid residue (22.32 wt. %) due to filler content in this plastic waste, achieved the highest hydrogen yield (34.4 mmol/g) and hydrogen efficiency (56.4 g/g). This suggests that certain components

or structures in this waste promote hydrogen formation or inhibit secondary reactions that consume hydrogen, although the high solid content indicates the presence of undecomposed materials or inert fillers.

PP+PE_W2 produced the highest gas fraction (87.08 wt. %) and high conversion (96.8 %) but the lowest hydrogen yield (6.2 mmol/g) and hydrogen efficiency (8.66 g/g), highlighting the influence of feedstock composition on hydrogen production.

These results demonstrate that both the type of polymer and the origin or purity of the plastic waste (fillers, additives, or degradation products) critically affect the performance of microwave pyrolysis for hydrogen generation. Clean polypropylene remains the most effective feedstock, while mixed or contaminated waste streams may require pretreatment or catalyst optimization to enhance hydrogen yields. Overall, the increased gas yields observed in our experiments represent a significant advantage.

The composition of the gas fraction from microwave-assisted pyrolysis showed considerable variation depending on the type and source of the plastic feedstock (Table 3). The main gaseous products were hydrogen (H_2), methane (CH_4), ethane (C_2H_6), ethylene (C_2H_4), propane (C_3H_8), propylene (C_3H_6), butenes, along with minor amounts of carbon oxides (CO and CO_2) and heavier hydrocarbons (C_5–C_6+).

Tables 3.

Composition of gases obtained at microwave-assisted pyrolysis of different plastic feedstocks

Exp.	Concentration, vol.%						
	H_2	CO	CH_4	C_2H_6	CO_2	C_2H_4	C_3H_8
PE_T	36.63	2.11	22.76	5.42	0.71	18.39	1.94
PP_T	45.23	1.04	43.28	8.61	1.51	0.03	0.03
PP_W	46.50	0.78	16.52	4.25	4.09	15.53	1.89
PP+PE_W1	75.35	0.16	0.29	7.07	0.35	0.68	1.21
PP+PE_W2	20.05	0.68	23.32	8.25	2.50	19.64	1.79

Exp.	Concentration, vol.%						
	C_3H_6	i-C_4H_{10}	n-C_4H_{10}	1-C_4H_8	2-C_4H_8	C_5	C_{6+}
PE_T	3.93	0.00	1.00	2.04	1.92	0.57	2.59
PP_T	0.15	0.01	0.00	0.00	0.07	0.02	0.02
PP_W	5.41	0.22	0.15	0.59	2.06	0.48	1.52
PP+PE_W1	3.35	0.36	0.29	0.30	2.68	1.51	6.41
PP+PE_W2	7.96	0.95	0.58	1.16	4.92	2.25	5.93

PP_T produced a gas rich in both H_2 (45.23 vol. %) and CH_4 (43.28 %), with very low amounts of unsaturated light hydrocarbons such as ethylene (0.03 %) and propylene (0.15 %). This indicates efficient chain scission reactions with minimal secondary reactions, generating mainly small, saturated molecules and hydrogen. The low CO (1.04 %) and CO_2 (1.51 %) levels further suggest non-oxidative degradation pathways.

PE_T, consistent with expectations for polyethylene, yielded a more complex gas composition. It produced moderate H_2 (36.63 %) and CH_4 (22.76 %), along with higher concentrations of ethylene (18.39 %) and ethane (5.42 %). The presence of olefins, including propylene (3.93 %), points to incomplete cracking and reflects the lower reactivity of the resulting alkenes under the tested conditions, consistent with the saturated PE backbone favoring β-scission reactions.

The waste PP sample (PP_W) generated gas with high H_2 content (46.5 %) and increased levels of olefins and C_3–C_4 fragments, including propylene (5.41 %) and total

C_4 unsaturated hydrocarbons (2.65 %), compared to PP_T. CO_2 was also the highest among all samples (4.09 %), likely due to the degradation of additives or minor oxygenated components.

Among all tested feedstocks, PP+PE_W1 produced an exceptionally high hydrogen concentration of 75.35 vol. %, well above that of PP_T (45.23 %) and PE_T (36.63 %). Despite this, CH_4 content was minimal (0.29 %), and CO and CO_2 were very low (0.16 % and 0.35 %, respectively), indicating strong selectivity toward H_2 formation with limited reforming or oxidation reactions. This behavior may result from the specific composition of the waste mixture enhancing dehydrogenation.

PP+PE_W2, in contrast, exhibited a low H_2 concentration (20.05 %) but higher levels of CH_4 (23.32 %), propylene (7.96 %), and significant C_4–C_6 hydrocarbons. The broader product distribution suggests more complex pyrolysis behavior, likely influenced by fillers, stabilizers, or other additives in the material.

Gross Heating Value and CO_2 emissions of gases

The gross heating value (GHV) and CO_2 emissions of the pyrolysis gases varied considerably depending on the plastic feedstock type and the heating method used, as summarized in Table 4.

Table 4.

Gross heating value and CO_2 emissions of gases obtained at microwave-assisted pyrolysis of different plastic feedstocks

Exp	$GHV_{mixture}$,		CO_2 emissions	CO_2 specific emissions
	kJ/m^3	kJ/kg	L CO_2 / L gas mixture	kg CO_2/kJ
PE_T	44398.25	49750.55	1.28	5.68E-05
PP_T	27959.21	54320.32	0.63	4.40E-05
PP_W	37577.78	47625.47	1.36	5.82E-05
PP+PE_W1	36016.20	55087.35	0.90	4.92E-05
PP+PE_W2	59826.72	46941.68	1.86	6.12E-05

Among the tested samples, microwave-assisted PP_T produced the lowest GHV (27,959 kJ/m³) due to the high hydrogen content (45.23 vol. %) and relatively low hydrocarbon fraction, whereas PE_T and PP_W gases achieved higher calorific values, exceeding 37,500 kJ/m³, confirming the potential of microwave pyrolysis to generate fuel-rich gas mixtures. PP+PE_W2 exhibited the highest GHV (59,826.72 kJ/m³), reflecting the substantial presence of saturated and unsaturated C_3–C_6 hydrocarbons, which contribute significantly to the energy density.

CO_2 emissions per liter of gas were lowest for PP_T (0.63 L CO_2/L gas) and PP+PE_W1 (0.90 L CO_2/L gas), indicating cleaner gas compositions with a lower carbon footprint. In contrast, feedstocks with higher hydrocarbon content, particularly conventionally heated samples, tend to emit more CO_2 per unit volume, highlighting the higher environmental impact of hydrocarbon-rich gases.

When expressed per unit mass (kJ/kg), GHV was highest for hydrogen-rich gases, notably PP_T (54,320 kJ/kg) and PP+PE_W1 (55,087 kJ/kg), while all other samples still exceeded the energy content of conventional fuels such as kerosene or diesel. Specific CO_2 emissions, measured in kg CO_2/kJ, ranged from 4.40×10^{-5} kg CO_2/kJ for PP_T to

6.12×10^{-5} kg CO_2/kJ for PP+PE_W2, demonstrating the superior carbon efficiency of microwave-assisted pyrolysis, particularly for hydrogen-rich gas production. In all cases, specific emissions were lower than those of conventional fossil fuels.

Overall, these results indicate that while microwave-assisted pyrolysis may yield gases with slightly lower volumetric energy due to high hydrogen content, it provides a more sustainable, low-carbon route for generating hydrogen-rich syngas or fuel gas mixtures, with a clear advantage over conventional hydrocarbon-rich pyrolysis products. The calorific value and carbon intensity of these gases, compared with common commercial fuels, are presented in Table 5.

Table 5.

Calorific value and carbon intensity of common commercial fuels [4-6]

Fuel	GHV		CO_2 emissions
	kJ/m^3	kJ/kg	kg CO_2/kJ
propane	99000	50400	5.96E-05
kerosene	37400	46200	6.94E-05
diesel	38578	45600	7.03E-05
natural gas	37285	52200	5.01E-05

The highest GHV per unit mass (kJ/kg) was observed for microwave-heated PP+PE_W1, reaching 55087 kJ/kg, followed closely by PP_T at 54320.32 kJ/kg. These values exceed those of typical liquid and gaseous fuels (Table 5), underscoring the energy-dense character of certain pyrolysis-derived gases.

From an environmental perspective, the specific CO_2 emissions of the pyrolysis gases were generally lower than or comparable to those of conventional fossil fuels. The cleanest gas was obtained from PP_T (4.40×10^{-5} kg CO_2/kJ), considerably lower than propane (5.96×10^{-5} kg CO_2/kJ), natural gas (5.01×10^{-5} kg CO_2/kJ), kerosene (6.94×10^{-5} kg CO_2/kJ), or diesel (7.03×10^{-5} kg CO_2/kJ). Even the sample with the highest carbon intensity.

4. Conclusions

Pyrolysis-derived gas from plastic waste, particularly polypropylene, has demonstrated strong potential as an alternative fuel due to its high energy density, making it a promising and sustainable energy source. This approach also offers the potential to reduce carbon emissions, contributing to global efforts to minimize the environmental impact of plastic waste.

Microwave-assisted pyrolysis further enhances this potential by producing cleaner gas compositions with high GHV (kJ/kg). Microwave heating improves selectivity toward lighter hydrocarbons, which are valuable for fuel refining, and provides a route to more refined fuel products. The method is also highly effective for hydrogen production, achieving yields up to 34.4 mmol H_2/g plastic with improved efficiency. This highlights the ability of microwave energy to break down polypropylene and generate hydrogen-rich gases, which are important for future energy applications.

Activated carbon, used as a catalyst in this study, plays a critical role in optimizing pyrolysis. Its presence influences the distribution of liquid and gaseous products, enhances overall yield, and promotes the formation of lighter, more valuable

hydrocarbons. The combination of microwave energy and activated carbon offers a unique advantage, as the gaseous fraction exhibits GHV values 7.4 to 10.5 times higher than the liquid fraction, enabling efficient energy recovery with a reduced carbon footprint.

The type and purity of the plastic feedstock, particularly PP+PE mixtures, also significantly affect product yields and composition. Cleaner feedstocks allow for better process control and more favorable product distributions.

Overall, microwave-assisted pyrolysis offers substantial advantages for converting polypropylene and polyethylene waste into hydrogen-rich gases. When combined with activated carbon as a catalyst and applied to cleaner feedstocks or controlled waste mixtures, this technology presents a sustainable pathway for waste-to-energy conversion and a significant reduction in environmental pollution from plastic waste.

5. Acknowledgments

- the PN 23.06 Core Program – ChemNewDeal within the National Plan for Research, Development and Innovation 2022-2027, developed with the support of the Ministry of Research, Innovation, and Digitalization, project no. PN 23.06.01.01, AQUAMAT;

- the Competitiveness Operational Program 2014-2020, Action 1.1.4: Attracting high-level personnel from abroad to enhance the RD capacity, project: P_37_471, „Ultrasonic/Microwave Nonconventional Techniques as new tools for nonchemical and chemical processes", financed by contract: 47/05.09.2016

REFERENCES

[1] Kanari, N., J.-L. Pineau, and S. Shallari, End-of-life vehicle recycling in the European Union. Jom, **2003**. 55(8): p. 15-19, 1047-4838,

[2] Perissi, I. and A. Jones, Investigating European Union decarbonization strategies: Evaluating the pathway to carbon neutrality by 2050. Sustainability, **2022**. 14(8): p. 4728, 2071-1050,

[3] Zhou, N., et al., Catalytic pyrolysis of plastic wastes in a continuous microwave assisted pyrolysis system for fuel production. Chemical Engineering Journal, **2021**. 418: p. 129412, 1385-8947,

[4] Jeswani, H., et al., Life cycle environmental impacts of chemical recycling via pyrolysis of mixed plastic waste in comparison with mechanical recycling and energy recovery. Sci Total Environ, **2021**. 769: p. 144483, 1879-1026 (Electronic); 0048-9697 (Linking), https://doi.org/10.1016/j.scitotenv.2020.144483

[5] The Engineering ToolBox. Heating Values of Fuel Gases. 2005 [cited 2025 22.10.2025]; Available from: https://www.engineeringtoolbox.com/heating-values-fuel-gases-d_823.html.

[6] Carbon Dioxide Emissions Coefficients. [cited 2025 22.10.2025]; Available from: https://www.eia.gov/environment/emissions/co2_vol_mass.php.

TRANSPARENT AI MODELS FOR CHEMICAL PROCESS DIAGNOSTICS: INSIGHTS FROM ONER AND JRIP

Andrei COMAN[1,*], Silvia CURTEANU[2]

[1]"Cristofor Simionescu" Faculty of Chemical Engineering and Environmental Protection, "Gheorghe Asachi" Technical University of Iași, 73 Dimitrie Mangeron Blvd., Iași, Romania

[2]"Cristofor Simionescu" Faculty of Chemical Engineering and Environmental Protection, "Gheorghe Asachi" Technical University of Iași, 73 Dimitrie Mangeron Blvd., Iași, Romania

Abstract

This paper investigates the use of Explainable Artificial Intelligence (XAI) in chemical engineering, focusing on rule-based methods that combine interpretability with operational value. Two case studies were developed on synthetic datasets representative of industrial processes. The first applies the OneR algorithm to water quality monitoring, while the second uses JRip for industrial emissions classification. Results highlight how these interpretable models can support diagnostics, process optimization, and compliance with regulatory requirements.

Key words: Explainable Artificial Intelligence; OneR; JRip; Chemical Engineering; Process Monitoring; Industrial Emissions

1. Introduction

The digital transformation of the chemical industry has accelerated significantly in recent years, reshaping how processes are designed, modeled, and optimized. The convergence of Industry 4.0 principles, high-frequency data acquisition, and automated control systems has generated vast multivariate datasets that capture complex and nonlinear interactions between process variables. These developments have strengthened the role of Artificial Intelligence (AI) and Machine Learning (ML) as essential tools for process modeling, predictive maintenance, and quality assurance [1-3].

However, despite their proven predictive capabilities, many AI and ML models still operate as "black boxes," offering high accuracy but little transparency regarding how predictions are derived. In chemical engineering, where operational safety, product conformity, and regulatory accountability are non-negotiable, this opacity represents a major barrier to industrial adoption [4-6]. Engineers and decision-makers must not only trust model outputs but also understand the reasoning behind them, particularly when decisions affect process safety or environmental compliance.

To overcome this limitation, the field of Explainable Artificial Intelligence (XAI) has emerged as a cornerstone of trustworthy and auditable digital transformation. XAI provides interpretive mechanisms that make model reasoning transparent and traceable, quantifying how each input variable influences the final outcome [7–9]. By bridging the gap between mathematical abstraction and engineering understanding, explainable models facilitate communication between data scientists and plant operators,

* Corresponding author: Andrei Coman, Email address: andreicoman22@gmail.com

transforming AI from an opaque computational tool into a reliable partner for process diagnostics and decision support.

In chemical process modeling, XAI serves multiple critical functions. First, it enhances the interpretability of predictive systems used for monitoring and optimization, allowing engineers to validate automated recommendations through domain knowledge. Second, it supports regulatory compliance by documenting the causal relationships between process inputs and outputs, ensuring that algorithmic decisions remain auditable under frameworks such as the EU Artificial Intelligence Act or industrial Good Manufacturing Practice (GMP) standards [10-12]. Third, explainable models improve operator trust and facilitate their integration into digital twins, predictive maintenance frameworks, and emission-control systems [13].

Recent literature demonstrates a growing number of successful XAI implementations in industrial environments. Rule-based algorithms such as OneR and JRip (RIPPER) have been used for tasks including process state classification, wastewater treatment optimization, and combustion diagnostics [14,15]. These interpretable approaches generate human-readable rules (IF-THEN structures) that align closely with engineering logic, allowing decisions to be directly incorporated into operational procedures and quality management systems. Likewise, probabilistic models such as Naive Bayes have shown strong performance in equipment fault diagnosis and quality prediction, where their transparency enables process engineers to quantify the influence of each variable on defect probability [16]. Moreover, post-hoc explainability frameworks such as SHAP and LIME have been applied to neural and ensemble models to provide both global and local interpretive insights, ensuring that high-complexity models remain accountable and explainable [17,18].

This research builds upon these foundations to explore how explainable AI methods can be effectively integrated into the modeling and optimization of chemical processes. The primary objective is to demonstrate that interpretability and predictive accuracy need not be mutually exclusive. By focusing on JRip and OneR, two rule-based algorithms characterized by their transparency and ease of audit, this study aims to show how interpretable ML models can deliver trustworthy and reproducible results that comply with industrial standards. Both algorithms were applied to representative datasets derived from real process scenarios: industrial water quality monitoring and emission classification.

The overarching goal of this work is to bridge the gap between algorithmic prediction and engineering understanding. By embedding explainability into the core of data-driven modeling, the study contributes to the development of reliable AI frameworks capable of supporting sustainable, safe, and regulation-compliant process operations. In doing so, it aligns with the broader vision of Industry 4.0, where transparency, accountability, and human-centered decision-making are essential for digital transformation in chemical engineering.

2. Experimental

2.1. Datasets description

Two datasets were developed for this research, each simulating realistic operating conditions representative of industrial chemical processes. Since direct access to proprietary industrial data was restricted due to confidentiality and safety regulations, synthetic datasets were generated to reproduce plausible process dynamics, inter-variable correlations, and parameter ranges commonly observed in industrial environments. Both datasets were specifically designed to test the performance and interpretability of explainable machine learning algorithms when applied to classification, process monitoring, and regulatory compliance tasks.

The first dataset, corresponding to Case Study 1, focuses on the monitoring and classification of industrial water quality within a cooling and treatment system. It contains 150 instances, each described by four measured parameters: pH, electrical conductivity (μS/cm), total organic carbon (TOC, mg/L), and temperature (°C). The output variable represents the compliance status ("Compliant" or "Non-compliant") according to predefined industrial water reuse standards and environmental regulations.

The objective of Case Study 1 was to evaluate the capacity of the OneR algorithm to extract simple, single-attribute decision rules capable of describing threshold-based relationships between process variables and compliance outcomes. In particular, this study aimed to demonstrate how minimalist, human-readable rules can provide engineers with transparent operational guidance for water treatment management, while ensuring traceability and auditability in regulatory contexts. Beyond assessing predictive accuracy, the case sought to highlight the practical advantage of interpretable models that can be directly translated into operational procedures or alarm thresholds within process control systems.

The second dataset, corresponding to Case Study 2, addresses the classification of industrial emission levels in a continuous chemical production process. This dataset comprises 200 instances, each characterized by six process variables: combustion temperature (°C), flow rate (m^3/h), CO_2 concentration (ppm), NO_x concentration (mg/m^3), pressure (bar), and oxygen fraction (%). The target variable denotes the emission category, classified as "Acceptable" or "Exceeding Limit," based on reference thresholds derived from environmental protection standards.

The objective of Case Study 2 was to assess the ability of the JRip (RIPPER) algorithm to generate interpretable multivariate rule sets that reflect the causal relationships between combustion conditions and emission outcomes. This case aimed to illustrate how explainable AI models can support real-time diagnostics, enabling process engineers to identify high-risk operational patterns and to justify regulatory decisions through explicit, human-understandable rules. Furthermore, the study explored how rule-based classifiers such as JRip can contribute to compliance verification and environmental auditing, reinforcing the role of transparency in sustainable industrial operation. Table 1 summarizes the key characteristics of both datasets.

Table 1.

Summary of input and output variables for the two investigated case studies

Case Study	Input variables	Output variable	No. of instances	Type of process
Industrial water quality monitoring	pH, Conductivity (µS/cm), TOC (mg/L), Temperature (°C)	Compliance status (Compliant/Non-compliant)	150	Classification
Industrial emission classification	Temperature, Flow rate, CO_2, NO_x, Pressure, Oxygen fraction	Emission category (Acceptable/Exceeding limit)	200	Classification

2.2. Software and tools

All data analyses were performed using the WEKA 3.8 software platform, an open-source machine learning environment developed at the University of Waikato, New Zealand. The datasets were imported in both CSV and ARFF formats and preprocessed within the WEKA graphical interface. Model development was conducted using WEKA's built-in implementations of OneR and JRip.

All experiments were executed on a standard workstation (Intel Core i5 processor, Windows 11). Default parameters were retained to preserve model reproducibility and to ensure comparability with existing XAI studies. Model evaluation was based on accuracy, precision, recall, and F-measure, complemented by the inspection of confusion matrices and rule sets.

2.3. Applied methods

Two case studies were developed to assess how interpretable machine learning algorithms can be applied to industrial chemical data for classification and compliance analysis.

In Case Study 1, the OneR algorithm was employed to classify water quality based on four physicochemical variables: pH, conductivity (µS/cm), total organic carbon (TOC) (mg/L), and temperature (°C). The output variable represented the compliance status of the treated water, labeled as Compliant or Non-compliant. The dataset contained 150 records representative of cooling and water treatment operations, where maintaining optimal chemical balance is essential for process reliability and regulatory conformity. The purpose of this case was to determine whether a minimal-rule classifier can accurately capture threshold-based behavior in continuous process parameters while maintaining full interpretability.

In Case Study 2, the JRip (RIPPER) algorithm was applied to classify industrial emissions from a petrochemical process. Six operational parameters were used as predictors: combustion temperature (°C), residual oxygen (%), gas flow rate (m^3/h), nitrogen oxides (NO_x, mg/m^3), sulfur dioxide (SO_2, mg/m^3), and volatile organic

compounds (VOC, mg/m^3). The target attribute described emissions compliance, defined as Compliant or Exceedance according to environmental regulatory thresholds. The dataset comprised 200 hourly observations simulating variable combustion and exhaust conditions, representative of a continuous industrial operation.

Both algorithms were trained and validated using 10-fold cross-validation, ensuring unbiased estimates of predictive accuracy and generalization capability. Model performance was evaluated through accuracy, precision, recall, and F-measure, while interpretability was assessed qualitatively by analyzing the structure, conciseness, and semantic clarity of the extracted decision rules. This dual evaluation framework allowed the comparison of predictive performance with cognitive transparency, emphasizing the balance between model reliability and explainability - an essential requirement for deployment in safety-critical industrial contexts.

3. Results and discussions

3.1. Case Study 1: Water quality classification using OneR

The first case study evaluated the capability of the OneR algorithm to classify industrial water quality based on a minimal yet interpretable rule set. The model was trained on four input variables: pH, conductivity, total organic carbon (TOC), and temperature, with the target variable indicating the compliance status of the treated water (Compliant or Non-compliant).

Among all predictors, pH emerged as the dominant attribute selected by the OneR classifier, confirming its critical influence on water stability and chemical balance in recirculating industrial systems. The optimal decision threshold identified by the algorithm was approximately pH = 7.2, which delineated compliant from non-compliant samples with a clear boundary. The resulting rule can be expressed as:

IF pH < 7.2 THEN Non-compliant

ELSE Compliant.

This simple threshold rule achieved an overall classification accuracy of 94.0%, with a precision of 0.92 and a recall of 0.90, based on 10-fold cross-validation. The confusion matrix showed balanced predictive performance across both classes, confirming that the model successfully captured the operational patterns relevant to regulatory compliance.

The histogram presented in **Figure 1** illustrates the empirical distribution of *pH* values for compliant and non-compliant samples. The predominance of non-compliant cases at pH values below 7.0 and above 8.0 aligns with expected chemical behavior, as deviations from neutral pH tend to increase corrosion and scaling risks in industrial systems. The clustering of compliant samples within the 7.0-7.5 interval demonstrates the model's ability to detect physically meaningful boundaries consistent with standard water quality criteria.

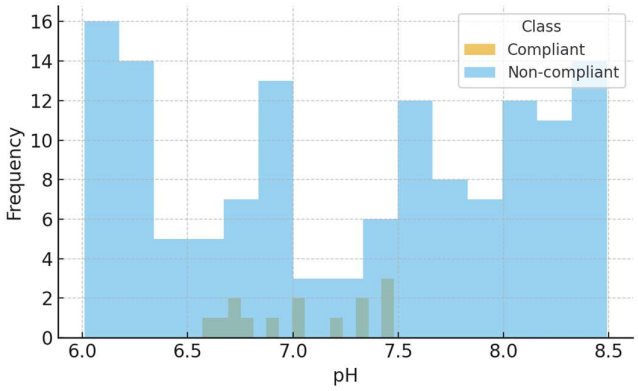

Fig. 1. Distribution of pH values for compliant and non-compliant samples in the industrial water quality dataset.

From an engineering standpoint, this outcome highlights the practicality of **single-rule classifiers** in contexts where rapid interpretability and operational transparency are prioritized over marginal gains in predictive accuracy. The OneR model effectively formalized empirical process knowledge, long used by plant operators, into a reproducible and auditable data-driven rule. Nevertheless, its reliance on a single variable may limit robustness under fluctuating process conditions or when interactions between chemical parameters become non-negligible.

The overall predictive performance of the OneR model is summarized in **Table 2**. The results confirm that, despite its simplicity, the algorithm achieved stable and well-balanced classification metrics, demonstrating its suitability for preliminary compliance screening in industrial water management systems.

Table 2.

Performance metrics of the OneR classifier for industrial water quality prediction

Metric	Value
Accuracy (%)	94
Precision	0.92
Recall	0.9
F-measure	0.91
Cross-validation folds	10

The precision-recall balance indicates that the model maintained consistent discrimination between compliant and non-compliant samples, without bias toward the majority class. The high F-measure value further supports the reliability of the single-attribute rule across all validation folds.

3.2. Case Study 2: Industrial emissions classification using JRip

The second case study focused on the application of the JRip (RIPPER) algorithm to the classification of industrial emission data. The primary objective was to identify operating conditions associated with regulatory exceedances in a petrochemical combustion process. The dataset contained 200 hourly observations described by six operational variables: combustion temperature (°C), residual oxygen (%), gas flow rate (m^3/h), nitrogen oxides (NO_x, mg/m^3), sulfur dioxide (SO_2, mg/m^3), and volatile organic compounds (VOC, mg/m^3). The output variable represented emission status, labeled as Compliant or Exceedance according to established environmental limits.

Following preprocessing and 10-fold cross-validation, the JRip model generated a concise rule set capable of accurately distinguishing between compliant and non-compliant operational states. The classifier achieved an overall accuracy of 96.2%, a precision of 0.95, and an F-measure of 0.94, indicating robust generalization performance across folds. The resulting decision rules, presented below, highlight the most influential process conditions related to emissions behavior:

Rule 1: IF combustion temperature > 880 AND NO_x > 350 → Exceedance

Rule 2: IF residual O_2 < 3.5 AND VOC < 200 → Compliant

Rule 3: IF SO_2 > 250 → Exceedance

These interpretable rules reflect well-established combustion chemistry phenomena: elevated flame temperatures and high nitrogen availability promote NO_x formation, while insufficient oxygen leads to incomplete oxidation and VOC accumulation. The combination of these variables enables a transparent diagnostic view of process efficiency and environmental compliance.

The performance metrics obtained for the JRip classifier are summarized in Table 3, demonstrating the model's ability to maintain both predictive accuracy and interpretability.

Table 3.

Performance metrics of the OneR classifier for industrial water quality prediction

Metric	Value
Accuracy (%)	96.2
Precision	0.95
Recall	0.93
F-measure	0.94
Cross-validation folds	10

From an engineering perspective, the extracted rules can be readily integrated into real-time monitoring systems for continuous compliance verification. Their structure enables clear interpretability by process engineers, supporting both preventive maintenance and regulatory audits. Unlike opaque ensemble methods, JRip provides traceable causal pathways between process variables and emission outcomes, reinforcing trust in data-driven decision frameworks.

The model's interpretability and strong predictive performance position JRip as a valuable tool for industrial process diagnostics, particularly in applications requiring transparent and auditable AI systems. Its rule-based format also facilitates future hybridization with post-hoc explainability tools such as SHAP, enabling combined local and global interpretive perspectives.

3.3. Comparative interpretation

The comparative evaluation of the two case studies highlights the relationship between model simplicity, interpretability, and predictive performance in the context of explainable artificial intelligence applied to chemical engineering.

The OneR algorithm demonstrated that even a single-variable decision rule can achieve a high degree of classification accuracy when the target phenomenon is dominated by a primary physical or chemical driver, in this case, pH. Its transparent formulation allows immediate comprehension and implementation by plant operators. However, its reliance on one predictor limits its adaptability under varying process conditions or when multiple parameters interact nonlinearly.

In contrast, the JRip algorithm offered greater expressive power by capturing multivariate dependencies among combustion temperature, NO_x, and SO_2 concentrations. This additional complexity resulted in superior predictive accuracy and richer diagnostic capability, while maintaining full interpretability through a concise set of human-readable rules. The derived rules aligned closely with known thermochemical relationships, confirming the model's consistency with engineering understanding rather than mere statistical correlation.

Taken together, the two approaches illustrate the explainability-accuracy continuum inherent to AI model selection. OneR occupies the lower-complexity end of the spectrum, ideal for rapid screening and operational transparency, whereas JRip balances interpretability with higher analytical depth, suitable for deployment in real-time monitoring and regulatory compliance systems. Both models underscore the practical value of explainable AI techniques as decision-support tools capable of translating data-driven insights into physically meaningful engineering knowledge.

4. Conclusions

This study demonstrated the applicability of explainable machine learning methods for modeling and compliance assessment in industrial chemical processes. By employing interpretable algorithms, OneR and JRip, the research showed that transparency and predictive performance can be simultaneously achieved without resorting to opaque black-box systems.

The first case study, focused on water quality monitoring, revealed that a single-attribute rule derived by OneR can effectively classify compliance with high accuracy while preserving complete interpretability. Such minimalistic models are well suited for operational environments where clarity and auditability are paramount, and where decisions must be communicated directly to process personnel.

The second case study, addressing emission compliance in petrochemical combustion systems, demonstrated the capacity of the JRip algorithm to capture

multivariate dependencies through concise, human-readable rules. The extracted relationships between combustion temperature, NO_x, and SO_2 concentrations were consistent with established thermochemical knowledge, confirming that rule-based classifiers can yield insights aligned with physical causality rather than statistical coincidence.

Comparative analysis across both studies emphasized that model selection in XAI depends on the balance between complexity, interpretability, and operational purpose. Simpler algorithms provide rapid and transparent decisions suitable for early diagnostic or educational applications, whereas more expressive rule-based models enable comprehensive understanding and predictive reliability for industrial automation and environmental supervision.

From a broader perspective, the results confirm that explainable artificial intelligence constitutes a viable framework for trustworthy digitalization in chemical engineering. By integrating interpretable models into data-driven workflows, engineers can maintain accountability, ensure regulatory compliance, and enhance process transparency, three pillars of sustainable industrial innovation. Future work will extend this research toward hybrid XAI systems that combine rule-based and post-hoc interpretability approaches (e.g., SHAP or LIME), enabling both global and local understanding of complex chemical process behaviors.

REFERENCES

[1] Kagermann, H., Wahlster, W., & Helbig, J. (2013). Recommendations for Implementing the Strategic Initiative INDUSTRIE 4.0. Final Report of the Industrie 4.0 Working Group.
[2] Leon, F., & Galaction, A. I. (2018). Modeling of fermentation processes using AI techniques. Biochemical Engineering Journal, 137, 154–166.
[3] Taboada, M., et al. (2019). Data-driven approaches for wastewater treatment optimization. Environmental Modelling & Software, 120, 104–135.
[4] Doshi-Velez, F., & Kim, B. (2017). Towards a Rigorous Science of Interpretable Machine Learning. arXiv preprint arXiv:1702.08608.
[5] Guidotti, R., et al. (2018). A Survey of Methods for Explaining Black Box Models. ACM Computing Surveys, 51(5), 93.
[6] Carvalho, D. V., Pereira, E. M., & Cardoso, J. S. (2019). Machine Learning Interpretability: A Survey on Methods and Metrics. Electronics, 8(8), 832.
[7] Zhang, H., et al. (2020). Interpretable Machine Learning for Industrial Process Data: Case Studies and Perspectives. Computers & Chemical Engineering, 139, 106904.
[8] Hara, S., & Hayashi, K. (2018). Making Tree Ensembles Interpretable: A Bayesian Model Selection Approach. Proceedings of the AAAI Conference on Artificial Intelligence.
[9] Molnar, C. (2022). Interpretable Machine Learning: A Guide for Making Black Box Models Explainable. 2nd Ed.
[10] European Commission. (2023). Proposal for a Regulation Laying Down Harmonised Rules on Artificial Intelligence (AI Act). Brussels: EU Publications.
[11] Yu, L., et al. (2010). Rule-based approaches for quality assessment in pharmaceutical manufacturing. Computers & Industrial Engineering, 59(4), 789–798.
[12] García, S., et al. (2015). Transparent AI Models for Quality Classification in Pharmaceutical Production. Expert Systems with Applications, 42(21), 7752–7764.
[13] Shao, J., Brodsky, A., & Peters, C. (2022). Explainable Predictive Maintenance Models for Chemical Reactors. Computers & Chemical Engineering, 159, 107666.
[14] Cohen, W. W. (1995). Fast Effective Rule Induction. Proceedings of the 12th International Conference on Machine Learning, 115–123.

[15] Frank, E., & Witten, I. H. (1998). Generating Accurate Rule Sets Without Global Optimization. Proceedings of the 15th International Conference on Machine Learning, 144–151.
[16] Dey, A., et al. (2016). Machine Learning Techniques for Predictive Maintenance: A Review and Case Studies. Journal of Process Control, 51, 1–15.
[17] Lundberg, S., & Lee, S. I. (2017). A Unified Approach to Interpreting Model Predictions. Advances in Neural Information Processing Systems, 30.
[18] Zhou, X., Li, Y., & Chai, X. (2023). SHAP-based Interpretability of Soft Sensors in Polymerization Processes. Chemical Engineering Science, 270, 118662.

EXPLAINABLE AI METHODS FOR DIAGNOSTICS AND OPTIMIZATION IN CHEMICAL PROCESSES: CASE STUDIES WITH J48, LINEAR REGRESSION, M5P AND M5RULES

Dumitriana-Roberta-Marina BRĂNESCU[1,*], Silvia CURTEANU[2]

[1]"Cristofor Simionescu" Faculty of Chemical Engineering and Environmental Protection, "Gheorghe Asachi" Technical University of Iași, 73 Dimitrie Mangeron Blvd., Iași, Romania

[2]"Cristofor Simionescu" Faculty of Chemical Engineering and Environmental Protection, "Gheorghe Asachi" Technical University of Iași, 73 Dimitrie Mangeron Blvd., Iași, Romania

Abstract

In this work, the focus is placed on the integration of interpretable machine learning models into chemical process analysis, with the aim of balancing predictive performance and transparency. Two representative case studies are presented. The first explores the classification of pump operating states using J48 decision trees. The second addresses a distillation column scenario where M5P and M5Rules are applied alongside Linear Regression to capture nonlinear dynamics through piecewise models and explicit rules. The findings emphasize the strengths and limitations of each method and demonstrate how interpretable approaches can transform data-driven models into practical decision-support tools for chemical engineers.

Key words: Explainable Artificial Intelligence; Chemical Engineering; J48; Linear Regression; M5P; M5Rules; Process Optimization

1. Introduction

The continuous digitalization of the chemical industry within the framework of Industry 4.0 has reshaped the way industrial systems are designed, monitored, and optimized. The integration of cyber-physical systems, smart sensors, and real-time analytics enables chemical plants to operate as intelligent networks, capable of self-diagnosis and adaptive control [1, 2]. This paradigm shift promotes the transition from experience-based engineering to data-driven decision-making, where Artificial Intelligence (AI) and Machine Learning (ML) play a central role [3]. These methods allow the extraction of hidden correlations among process variables, supporting predictive maintenance, quality control, and energy optimization [4, 5].

In recent years, numerous studies have demonstrated the applicability of machine learning in chemical and biochemical process modeling. Algorithms such as neural networks, support vector machines, and tree-based models have been employed for reaction kinetics prediction, polymerization monitoring, and wastewater treatment optimization [6-8]. For instance, decision-tree algorithms have been used to identify critical factors influencing bioreactor performance, while regression-based techniques have modeled distillation and crystallization processes with high accuracy [9, 10]. However, while their predictive capabilities are remarkable, many of these algorithms function as black-box models, providing little insight into their internal logic [11].

* Corresponding author: Dumitriana-Roberta-Marina Brănescu, Email address: roberta.branescu@gmail.com

The lack of interpretability raises significant concerns in industrial environments, where process engineers must validate every computational decision affecting safety, quality, and compliance. As chemical operations are subject to strict regulatory and environmental standards, the need for transparent and auditable models becomes essential [12]. Consequently, the emerging field of Explainable Artificial Intelligence (XAI) aims to integrate interpretability into the machine learning workflow, making algorithmic reasoning accessible and trustworthy [13,14]. XAI enhances model transparency by providing explanations for predictions, identifying feature importance, and generating human-readable rules. These mechanisms allow engineers to justify process decisions and detect model inconsistencies before deployment in critical systems [15].

Several categories of explainable algorithms are particularly relevant to chemical process engineering. Intrinsic interpretable models, such as Linear Regression and Decision Trees, provide explicit cause–effect relationships between inputs and outputs. Hybrid models, such as M5P and M5Rules, combine the predictive power of regression analysis with the comprehensibility of rule-based systems, effectively capturing nonlinear interactions [16, 17]. In contrast, post-hoc explanation methods, such as LIME (Local Interpretable Model-Agnostic Explanations) and SHAP (Shapley Additive Explanations), enable the interpretation of complex models after training by approximating local behaviors or computing variable contribution scores [18,19].

In the context of chemical engineering, XAI contributes to several strategic objectives: enhancing process safety, improving energy efficiency, ensuring compliance with the European Artificial Intelligence Act, and fostering human-machine collaboration [20]. These developments align with the broader goal of Industry 4.0, to build intelligent, transparent, and sustainable industrial systems.

The present study investigates the integration of explainable models into chemical process analysis through two representative case studies. The first focuses on the classification of pump operating states using the J48 decision tree algorithm, illustrating fault-detection capabilities through interpretable thresholds. The second addresses the optimization of a distillation column using Linear Regression, M5P, and M5Rules, demonstrating the capacity of interpretable regression models to capture nonlinear process behavior. Together, these examples highlight the balance between predictive performance and interpretability, establishing XAI as a reliable decision-support framework for modern process engineering.

2.1. Datasets description

Two representative datasets were analyzed in this study, each reflecting a specific objective related to the integration of interpretable machine learning models into chemical process analysis. Both datasets were synthetically generated to simulate realistic industrial conditions, ensuring the possibility of controlled experimentation while maintaining physical consistency with reported operational data.

The first case study focused on the diagnosis of pump operating states, aiming to develop a transparent classification framework capable of detecting abnormal conditions based on process measurements. The dataset comprised 100 synthetic instances, each defined by three continuous input variables: temperature (°C), vibration (g), and pressure

(bar) and one categorical output variable corresponding to the operating state (OK or Failure). The objective of this study was to evaluate how rule-based algorithms, such as decision trees, can reproduce the diagnostic reasoning of a process engineer through explicit and human-readable decision thresholds.

The second case study addressed the optimization of a distillation column, with the goal of modeling and interpreting the relationship between specific energy consumption (kWh/t) and key operational parameters. The dataset contained 600 synthetic observations characterized by seven continuous input variables: reflux ratio, top pressure, feed temperature, light-key fraction, column load, ambient temperature, and purity. The aim was to assess how interpretable regression models can capture nonlinear dependencies among variables and support the identification of optimal operating regimes for energy efficiency.

Both datasets were preprocessed to remove inconsistencies and normalized to ensure comparability across variables. Their structure allows a systematic comparison between classification and regression paradigms under explainability constraints. Table 1 presents the key parameters included in both case studies.

Table 1.

Overview of input and output variables used in the two case studies

Case Study	Input variables	Output variable	No. of instances	Type of process
Pump diagnostics	Temperature (°C), Vibration (g), Pressure (bar)	Operating state (OK/Failure)	100	Classification
Distillation column	Reflux ratio, Top pressure, Feed temperature, Light-key fraction, Column load, Ambient temperature, Purity	Specific energy consumption (kWh/t)	600	Regression

2.2. Software and tools

All data analyses and model simulations were carried out using the WEKA 3.8 software platform, an open-source machine learning environment developed at the University of Waikato, New Zealand. The datasets were imported in both CSV and ARFF formats, preprocessed within the WEKA interface, and analyzed using the built-in implementations of Linear Regression, J48, M5P, and M5Rules. All experiments were executed on a standard workstation (Intel i5 processor, 16 GB RAM). This environment ensured full **reproducibility and consistency** across all tested models, providing reliable results for comparative evaluation.

2.3 Applied methods

Four interpretable models were tested, each selected for its relevance within the Explainable Artificial Intelligence (XAI) framework.

The Linear Regression (LR) model provides a global and fully interpretable relationship between inputs and outputs through explicit coefficients. The J48 Decision Tree algorithm constructs human-readable classification rules derived from information gain, offering transparent logic for decision making. The M5P Model Tree method divides the input space into local regions and fits linear regressions within each, thereby capturing nonlinear behaviors while maintaining interpretability. Finally, M5Rules extracts concise rule-based equations from the M5P structure, allowing direct analytical understanding of process relationships and supporting practical implementation in industrial systems.

A schematic representation of the experimental workflow is shown in *Figure 1*.

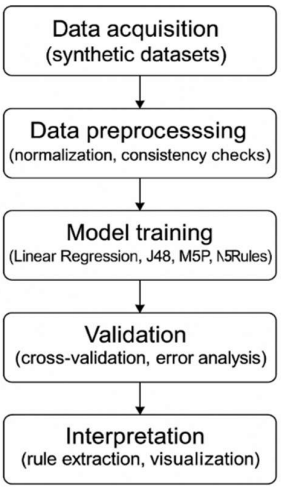

Fig. 1. Workflow for the development and validation of XAI models applied to chemical process data.

3. Results and discussions

3.1. Case Study 1: Pump diagnostics using J48

The first case study focused on the classification of pump operating states using the J48 decision tree algorithm. The dataset included 100 synthetic instances characterized by three operational variables: temperature, vibration, and pressure. After model training, J48 achieved an overall classification accuracy of 98%, confirming the robustness of the model in detecting abnormal behavior.

Figure 2 illustrates the simplified decision tree obtained from the model. The structure highlights vibration as the dominant predictive feature, with a critical threshold at 0.82g. Instances with vibration below this limit were classified as “OK,” while higher values indicated potential mechanical failure.

Such a transparent model provides human-readable rules that can be directly integrated into maintenance systems for early fault detection. The confusion matrix results (not shown) confirmed the stability of the model, with a Kappa coefficient of 0.95 and F-measure of 0.98, emphasizing both precision and reliability.

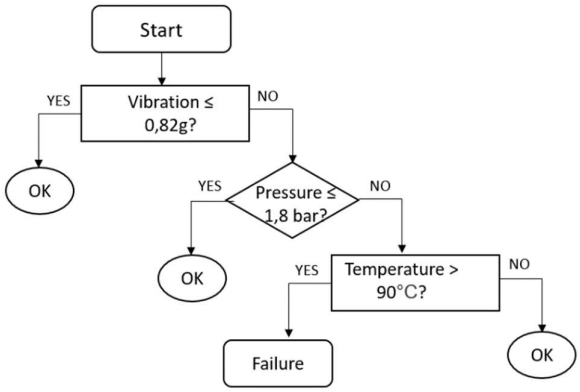

Fig. 2. Simplified J48 decision tree for pump state classification.

3.2. Case Study 2: Distillation column optimization using interpretable regression

The second case study addressed the optimization of a distillation column, aiming to model the relationship between operational parameters and specific energy consumption. The synthetic dataset contained 600 instances and seven input variables, including reflux ratio, top pressure, feed temperature, light-key fraction, column load, ambient temperature, and purity.

Figure 3 shows the nonlinear relationship between the reflux ratio and specific energy consumption (kWh/t). As the reflux ratio increases, energy demand rises exponentially, reflecting the thermodynamic behavior typical of distillation processes. This observation confirms that purely linear models are insufficient to capture system dynamics.

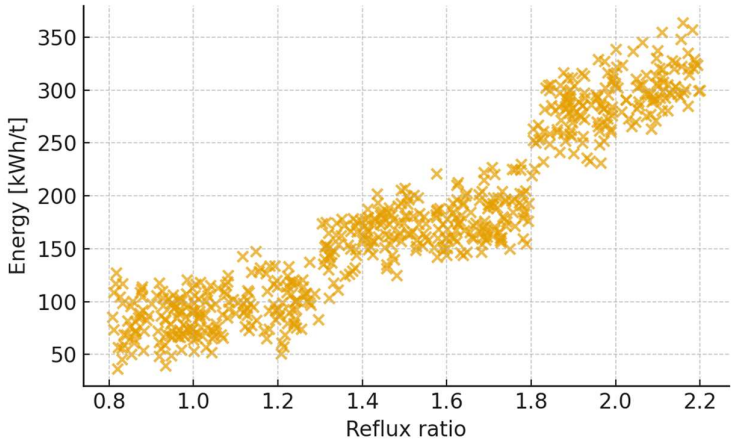

Fig. 3. Relationship between reflux ratio and specific energy consumption in the distillation column.

The Linear Regression (LR) model explained approximately 96.6% of energy variability ($R^2 = 0.966$), but residual analysis revealed systematic deviations in nonlinear regions. To address this limitation, M5P and M5Rules algorithms were implemented. Both models divided the input space into distinct subregions, producing local linear equations or rules that accurately captured nonlinear transitions.

The M5P model achieved an R^2 of 0.995 and an RMSE of 8.27 kWh/t, while the M5Rules model reached similar accuracy with slightly improved interpretability (RMSE = 8.21 kWh/t). Example rules extracted from M5Rules are shown below in Figure 4.

IF Reflux ≤ 1,25 AND *TopPressure* ≤ 0.9
THEN Energy = 85.3 + 42.7·Reflux

IF Reflux > 1,25 AND Purity > 96.5
THEN Energy = 120.8 + 35.2·Reflux

IF Reflux > 1,25 AND Purity ≤ 96.5
THEN Energy = 165.8 + 6.4·Reflux

Fig. 4. Extracted rules and model regions obtained with the M5Rules algorithm.

These interpretable equations enable engineers to visualize how specific process variables influence energy consumption under different operating regimes.

3.3. Comparative interpretation

To compare performance across methods, Table 2 summarizes the predictive accuracy and interpretability of all models used in this study.

Table 2.

Comparison of model performance and interpretability metrics

Model	Type	R^2	RMSE (kWh/t)	Interpretability	Main insight
Linear Regression	Global	0.966	21.29	High	Simple but misses nonlinearities
M5P	Piecewise Tree	0.995	8.27	Very High	Captures local operating trends
M5Rules	Rule-based	0.995	8.21	Excellent	Provides human-readable process rules

These results demonstrate that interpretable regression approaches (M5P and M5Rules) combine **high predictive accuracy** with **transparency**. Their rule-based nature allows for direct industrial application, supporting both **optimization** and **compliance with explainability requirements** of the European AI Act. Taken together, the two case studies confirm that Explainable AI methods represent a practical bridge between **machine learning performance** and **engineering interpretability**, contributing to safer and more sustainable process design.

4. Conclusions

The study demonstrated that Explainable Artificial Intelligence (XAI) can effectively bridge the gap between advanced data analytics and engineering interpretability in chemical process modeling. Using two representative synthetic case studies, interpretable models such as Linear Regression, J48, M5P, and M5Rules achieved both high predictive accuracy and transparent logic, allowing process engineers to validate and trust machine-generated outcomes.

The J48 classifier provided an intuitive fault-diagnosis framework for pump operation, achieving 98% accuracy and delivering explicit vibration-based rules for early maintenance actions. In contrast, the distillation column analysis showed that M5P and M5Rules outperform global Linear Regression, capturing nonlinear interactions between reflux ratio, energy consumption, and purity with near-perfect predictive performance ($R^2 \approx 0.995$).

These results confirm that interpretable models can serve as auditable, high-fidelity decision-support tools in chemical engineering environments where transparency and reliability are critical. Beyond accuracy, their rule-based structure aligns with the principles of the European AI Act, enabling compliance with forthcoming industrial standards for explainability.

Future research should focus on hybrid frameworks that combine interpretable and deep learning components, expanding the scope of XAI toward real-time process control, adaptive optimization, and sustainability assessment across the chemical industry.

REFERENCES

[1] Kagermann, H., Wahlster, W., & Helbig, J. (2013). Recommendations for Implementing the Strategic Initiative INDUSTRIE 4.0: Final Report of the Industrie 4.0 Working Group. Acatech – National Academy of Science and Engineering, Germany.
[2] Lee, J., Bagheri, B., & Kao, H.A. (2015). A Cyber-Physical Systems Architecture for Industry 4.0-Based Manufacturing Systems. Manufacturing Letters, 3, 18–23.
[3] Wuest, T., Weimer, D., Irgens, C., & Thoben, K.D. (2016). Machine Learning in Manufacturing: Advantages, Challenges, and Applications. Production & Manufacturing Research, 4(1), 23–45.
[4] Taboada, M., et al. (2019). Data-driven approaches for wastewater treatment optimization. Environmental Modelling & Software, 120, 104–135.
[5] Lee, J.M., Yoo, C.K., & Qin, S.J. (2018). Process Data Analytics for Smart Manufacturing: An Overview. AIChE Journal, 64(12), 4463–4478.
[6] Leon, F., & Galaction, A.I. (2018). Modeling of fermentation processes using AI techniques. Biochemical Engineering Journal, 137, 154–166.
[7] Ghaemi, M.S., et al. (2020). Machine Learning Approaches for Predicting Polymerization Outcomes. Chemical Engineering Science, 216, 115510.
[8] Wang, L., Zhang, J., & Xu, Y. (2021). Artificial Intelligence Applications in Process Control and Optimization: A Review. Chemical Engineering and Processing, 166, 108505.
[9] Draper, N.R., & Smith, H. (1998). Applied Regression Analysis. Wiley.
[10] Quinlan, J.R. (1992). Learning with Continuous Classes. Proceedings of the 5th Australian Joint Conference on Artificial Intelligence, 343–348.
[11] Molnar, C. (2022). Interpretable Machine Learning: A Guide for Making Black Box Models Explainable. Lulu Press.
[12] European Commission. (2021). Proposal for a Regulation Laying Down Harmonised Rules on Artificial Intelligence (Artificial Intelligence Act). COM/2021/206 final, Brussels.
[13] Doshi-Velez, F., & Kim, B. (2017). Towards a Rigorous Science of Interpretable Machine Learning. arXiv preprint arXiv:1702.08608.
[14] Adadi, A., & Berrada, M. (2018). Peeking Inside the Black-Box: A Survey on Explainable Artificial Intelligence (XAI). IEEE Access, 6, 52138–52160.
[15] Carvalho, D.V., Pereira, E.M., & Cardoso, J.S. (2019). Machine Learning Interpretability: A Survey on Methods and Metrics. Electronics, 8(8), 832.
[16] Wang, Y., & Witten, I.H. (1997). Inducing Model Trees for Continuous Classes. Proceedings of the 9th European Conference on Machine Learning (ECML), Springer, 128–137.
[17] Hall, M., et al. (2009). The WEKA Data Mining Software: An Update. SIGKDD Explorations, 11(1), 10–18.
[18] Ribeiro, M.T., Singh, S., & Guestrin, C. (2016). Why Should I Trust You? Explaining the Predictions of Any Classifier. Proceedings of the 22nd ACM SIGKDD International Conference on Knowledge Discovery and Data Mining, 1135–1144.
[19] Lundberg, S.M., & Lee, S.I. (2017). A Unified Approach to Interpreting Model Predictions. Advances in Neural Information Processing Systems (NeurIPS), 30, 4765–4774.
[20] Fernández, A., Del Ser, J., & Hussain, A. (2020). Explainable Artificial Intelligence for Industry: Concepts, Applications, and Challenges. IEEE Access, 8, 153993–154017.

DETERMINATION OF PHYSICO-CHEMICAL PROPERTIES AND STABILITY ASSESSMENT OF NANOFUELS CONTAINING MULTI-WALLED CARBON NANOTUBES

Andrei Laurentiu NICULAE[1,*], Ioan CALINESCU[2], Petre CHIPURICI[2], Radu CHIRIAC[1,3]

[1]National University of Science and Technology Politehnica Bucharest, Faculty of Mechanical Engineering and Mechatronics, 313 Splaiul Independentei, 060042, Bucharest, Romania
[2]National University of Science and Technology Politehnica Bucharest, Faculty of Chemical Engineering and Biotechnology, 1-7 Gheorghe Polizu, 011061, Bucharest, Romania
[3]EA7341 CMGPCE of Conservatoire National des Arts et Metiers, Paris, France

Abstract

The addition of nanoparticles to fuels can modify their physicochemical properties, although previous studies have not revealed a clear pattern in these variations. In this study, density, viscosity, and stability were evaluated for a commercial B7 diesel fuel blended with 25, 50, and 100 ppm multi-walled carbon nanotubes (MWCNTs), using 5% n-butanol as the solvent. Span 60 surfactant was used for one sample. The impact on density was minimal, while viscosity varied between −2.21% and +2.56%. Dynamic light scattering (DLS) measurements demonstrated good stability for fuels containing 25 and 50 ppm MWCNTs, whereas significant instability was observed at 100 ppm.

Keywords: Nanofuels, Multi-walled carbon nanotubes, Diesel, Stability, Physico-chemical properties, Fuel additives

1. Introduction

Improving fuel atomization and combustion efficiency while reducing pollutant emissions remains a major challenge for internal combustion engines, and the use of nanoparticles as fuel additives has emerged as a promising solution. One important advantage of nanoparticle-containing emulsion fuels is their ability to induce puffing and micro-explosions, which promote secondary breakup and thereby enhance liquid fuel atomization [1]. However, fuel spray development is also strongly influenced by its physico-chemical properties, some of which can be modified through the addition of nanoparticles [2]. Density and viscosity play a key role in spray development by directly influencing droplet breakup and atomization. Higher values of these properties result in slower and less efficient atomization. As reported in [3], increasing density and viscosity prolongs jet breakup time and reduces the spray cone angle, which indicates poorer

* Corresponding author email address: andrei.niculae@upb.ro

atomization due to slower jet disintegration and vaporization. In contrast, penetration increases, thus allowing the jet to travel a longer distance inside the combustion chamber.

Concerns regarding the potential toxicity of metallic fuel additives have motivated the use of less harmful, non-metallic catalysts [4]. MWCNTs, as carbon-based nanoparticles, represent a promising alternative because of their lower environmental impact.

Fig. 1 illustrates the percentage variations in the density of fuels doped with MWCNTs as a function of nanoparticle concentration. The figure was constructed using the relative differences calculated between the density values reported in [5–13] for the nanofuels and the corresponding base fuels, with the base fuel values taken as reference. At ppm-level concentrations, the actual amount of MWCNTs added to the fuel is extremely small. In terms of total mass, these nanoparticles represent only a negligible fraction of the fuel. Consequently, they do not produce a significant impact on fuel density, as reflected by the low average percentage variations, which remain below 0.7%. These minor fluctuations are within acceptable limits and are most likely the result of measurement uncertainties. However, exceptions were observed in study [7], where larger density increases of 0.86% at 25 ppm, 1.62% at 50 ppm, and 2.35% at 100 ppm were calculated based on the reported values. These deviations may be attributed to the use of surfactants or solvents at higher concentrations.

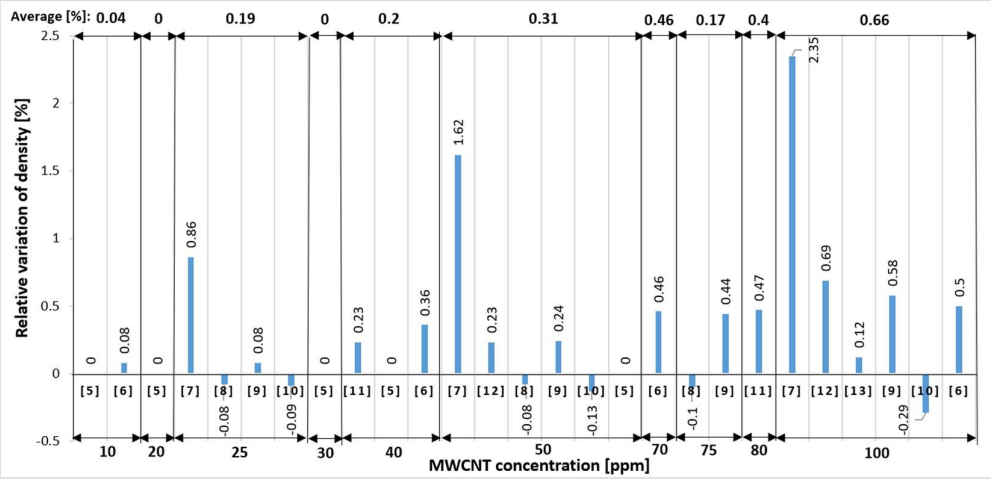

Fig. 1. Relative variation of density as a function of MWCNT concentration

Fig. 2 illustrates the percentage variations in the kinematic viscosity of fuels doped with MWCNTs as a function of nanoparticle concentration. The figure was constructed using the relative differences calculated between the kinematic viscosity values reported in [5–13] for the nanofuels and the corresponding base fuels, with the base fuels' values taken as references. The addition of MWCNT nanoparticles affects the kinematic viscosity of the fuels, showing both increasing and decreasing trends. However, for most fuels and concentrations considered, nanoparticle addition leads to an increase in viscosity, with maximum reported values of up to 29.51% at 100 ppm. This

increase can be attributed to the formation of nanoparticle networks or agglomerates within the fluid, leading to a significant rise in internal resistance and, consequently, in viscosity. Reported viscosity reductions of up to 15.25% suggest that, in some cases, nanoparticle dispersion may also have a fluidizing effect, reducing the flow resistance of the fuel. The maximum viscosity decrease of 15.25% was recorded at a concentration of 100 ppm MWCNT with the addition of 2% surfactant. These variations highlight that the effects depend not only on nanoparticle concentration but also on the fuel composition and the use of surfactants to achieve effective dispersion. No clear or consistent trend in this parameter with nanoparticle dosage can be identified.

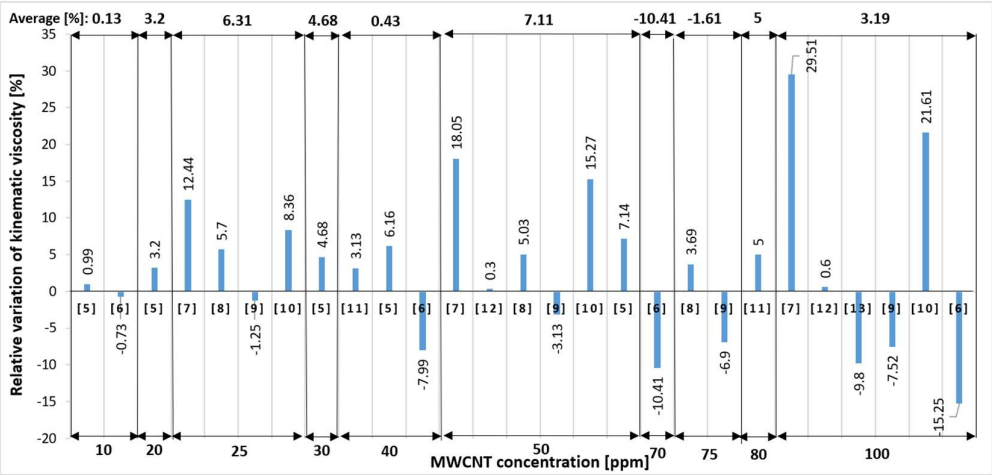

Fig. 2. Relative variation of kinematic viscosity as a function of MWCNT concentration

Since the variation of kinematic viscosity, calculated based on values reported in the literature [5–13], did not reveal a well-defined trend, it was considered necessary to perform experimental measurements. Therefore, a commercial B7 diesel fuel was blended with 25, 50, and 100 ppm MWCNTs, using 5% n-butanol as the solvent. The density and kinematic viscosity of the resulting nanofuels were then experimentally determined. Span 60 surfactant was added to one sample at 1 wt.% of the n-butanol fraction. Furthermore, the stability of the prepared nanofuels was assessed by dynamic light scattering (DLS) measurements.

2. Experimental

Preparation of Carbon-Based Nanofuels

To facilitate nanoparticle dispersion and ensure optimal homogenization of the blends, n-butanol ($C_4H_{10}O$) was used as the solvent. Compared to short-chain alcohols such as methanol (CH_3OH) and ethanol (C_2H_5OH), n-butanol offers significant advantages when mixed with diesel fuel. These include superior miscibility, a lower tendency for water absorption (reduced hydrophilicity), and physicochemical properties that are closer to those of diesel fuel [14].

The prepared fuel blends were labeled according to their composition. The base fuel, denoted B7S5, consisted of 95% commercial B7 diesel and 5% n-butanol. Three additional blends were obtained by doping the base fuel with unfunctionalized MWCNTs at different concentrations: B7S5C25 (25 ppm), B7S5C50 (50 ppm), and B7S5C100 (100 ppm). A fifth blend, B7S5C100-S, was formulated by adding 100 ppm unfunctionalized MWCNTs and 1 wt.% surfactant relative to the n-butanol fraction.

For the preparation of the B7S5C100-S fuel, Span 60 was selected as the surfactant. The choice was based on its hydrophilic-lipophilic balance (HLB), a parameter used to describe the ratio between the hydrophilic (water-soluble) and lipophilic (oil-soluble) components of a surfactant. HLB values range from 0 to 20. Surfactants with HLB values below 10 are predominantly lipophilic, showing higher affinity for oily substances, with this effect becoming more pronounced as the value decreases. Conversely, surfactants with HLB values above 10 are mainly hydrophilic and have a higher affinity for water. Span 60 has an HLB value of 4.3, which makes it suitable for use in diesel fuel [15].

The unfunctionalized MWCNT nanoparticles were procured from SkySpring Nanomaterials, Inc. (USA). They were produced by catalytic chemical vapor deposition (CCVD), and their specifications are presented in Table 1.

Table 1.

Specifications of the unfunctionalized MWCNT nanoparticles

Purity	Outer diameter	Inner diameter	Length	Bulk density	Real density
>95% (wt.)	<8 nm	2-5 nm	5-20 μm	0,27g/cm^3	~2,1 g/cm^3

For weighing the nanoparticles and the Span 60 surfactant, an analytical balance with internal self-calibration (KERN ADJ 200-4) was used. This equipment ensures high precision, with a maximum weighing capacity of 220 g, a repeatability of 0.2 mg, a readability of 0.1 mg, and a linearity of ±0.4 mg [16]. The volumes of n-butanol and B7 required for each sample were then measured using graduated cylinders.

Table 2 presents the composition of the prepared fuels. The B7S5C25, B7S5C50, and B7S5C100 blends were prepared in four batches, each with a volume of 4 liters, resulting in a total volume of 16 liters per blend. The table details the volume and composition of each batch (B7 and n-butanol) as well as the corresponding amount of MWCNTs added during preparation. The B7S5 and B7S5C100-S fuels were prepared in a single batch.

Table 2.

Composition of the prepared fuels

Fuel	Total volume per batch (mL)	Volume of B7 per batch (mL)	Volume of n-butanol per batch (mL)	Amount of MWCNT per batch	Surfactant mass (Span 60) (mg)
B7S5	1600	15200	800	-	-
B7S5C25	4000	3800	200	83 mg (25 ppm)	-
B7S5C50	4000	3800	200	166 mg (50 ppm)	-
B7S5C100	4000	3800	200	332 mg (100 ppm)	-
B7S5C100-S	800	760	40	64.8 mg (100 ppm)	330

The first step in the preparation of the B7S5C25, B7S5C50, and B7S5C100 fuels consisted of ultrasonic homogenization. A volume of 200 mL of n-butanol, 50 mL of B7, and the corresponding amounts of MWCNTs specified in Table 2 were placed in the reactor. The total volume subjected to ultrasonic homogenization was therefore 250 mL, corresponding to the maximum capacity of the Sonics Vibra-Cell probe. The temperature in the reactor was maintained at 5 °C by a water circulation system connected to a Thermo Scientific AC 200 circulator. The ultrasonic probe was inserted 2 cm into the reactor. The effective sonication time was set to 20 minutes, with an ON/OFF cycle of 10 s/10 s and an amplitude of 50%. The ON/OFF mode of 10 s/10 s means that the probe operates in cycles, each consisting of 10 seconds of sonication followed by a 10 second pause. These cycles continue until a total process time of 40 minutes is reached, corresponding to an effective ultrasonic homogenization time of 20 minutes. For the B7S5 fuel, the specified amounts of B7 and n-butanol were added to a vessel and manually mixed. For the preparation of B7S5C100-S, 40 mL of n-butanol, 64.8 mg of MWCNTs, and 330 mg of Span 60 surfactant were introduced into the reactor. The effective sonication time was set to 10 minutes, with the same ON/OFF cycle of 10 s/10 s and an amplitude of 30%. Fig. 3 presents the equipment employed in this phase of the preparation process.

Fig. 3. Ultrasonic homogenizer Sonics Vibra-Cell, temperature-controlled reactor, and Thermo Scientific AC 200 circulator

The homogenized mixture was subsequently transferred to a vessel containing 3750 mL of B7 for B7S5C25, B7S5C50, and B7S5C100 or 760 mL for B7S5C100-S (Fig. 4a). A second homogenization step was then performed using a mechanical stirrer. For B7S5C25, B7S5C50, and B7S5C100, mixing was carried out for 40 minutes at 20,000 rpm, whereas for B7S5C100-S it was conducted for 15 minutes at 15,200 rpm (Fig. 4b). Fig. 4c shows samples of the prepared fuels corresponding to different nanoparticle concentrations.

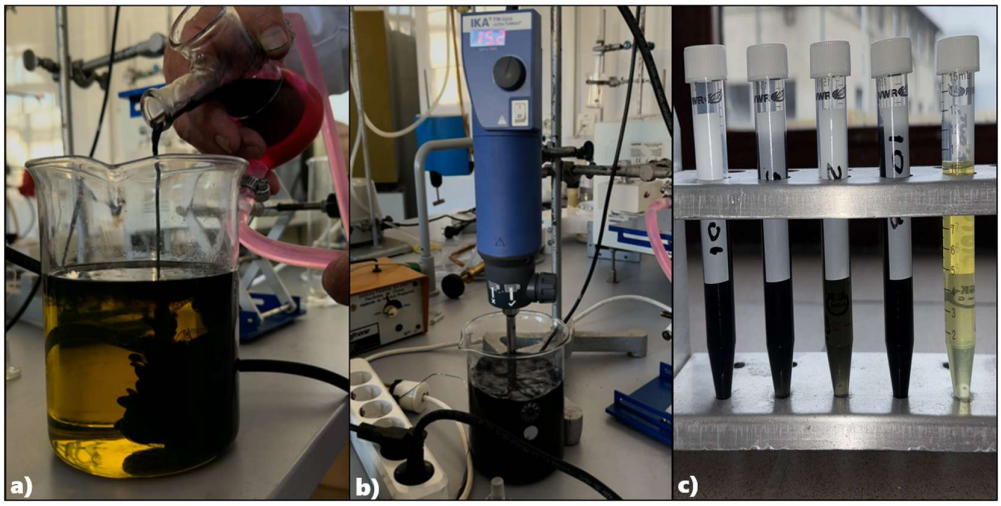

Fig. 4. **a)** Vessel containing the B7 volume to which the homogenized mixture is added; **b)** Additional homogenization step performed using the Ultra Turrax mechanical stirrer; **c)**Samples of the prepared fuels, from left to right: B7S5C100, B7S5C50, B7S5C25, B7S5C100-S, and B7S5

Density Determination Procedure

Fuel density was determined using a pycnometer, a widely applied method for assessing the density of petroleum products. The device consists of a vessel with a precisely calibrated volume, which is filled with the fuel to be analyzed. It is equipped with a perforated stopper that allows excess liquid to escape, ensuring that the final volume of fuel exactly matches the pycnometer's nominal volume.

The measurement procedure involves weighing the empty pycnometer first, then weighing it again after filling it with the test fuel. The temperature of the fuel is also measured using a thermometer, as density is temperature-dependent. The density is then calculated according to Equation (2).

Since the SR EN 590:2022 standard [17] specifies the reference density of diesel at 15 °C, Equation (3) was applied to correct the measured density to this temperature.

Additionally, density values at 40 °C were determined using the same correction method, as these are required for kinematic viscosity measurements at this temperature.

The following calculation formulas were used [18]:

$$m_f = m_{pf} - m_p \quad (1)$$

$$\rho^t = \frac{m_f}{V_p} \quad (2)$$

$$\rho^{t'} = \rho^t + c \cdot (t - t') \quad (3)$$

Where:

- m_f = mass of the fuel (g);
- m_{pf} = mass of the pycnometer filled with fuel (g);
- m_p = mass of the empty pycnometer (g);
- ρ^t = fuel density at the measurement temperature t (g/cm^3);
- V_p = volume of the pycnometer (cm^3);
- $\rho^{t'}$ = fuel density at the temperature t' (g/cm^3);
- c = correction coefficient for the variation of density with a 1 °C change in temperature (g/ (cm^3 · °C)).

Table 3 presents the correction coefficient values for petroleum products as a function of the density measured at the test temperature.

Table 3.

Mean density correction coefficients for petroleum products [18]

ρ^t (g/cm^3)	c (g/cm^3·°C)	ρ^t (g/cm^3)	c (g/cm^3·°C)	ρ^t (g/cm^3)	c (g/cm^3·°C)
0.6900-0.6999	0.000910	0.8000-0.8099	0.000765	0.9100-0.9199	0.000620
0.7000-0.7099	0.000897	0.8100-0.8199	0.000752	0.9200-0.9299	0.000607
0.7100-0.7199	0.000884	0.8200-0.8299	0.000738	0.9300-0.9399	0.000594
0.7200-0.7299	0.000870	0.8300-0.8399	0.000725	0.9400-0.9499	0.000581
0.7300-0.7399	0.000857	0.8400-0.8499	0.000712	0.9500-0.9599	0.000567
0.7400-0.7499	0.000844	0.8500-0.8599	0.000699	0.9600-0.9699	0.000554
0.7500-0.7599	0.000831	0.8600-0.8699	0.000685	0.9700-0.9799	0.000541
0.7600-0.7699	0.000818	0.8700-0.8799	0.000673	0.9800-0.9899	0.000528
0.7700-0.7799	0.000805	0.8800-0.8899	0.000660	0.9900-1.0000	0.000515
0.7800-0.7899	0.000792	0.8900-0.8999	0.000647	-	-
0.7900-0.7999	0.000778	0.9000-0.9099	0.000633	-	-

Viscosity Measurement Procedure

Viscosity measurements were carried out using an Ostwald viscometer, also known as a capillary viscometer. This device is widely used to determine the viscosity of liquids with known density [19]. Its operating principle is based on measuring the flow time of the test fuel and a reference liquid between two fixed marks under the influence of gravity, at a temperature of 40 °C maintained with high precision [20].

Fig. 5a shows a schematic representation of the Ostwald viscometer. The liquid to be tested is introduced through the filling section (indicated by the arrow) until the level in the large reservoir reaches approximately two-thirds of its height. A suction pump connected to the opposite end of the viscometer is then used to draw the liquid slightly above the upper mark. The flow time of the liquid between the upper and lower marks is precisely measured. The Ostwald viscometer and a thermometer used to monitor the temperature are placed in a thermostatic bath to ensure stable thermal conditions during measurements. The viscometer is firmly secured in a support stand to maintain precise vertical alignment (Fig. 5b).

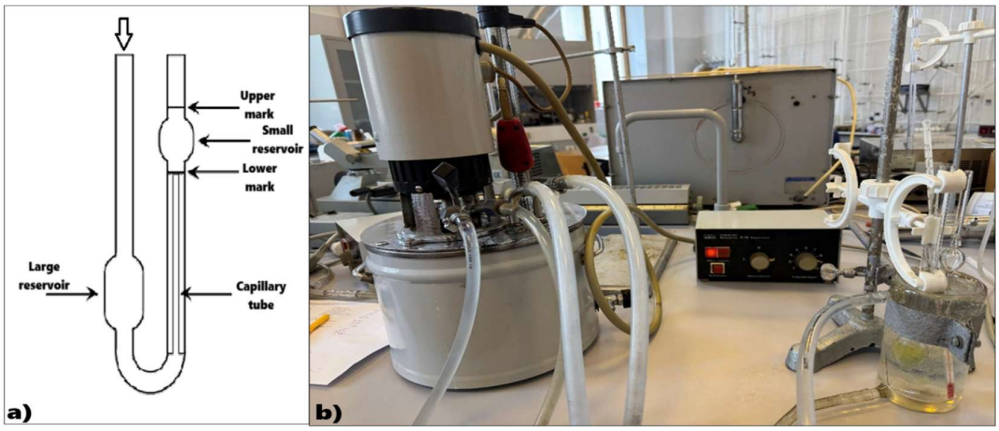

Fig. 5. **a)** Schematic representation of an Ostwald viscometer [21]; **b)** Thermostatic bath containing the Ostwald viscometer and a thermometer for temperature monitoring

According to [20], the relative dynamic viscosity of the tested fuel (η_f), expressed in cP, is determined using the following equation:

$$\eta_f = \eta_r \cdot \frac{t_f \cdot \rho_f}{t_r \cdot \rho_r} \tag{4}$$

Where:

- η_r = dynamic viscosity of the reference liquid (cP);
- t_f = flow time of the tested fuel (s);
- t_r = flow time of the reference liquid (s);
- ρ_f = density of the tested fuel at 40 °C (kg/m^3);
- ρ_r = density of the reference liquid at 40 °C (kg/m^3).

The kinematic viscosity of the tested fuel (ν_f), expressed in mm^2/s, is determined using the following equation:

$$\nu_f = \frac{\eta_f(cP)\cdot 10^3}{\rho_f(kg/m^3)} \tag{5}$$

The reference liquid used in the measurements was distilled water, with a dynamic viscosity of η_r=0,656 cP, a flow time of t_r = 79 s, and a density of ρ_r = 992,2 kg/m^3.

To assess the reproducibility of the results, flow time measurements were conducted in three distinct experimental sets (Sets 1, 2, and 3), performed at one-week intervals. For the B7 fuel, measurements were taken only in Set 1. The B7S5C25, B7S5C50, and B7S5C100 fuels were analyzed in all three sets, while B7S5 and B7S5C100-S were analyzed in two sets (Sets 1 and 3, and Sets 2 and 3, respectively). For each sample, several flow time measurements were taken, and the arithmetic mean was calculated. This average value was then used to determine the dynamic viscosity using equation (4) and the kinematic viscosity using equation (5).

Stability Evaluation Procedure for Nanofuels

The stability of nanofuels can be evaluated using a dynamic light scattering (DLS) system [22]. DLS measurements are performed in accordance with ISO 22412:2017, which describes the operating principle of the method. According to this standard [23], the Brownian motion of particles suspended in a fluid, combined with the Stokes–Einstein theory, enables the estimation of the hydrodynamic diameter based on the diffusion rate in a medium of known temperature and viscosity. The DLS method relies on detecting light scattered by the suspended particles. The intensity and frequency of the scattered light vary depending on the diffusion rate, which in turn is influenced by the particles' hydrodynamic diameter, as well as by the viscosity and temperature of the fluid. For accurate analysis, the viscosity, temperature, and refractive index of the fuel must be known, since these parameters are required to calculate the hydrodynamic diameter estimated by DLS.

The hydrodynamic diameter represents the size of a hypothetical sphere that has the same translational diffusion coefficient as the analyzed particle. This value does not exclusively reflect the physical size of the particle but also accounts for its interactions with the surrounding medium. When a dispersed particle moves through a liquid, a layer of electric dipoles known as the electric double layer forms and adheres to its surface [24]. As a result, the hydrodynamic diameter is generally larger than the actual particle diameter.

The refractive index is defined as the ratio between the speed of light in a vacuum and its speed in the test medium [25]. It was measured using an Abbe Krüss AR-2 refractometer, which has a measurement range of 1.3–1.7 and a resolution of 0.001 [26].

DLS analyses were performed using a Beckman Coulter N4 Plus system, which is capable of measuring particle sizes in suspension ranging from 3 nm to 3 μm. The instrument is equipped with an optical system comprising six fixed-angle optical fibers positioned at 14.9°, 20.6°, 30.4°, 40.2°, 50.4°, and 90°. This configuration enables multi-angle particle analysis, improving the accuracy of the measurements [27]. DLS tests were

carried out for the B7S5C25, B7S5C50, and B7S5C100 samples two months after preparation and were then repeated after ultrasonic redispersion.

3. Results and discussions

Density of the Investigated Fuels

Fig. 6 presents the density values of the fuels at 15 °C and 40 °C, together with the relative differences calculated for the nanoparticle-doped blends, using the base fuel (B7S5) as reference. Because the butanol content in B7S5 is only 5%, its density is very similar to that of B7. The addition of nanoparticles at concentrations of 25, 50, and 100 ppm, as well as the use of Span 60 surfactant in B7S5C100-S, resulted in slight density reductions ranging from 0.16 % to 0.64 %. These small variations can likely be attributed to uncertainties associated with the measurement method. The calculated relative differences confirm that the influence of nanoparticles on fuel density is negligible at ppm-level dosages. It is worth noting that all prepared fuels exhibit density values at 15 °C within the limits specified by SR EN 590:2022 [17] for commercial diesel during the transition period — classes D and E (815–845 kg/m³).

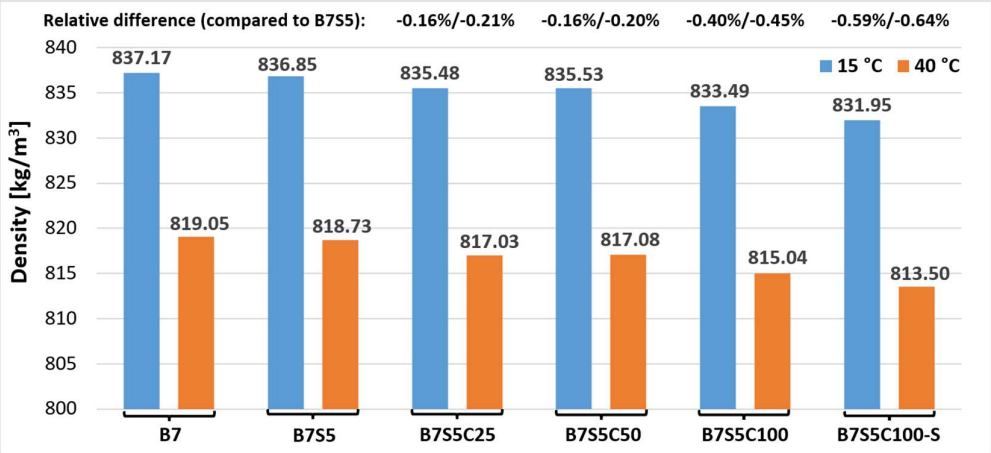

Fig. 6. Fuel density at 15 °C and 40 °C and relative differences compared to B7S5

Viscosity of the Investigated Fuels

Fig. 7 presents the kinematic viscosity values of the fuels at 40 °C, determined across three measurement sets, together with the calculated average values and relative differences for the nanoparticle-doped fuels, taking B7S5 as the reference. The presence of n-butanol in B7S5 leads to a 9.24% decrease in viscosity compared to B7. The addition of 25 ppm MWCNTs results in a further 2.21% reduction relative to B7S5, whereas higher concentrations cause slight increases of 2.77% at 50 ppm and 2.56% at 100 ppm.

The addition of Span 60 surfactant in B7S5C100-S leads to a 1.99% decrease in viscosity. The B7S5C100 sample exhibited higher data dispersion. Reduced stability was observed after one week, with visible nanoparticle sedimentation at the bottom of the vessel. This agglomeration likely influenced the flow through the Ostwald viscometer capillary tube, which may explain why the data presented in Fig. 2, constructed from literature sources [5–13], did not show a clear trend in viscosity variation with MWCNT concentration. Ensuring good sample stability is therefore crucial to avoid disturbances in flow during viscosity measurements. The reduced viscosity dispersion observed for B7S5C100-S compared to B7S5C100 highlights the stabilizing effect of Span 60. It is worth noting that all prepared fuels exhibited viscosity values within the range specified by SR EN 590:2022 [17] (2–4.5 mm²/s).

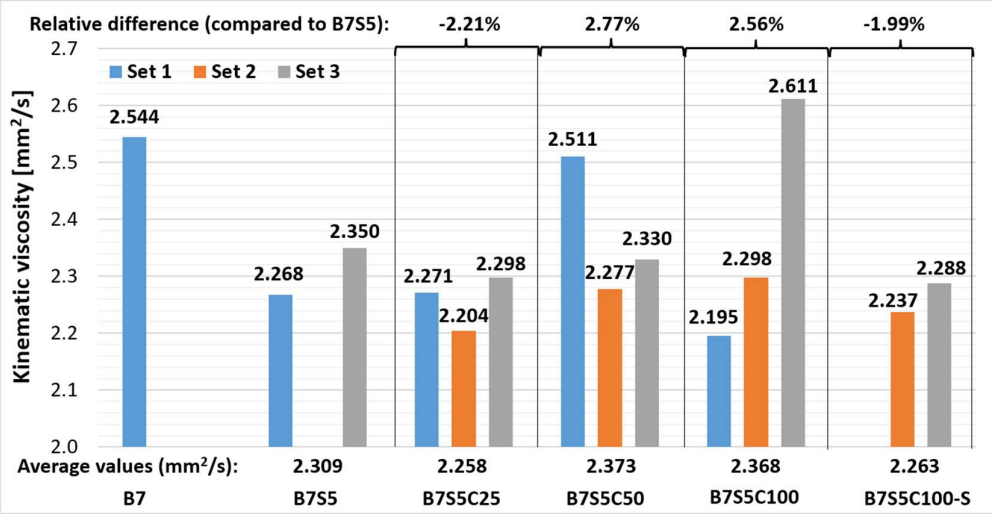

Fig. 7. Kinematic viscosity of the investigated fuels at 40 °C

Stability of Nanofuels

Table 4 presents the refractive index values determined for nanofuels without surfactant. The results show similar values regardless of the MWCNT concentration.

Table 4.

Refractive index values for B7S5C25, B7S5C50, and B7S5C100 nanofuels

Fuel	B7S5C25	B7S5C50	B7S5C100
Refractive index	1.456	1.456	1.4517

Figs. 8a and 8b present the light scattering intensity profiles as a function of particle size for the B7S5C25 nanofuel, measured two months after preparation (a) and following ultrasonic redispersion (b). The results indicate that carbon nanotubes are organized in aggregates with average sizes of approximately 307.4 nm in the non-

redispered sample and about 275.9 nm in the redispered one. In both cases, the presence of a single, well-defined peak reflects a monodisperse particle size distribution. Two months after preparation, the hydrodynamic diameter ranged between 303.6 and 311.8 nm, exceeding the redispered values (272.2–279.6 nm), which is consistent with aggregate growth during storage. Nevertheless, the increase was relatively modest, suggesting that the sample retained a good degree of stability over time. The results also show good reproducibility, with no significant differences between repeated measurements. The low standard deviation values (20.5–33.4 nm for the non-redispered sample and 34.8–37.2 nm for the redispered one) indicate a narrow distribution of aggregate sizes in both cases, suggesting limited variability in particle size.

Figs. 8c and 8d show the corresponding profiles for the B7S5C50 nanofuel, also recorded after two months of storage (c) and after ultrasonic redispersion (d). The average aggregate size was approximately 276.1 nm in the non-redispered sample and decreased to about 202.5 nm after redispersion. Similar to the B7S5C25 nanofuel, a single peak was observed in both distributions, indicating monodispersity. The hydrodynamic diameter after two months (272.2–281.4 nm) was slightly larger than that of the redispered sample (199.7–205 nm), reflecting moderate aggregate growth during storage. Compared to the lower concentration (25 ppm), a more pronounced increase in aggregate size was observed at 50 ppm during storage, confirming that increased MWCNT concentration promotes agglomeration. Similarly, the measurements in this case exhibited only minor differences, indicating good reproducibility. The standard deviation values ranged from 34.0 to 36.8 nm for the non-redispered sample and from 24.1 to 27.4 nm for the redispered one. These low values indicate that the aggregate sizes remained confined to a narrow range, consistent with the results obtained at the 25 ppm concentration.

Figs. 8e and 8f display the results for the B7S5C100 nanofuel. Unlike the lower concentrations, the non-redispered sample exhibited marked polydispersity and a high degree of agglomeration. Multiple peaks appeared in different size ranges, with the main fraction located between 100 and 200 nm, while additional peaks revealed the presence of larger aggregates ranging from 300 to 3000 nm. This heterogeneity is reflected in the wide variability of hydrodynamic diameters (150.6–561.7 nm) and in the large standard deviations (28.6–1151.6 nm), which are substantially higher than those observed for the 25 and 50 ppm samples. After redispersion, the distribution narrowed considerably, with intensity peaks concentrated between 150 and 200 nm. The hydrodynamic diameter range (156.1–236.5 nm) and standard deviations (31.1–184.5 nm) decreased substantially, though variability remained slightly elevated, indicating a lower stability of the redispersed sample. In summary, increasing the MWCNT concentration to 100 ppm leads to more pronounced aggregation and a broader particle size distribution during storage. These findings confirm that higher nanoparticle concentrations enhance agglomeration tendencies, and that achieving long-term stability at such concentrations may require the use of functionalized nanoparticles or appropriate surfactants.

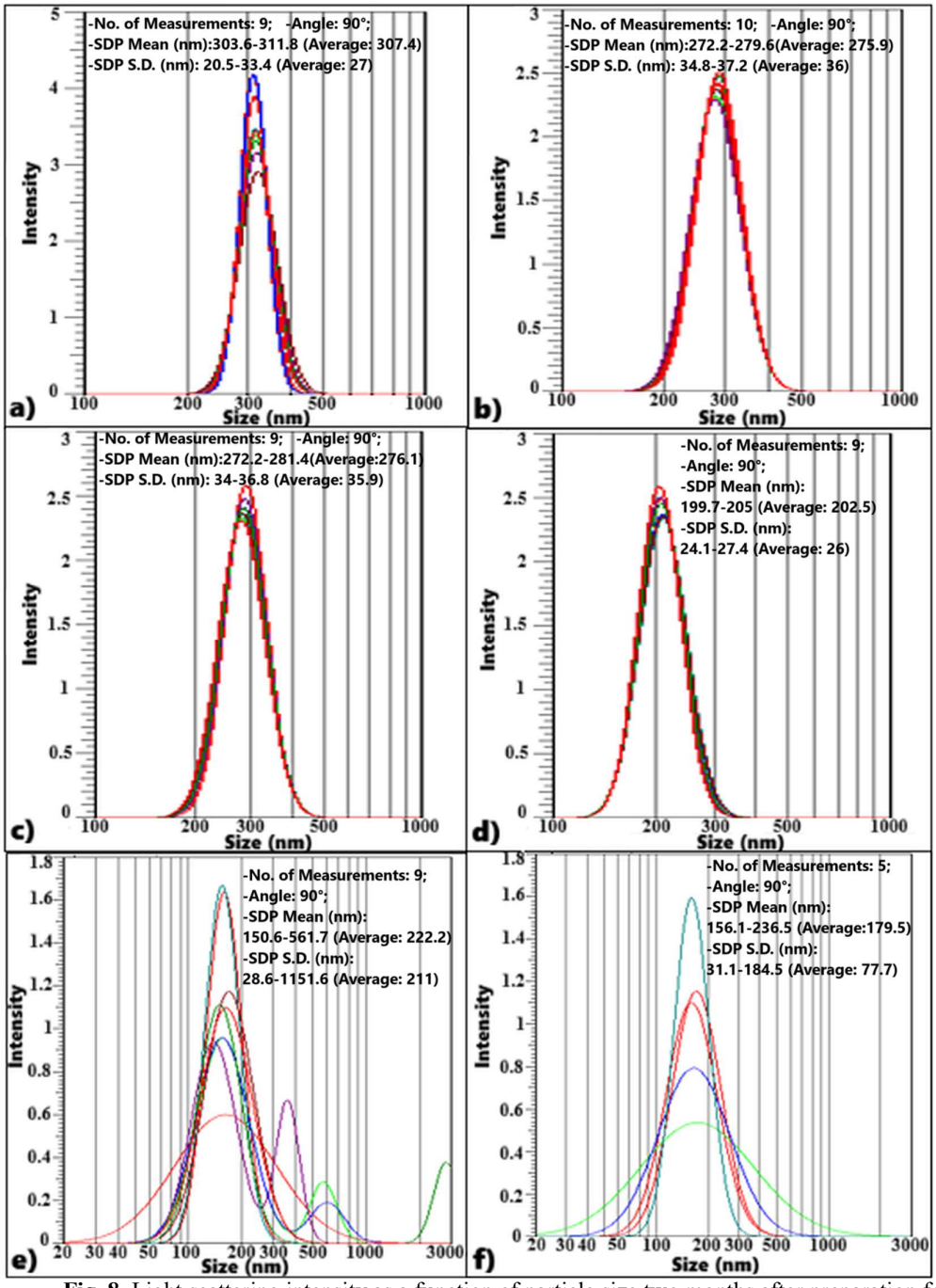

Fig. 8. Light scattering intensity as a function of particle size two months after preparation for: a) B7S5C25, c) B7S5C50, e) B7S5C100, and after ultrasonic redispersion for: b) B7S5C25, d) B7S5C50, f) B7S5C100

In [28], a stability study was carried out for B10 fuel doped separately with 100 mg/L of unfunctionalized and amide-functionalized MWCNTs. DLS measurements were performed immediately after preparation and over three consecutive days. The nanoparticles were supplied by the same manufacturer (SkySpring Nanomaterials, Inc., USA). When comparing the particle size values obtained two months after preparation in this study with those reported in [28], the measured sizes (222.2–307.4 nm) were significantly lower than those for unfunctionalized MWCNT dispersions (4146–4404 nm) and even those for functionalized dispersions (2431–4895 nm). These results indicate that the preparation method adopted in this work provides improved nanoparticle dispersion stability compared to the approach reported in [28].

4. Conclusions

In this study, the density and viscosity of a commercial B7 diesel fuel were determined and compared with those of the same fuel doped with unfunctionalized MWCNTs at different concentrations. To promote nanoparticle dispersion and ensure proper homogenization of the blends, n-butanol was used as the solvent. For the B7S5C100-S sample, the Span 60 surfactant was additionally used. The refractive index was measured, and the stability of the nanoparticle-doped fuels was evaluated through DLS analysis.

The main conclusions are as follows:

- All prepared fuels exhibit density values at 15 °C that comply with the limits defined by SR EN 590:2022 for the transition period. The calculated relative differences confirm that the effect of MWCNTs on density is minimal due to their low (ppm-level) concentrations.
- The presence of n-butanol in B7S5 reduced viscosity by 9.24% compared to B7. Doping with 25 ppm of MWCNTs further decreased viscosity by 2.21% relative to B7S5. At higher concentrations, viscosity increased by 2.77% (50 ppm) and 2.56% (100 ppm). The addition of Span 60 surfactant in B7S5C100-S led to a 1.99% reduction. All viscosity values remained within the range required by SR EN 590:2022.
- Adequate sample stability is essential to ensure a steady and uniform fuel flow through the capillary tube. The use of Span 60 surfactant improved the stability of B7S5C100-S compared to B7S5C100 by reducing the variability of kinematic viscosity measurements.
- DLS measurements demonstrated good stability for fuels containing 25 ppm and 50 ppm of MWCNTs. At higher concentrations, stability may be enhanced using functionalized nanoparticles or the Span 60 surfactant.

Future work will address the influence of these nanofuels on spray development, engine performance, and emissions.

REFERENCES

[1] H. Zhang, Z. Lu, T. Wang, Z. Che, Micro-explosion of emulsion droplets with nanoparticles at high temperature, International Journal of Heat and Mass Transfer 219 (2024). https://doi.org/10.1016/j.ijheatmasstransfer.2023.124851.

[2] K. Kannaiyan, A. AlDosari, R. Sadr, Effects of nanoscale fuel additives on properties and non-reacting spray performance of alternative, conventional and blended jet fuels at elevated ambient conditions, Fuel Processing Technology 208 (2020). https://doi.org/10.1016/j.fuproc.2020.106436.

[3] M. Hawi, H. Kosaka, S. Sato, T. Nagasawa, A. Elwardany, Effect of injection pressure and ambient density on spray characteristics of diesel and biodiesel surrogate fuels, Fuel 254 (2019). https://doi.org/10.1016/j.fuel.2019.115674.

[4] A. Ahmed, A. N. Shad, A. Azam, G. M. Uddin, M. S. Ali, S. Hassan, H. Ahmed, T. Aslam, Environment-friendly novel fuel additives: Investigation of the effects of graphite nanoparticles on performance and regulated gaseous emissions of CI engine, Energy Conversion and Management 211 (2020). https://doi.org/10.1016/j.enconman.2020.112748.

[5] A.I. El-Seesy, A.K. Abdel-Rahman, M. Bady, S. Ookawara, Performance, combustion, and emission characteristics of a diesel engine fueled by biodiesel-diesel mixtures with multi-walled carbon nanotubes additives, Energy Conversion and Management 135 (2017) 373–393. https://doi.org/10.1016/j.enconman.2016.12.090.

[6] N.M. Nachippan, M. Parthasarathy, P.V. Elumalai, A. Backiyaraj, D. Balasubramanian, A.T. Hoang, Experimental assessment on characteristics of premixed charge compression ignition engine fueled with multi-walled carbon nanotube-included Tamanu methyl ester, Fuel 323 (2022). https://doi.org/10.1016/j.fuel.2022.124415.

[7] J.B. Ooi, C.C. Kau, D.N. Manoharan, X. Wang, M.V. Tran, Y.M. Hung, Effects of multi-walled carbon nanotubes on the combustion, performance, and emission characteristics of a single-cylinder diesel engine fueled with palm-oil biodiesel-diesel blend, Energy 281 (2023). https://doi.org/10.1016/j.energy.2023.128350.

[8] E. Arslan, M. Raşit Atelge, N. Kahraman, S. Ünalan, B.A. Çeper, Examination of the effect on the engine of diesel-nanoparticle mixture with natural gas addition, Fuel 357 (2024). https://doi.org/10.1016/j.fuel.2023.129911.

[9] H. Solmaz, S.M.S. Ardebili, A. Calam, E. Yılmaz, D. İpci, Prediction of performance and exhaust emissions of a CI engine fueled with multi-wall carbon nanotube doped biodiesel-diesel blends using response surface method, Energy 227 (2021). https://doi.org/10.1016/j.energy.2021.120518.

[10] B. Ittoo, J.B. Ooi, M.V. Tran, F. Jaliliantabar, G. Hasan Najafi, V. Swamy, Effects of dispersed multiwalled carbon nanotubes on the micro-explosion and combustion characteristics of 2-methylfuran – diesel mixture droplets, Fuel 316 (2022). https://doi.org/10.1016/j.fuel.2022.123308.

[11] R.L. Krupakaran, G.J. Rani, P. Anchupogu, G.V. Reddy, D.R. Reddy, R.K. Petla, Comparative assessment of MWCNTs and alumina nanoparticles dispersion in biodiesel blend on the engine characteristics of an unmodified DI diesel engine, Materials Today: Proceedings 68 (2022) 1241–1251. https://doi.org/10.1016/j.matpr.2022.06.045.

[12] S. Ramalingam, M. Naresh Babu, Y. Devarajan, M. Dinesh Babu, E.G. Varuvel, Environmental and energy valuation of waste-derived Cymbopogon Martinii Methyl Ester combined with multi-walled carbon (MWCNTs) additives in hydrogen-enriched dual fuel engine, International Journal of Hydrogen Energy 48 (2023) 39641–39657. https://doi.org/10.1016/j.ijhydene.2023.08.006.

[13] T. Sathish, K. Muthukumar, A.K. Abdulwahab, M. Rajasimman, R. Saravanan, K. Balasankar, Enhanced waste cooking oil biodiesel with Al2O3 and MWCNT for CI engines, Fuel 333 (2023). https://doi.org/10.1016/j.fuel.2022.126429.

[14] E. Geacai, I. Nita, S. Osman, O. Iulian, EFFECT OF n-BUTANOL ADDITION ON DENSITY AND VISCOSITY OF BIODIESEL, U.P.B. Sci. Bull., Series B 79 (2017). https://www.scientificbulletin.upb.ro/rev_docs_arhiva/full638_310332.pdf.

[15] A. Rahman, D. Kumara, W. Kusdiana, A. Nugroho, THE UTILIZATION OF FUEL DIESEL EMULSION AS A RESERVE SOURCE OF DIESEL FUEL FOR INDONESIAN WAR SHIPS, International Journal of ASRO 11 (2020) 44–53. https://doi.org/10.37875/asro.v11i04.357.

[16] KERN & Sohn GmbH, Operating instructions Analytical balance KERN ADB_ADJ, (2019). https://dok.kern-sohn.com/manuals/files/English/adb_adj-ba-e-1931.pdf.
[17] Romanian Standards Association, SR EN 590:2022 Automotive fuels. Diesel fuel. Requirements and test methods (2022).
[18] P. Chipurici. Determination of the Density of Petroleum Products. Laboratory report, National University of Science and Technology Politehnica Bucharest, Faculty of Chemical Engineering and Biotechnologies, Department of Bioresources and Polymer Science.
[19] J.I. Urete, M.O. Sule, J. Gordon, O.S. Kolade, R. Nze, S.A. Tsebam, O.B. Oyeleye, D.U. Robinson, I.A. Fetuga, Biodiesel Production Optimization from Waste Cooking Oil Using Animal Bone Catalyst, The Journal of Engineering and Exact Sciences 9 (2023). https://doi.org/10.18540/jcecvl9iss8pp16634-01e.
[20] P. Chipurici. Determination of the Viscosity of Petroleum Products. Laboratory report, National University of Science and Technology Politehnica Bucharest, Faculty of Chemical Engineering and Biotechnologies, Department of Bioresources and Polymer Science.
[21] M.O. Abdul-Majeed, Effect of Diarrheastat® and Enrosol-S® on rumen ecosystem in rams Diarrheastat® Enrosol-S®, Iraqi Journal of Veterinary Sciences 25 (2011) 29–33. https://doi.org/10.33899/ijvs.2011.5703.
[22] A.C. Sajeevan, V. Sajith, Synthesis of stable cerium zirconium oxide nanoparticle - Diesel suspension and investigation of its effects on diesel properties and smoke, Fuel 183 (2016) 155–163. https://doi.org/10.1016/j.fuel.2016.06.048.
[23] BSI Standards Publication, BS ISO 22412:2017 Particle size analysis — Dynamic light scattering (DLS) (2017).
[24] Malvern Instruments, Inc, Dynamic Light Scattering: An Introduction in 30 Minutes, Technical note. https://www.research.colostate.edu/wp-content/uploads/2018/11/dls-30min-explanation.pdf.
[25] M.A. Fahim, T.A. Alsahhaf, A. Elkilani, Thermophysical Properties of Petroleum Fractions and Crude Oils, in: Fundamentals of Petroleum Refining, Elsevier, 2010: pp. 33–67. https://doi.org/10.1016/B978-0-444-52785-1.00003-6.
[26] A. Krüss Optronic GmbH, Refractometers. https://www.ankersmid.com/AutoFiles/doc/5909_Refraktometer%20totaal.pdf.
[27] Beckman Coulter, Inc., Coulter N4 Plus Preliminary Manual.
[28] D. Gamboa, B. Herrera, J. Acevedo, D. López, K. Cacua, Experimental evaluation of a diesel engine using amide-functionalized carbon nanotubes as additives in commercial diesel and palm-oil biodiesel, International Journal of Thermofluids 22 (2024). https://doi.org/10.1016/j.ijft.2024.100669.

CONSIDERATIONS FOR MODELING, CALCULATION AND AUTOMATION OF A FIRE SUPPRESSION INSTALLATION IN AN INDUSTRIAL FACILITY

Cosmin GURAN [1*], Adina GAVRILA [1], Oana PARVULESCU [1], Timur CHIS [2], Tanase DOBRE [1]

[1]National University of Science and Technology Politehnica Bucharest, Polizu 1-7, 01161, Bucharest Romania; [2]Petroleum and Gas University of Ploiesti, B[dul] Bucharest 39, Ploiesti, Romania

Abstract

The main purpose of the work is to show how it optimizes fire detection, signaling and extinguishing systems for various installations, so as to minimize the risk of all loss types. Considering all the provisions of current regulations, the paper presents a case study regarding the organization of the fire extinguishing installation in an industrial location such as a chemical materials warehouse.

Key words: Industrial warehouse, Suppression fire installation, Computing model, Case study

1. Introduction

In this paper, water is used as a fire extinguishing agent for the specific case considered. Water is the most commonly used fire extinguishing agent, mainly due to the fact that it is widely available and inexpensive. It also has very desirable fire extinguishing characteristics such as a high specific heat and high latent heat of vaporization. A single kilo of water can absorb 5819.5 kJ of heat as it increases from 21^0C room temperature to become steam at 100 ^{0}C. Water is not the perfect extinguishing agent [1-4], however, and is considered inappropriate for the protection of certain water reactive materials. In some cases, the use of water can produce heat, flammable or toxic gases, or explosions. The quantities of such products must be considered, however, because application of sufficient water can overcome the reaction of minor amounts of these materials. With or without water as fire extinguishing agent, the fire protection is important for several essential reasons, concerning both human safety and protection of property and environment. It is mentioned in this regard: i) Human life protection, ii) Limitation of material damage, iii) Business continuity, iv) Environmental protection, v) Legal compliance and respectively vi) Protection of heritage and community.

∗ Corresponding author: Email address: cosmin.guran@yahoo.com

2. Modelling considerations for fire extinguishing installation (FEI)

In the algorithm for modeling an extinguishing installation, the first step consists in setting the capacity conditions of the enclosure that must be ensured. This is followed by checking each of the requirements imposed by the preventive, passive and active protection methods**.** As preventive measures (prevent fire outbreak) it is obliged to consider and justify: i) Safe electrical installations (periodic checks, overload/short circuit protection), ii) Proper storage of flammable materials (in ventilated spaces, special containers), iii) Smoking prohibition in hazardous areas, iv) Equipment maintenance (prevention of sparks, fuel leaks), v) Personnel training on fire safety rules and respectively vi) Prevention plans and internal procedures (including ISU controls). For passive protection measures, which take into account the limit of fire spread, it must by justified: i) Building compartmentalization with or whiteout fire-resistant walls and doors, ii) Fire-resistant cables, pipes and materials, iii) Smoke and hot gas evacuation systems, iv) Luminous evacuation markings and emergency lighting and not on the last place v) Access for fire trucks and external hydrants. Active protection measures oriented to detect and combat the fire refers to: i) Detection and alarm systems containing smoke, temperature, flame detectors, manual buttons and opto- acoustic sirens, ii) Automatic suppression installations based on sprinklers, deluge systems, foam, water spray, inert or chemical gases, iii) Interior and exterior hydrants, iv) Portable extinguishers (appropriate to risk type: water, foam, powder, CO_2) and respectively v) Alarm transmission systems to firefighters/dispatch. In the sense of the above-mentioned requirements, organizational methods must be added and clearly implemented, which must contain: i) Clear evacuation plan, displayed and practiced periodically, ii) Fire drills (practical exercises with personnel), iii) Trained internal intervention teams (PSI brigade) and iv) Control and maintenance register for safety equipment.

a. Case Study of FEI modeling, calculation and automation

Construction characteristics analysis

First of all, for the minimum mandatory equipment and fitting of buildings and installations with fire suppression systems and installations, the requirements from Romanian standards, norms and laws. Concretely for building must be respected, referring to such buildings, especially normative P118/2-2013 with subsequent additions. The fire limitation and suppression installations that will equip the investment objective are:

- Fire suppression installations with interior fire hydrants
- Fire suppression installations with exterior fire hydrants

- Automatic fire suppression installations type sprinkler

For our exemplification, we consider as a case study an industrial production and storage hall for dangerous materials and substances, with the technical characteristics given by table 1.

Table 1.

Technical specifications of the building

Ac	uilding height	Volume	Resist. grade	Stored goods	Storage height	Q_{hi}	Q_{he}	Material category	Q suppres	As
[m^2]	[m]	[m^3]	-	-	[m]	[l/s]	[l/s]	[-]	[l/min]	[m^2]
2610	8.00	20880	II	chemical materials	6	4.2	15	III	30	300

The height regime is 8 m and the maximum storage height in racks is 6m. Built area known as developed area have the value of 2610 m² and it must be insured against fire danger The corresponding volume of the warehouse chemical products water resistant is 20880 m^3.

Norms and regulations

The work was elaborated in accordance with the following provisions in force, specified here at references list [5 -10]

After norms and regulations the technical equipment of buildings with different types of cold water supply installations for fire fighting is done according to: i) Building destination (residential, social-cultural, industrial etc.), ii) Building size (built volume and number of floors), iii) Number of persons active in the building, iv) Fire resistance grade and fire hazard category of the building, v) Importance of the building or of goods and materials sheltered in buildings and vi) Other technical or economic factors

Exterior and interior hydrants

In the calculation model, the establishment of the number of hydrants to be placed inside and outside the chemical warehouse is done in accordance with the norms imposed by law.

According to normative P 118-2/2013 [8], containing specifications regarding fire safety of buildings, we find in Part II - Suppression installations the art. 6.1. paragraph n which stipulates production and/or storage buildings with high or very high fire risk, with developed areas greater than 600 sqm and volume over 3000 m^3 mandatory equipment with exterior fire hydrants is required. Since the conditions specified above are met, regarding fire risk, the building being classified in category C fire hazard (high fire risk) Ac = 2610 sqm, V = 20880 mc, mandatory equipment of the investment with exterior fire hydrants is required. For interior hydrants the normative P 118-2/2013 [8] we find art. 4.1. paragraph l, which shows that production and/or storage buildings or spaces where combustible materials or substances are used, with developed area greater than 600 m^2, mandatory equipment with interior fire hydrants is required. As a result, the investment objective will be equipped with interior fire hydrants.

Following the specifications referring to exterior fire hydrants, the investment objective that is the subject of this project will be equipped with minimum three exterior fire hydrants. The number of jets in operation is: 1 jet in operation, the water flow rate that must be ensured for production and storage buildings with volume less than 50000 mc and fire stability level II, according to annex no. 8 from P118/2- 2013 is: 15.0 l/s for buildings equipped with sprinkler suppression installations. Table 2 shows this selection

Table 2.

Flow rate for external hydrants according to Annex 8 reference [8]

Buikding fire stability	Fire risc	Water flow rate for extinguishing a fire qie (l/s) reported to building volume mc)							
		până la 2000	2001 ... 3000	3001 ... 5000	5001 ... 20000	20001 ... 50000	50001 ... 200000	200001 ... 400000	peste 400001
I – II	small	5	5	5	10	10	10	20 (15)	20 (15)
	high	5*	10	10	15	20 (15)	30 (20)	35 (20)	40 (30)
III	smal	5	5	10	15 (10)	20 (15)	30 (15)	-	-
		5	10	15 (10)	20 (15)	30 (20)	40 (20)	-	-
IV - V	small	5	10	15 (10)	20 (15)	20 (15)	-	-	-
	medium	5	15	20 (15)	25 (20)	40 (30)	-	-	-

For hydrodynamic computation of water flow rate respect to the exterior fire hydrant installation will have the following characteristics:

- theoretical operating time for exterior hydrants, according to art. 6.19 [8] is 180 minutes
- calculation flow rate of the installation, according to annex no. 8 from P 118-2/2013 [8] is: 15 l/s

It obtains the intangible water reserve for fire suppression with exterior hydrants V_{he} =15 x 180 x 60 = 216000 liters = 162 m^3

For exterior suppression of a possible fire, the investment objective will be equipped with four exterior fire hydrants, above-ground, with diameter D_n = 100 mm, with two type B couplings and one type A coupling, which can each ensure a flow rate 3 pcs x 5.0 l/s = 15 l/s, so the total established flow rate. The four above-ground exterior fire hydrants will be placed, according to the plan here given by figure 1, in the beneficiary's premises, at approximately 5.5 m from the building. Water supply to exterior hydrants will be realized with a high-density polyethylene pipe type PEHD, with diameter DN 150 mm.

We consider that the public street network cannot ensure exterior suppression of a possible fire directly from exterior hydrants, but only through motor pumps or fire trucks. In this case for the investment, that is the subject of this case study, the establishing of the pump discharge pressure must be calculated. In indirect expression, as the water column pressure (H_{nec}), this results from the summation of the static column pressure (H_g) of the column pressure corresponding to the dynamics flow in pipes ($\Sigma i*l$) as well as the column pressure to overcome the hydraulic resistances in the transport path ($\Sigma h_r l$). According to the calculation summary from table 3 the result is $H_{nec} = H_g + \Sigma i*l + \Sigma h_r l + H_i = 12 + 6.577 + 20.81 = 29.38$ mH_2O

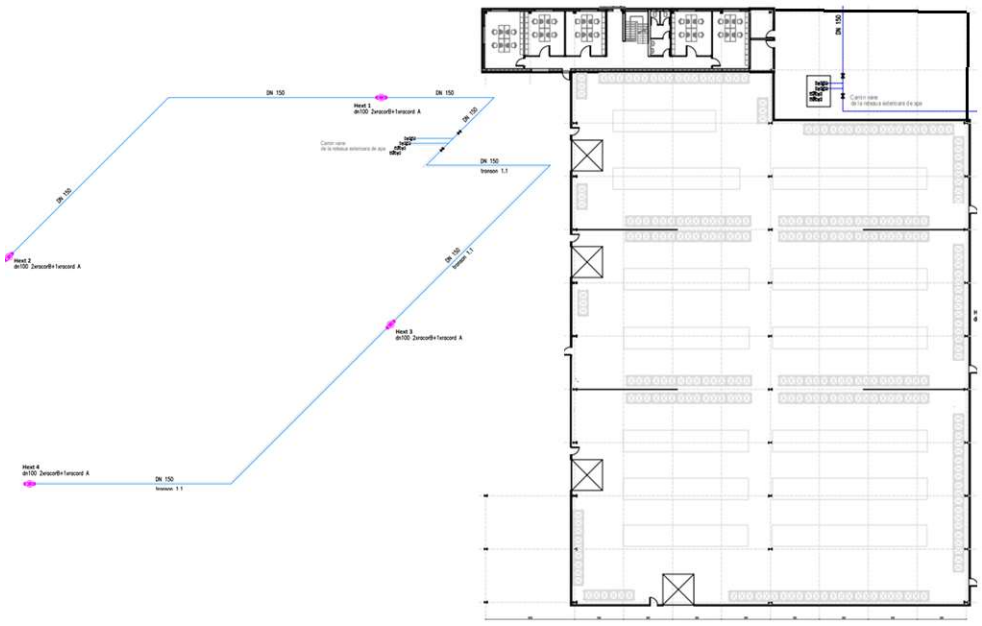

Fig. 1. Positioning of exterior hydrants connections in the warehouse and their external isometry

According to art. 6.8 from normative P 118-2/2013 [8], water inputs made with the help of exterior fire hydrants must reach all points of protected buildings (objectives) It is important to consider the action radius of operating hydrants with hose length, which can be 150 m in case of using motor pumps and 200 m in case of using fire trucks.

Table 3.

Data in computation of dischare pressure of motor pump for exterior hydrants

	q_c	l	d_n	v	i	$i*l$	$\Sigma i*l$	$\Sigma\zeta$	h_{rl}	Σ	H_g	H_i
	[l/s]	[m]	[mm]	[m/s]	[Pa/m]	[Pa]	[Pa]	[-]	[mH_2O]	[mH_2O]	[mH_2O]	[mH_2O]
ajutaj	5		18									
furtun	5	120	100	1.11	200	2.4	2.4	0	0	2.4		
T1.1	15	129	150	1.9	280	3.61	6.01	15.4	0.565	**6.577**	**12**	**20.81**

For the exterior hydrants, corresponding to the provisions of normative P 118-2/2013 [8], it establish that he interior installation will have the following characteristics: i) minimum specific flow rate of one jet q_{hi} = 2.10 l/s, after data given in annex no. 3 from [8], ii) number of jets in simultaneous operation per building n = 2 one for production and on for storage buildings (case of warehouse with volume greater than 5000 mc in before mentioned annex) , iii) effective reach of a jet must ensure the following minimum lengths as follow 10 meters for compact jet, 6 meters for spray jet in curtain form, 3 meters for conical spray jet, iv) flow rate for fire suppression with interior hydrants Q_{hi} = n q_{hi} = 2 x 2.10 = 4.20 l/s, v) standard operating time of interior hydrants T_{hi} = 10 minutes as it is recommended, for this

warehouse, in art. 4.35 from [8], vi) intangible water reserve for fire suppression with interior hydrants: $V_{hi} = 60(n-1)q_{hi}T_{hi} = 60 \times 1 \times 2.1 \times 10 = 1260$ liters, so 1.30 m^3 vii) available pressure necessary at interior hydrant coupling is 33.05 mCA as it result from data given in table 4

Table 4.

Data in computation of pressure at the coupling of interior hydrants

Tronson	q_c	l	d_e	v	$\Sigma i*l$	$\Sigma\zeta$	Σh_{rl}	Σ	H_g	H_i	H_{nec}
	[l/s]	[m]	[mm]	[m/s]	[mH2O]	[-]	[mH2O]	[mH2O]	[mH2O]	[mH2O]	[mH2O]
ajutaj	2.1		13								
furtun	2.1	20	52	0.98	1.5	0	0	1.500			
T1.1	2.1	3.5	60.3	1	1.6225	2.80	0.134	1.757			
T1.2	4.2	14.1	76.1	1.2	2.1019	1.50	0.236	2.338			
T1.3	4.2	14.3	76.1	1.2	2.5881	6.80	0.696	3.284			
T1.4	4.2	9.2	76.1	1.2	2.9009	0.50	0.730	3.631			
T1.5	4.2	4.1	76.1	1.2	3.0403	1.50	0.832	3.872			
T1.6	4.2	21	76.1	1.2	3.7543	18.40	2.078	5.832	**4.8**	**22.41**	**33.05**

The interior hydrants proposed to be installed in the warehouse and office area no. 1 will be according to STAS 297/2 and ISO 6309, equipped with flat hose with diameter 50 mm and length 20 m. The universal discharge pipe provided with shut-off valve and with nozzle diameter of 12 mm will ensure the specific flow rate of 2.10 l/s. The distribution network for feeding interior fire hydrants will be executed from steel pipe because art. 4.26 from [8] shows that pipes made of plastic materials are not allowed for warehouse interior. Interior hydrants will be placed in accordance with the requirements [8, 10] in visible and easily accessible places in case of fire. Figure 2 completes Figure 1 by adding the positioning of the 6 interior hydrants in the warehouse, serving the sprinkler extinguishing system.

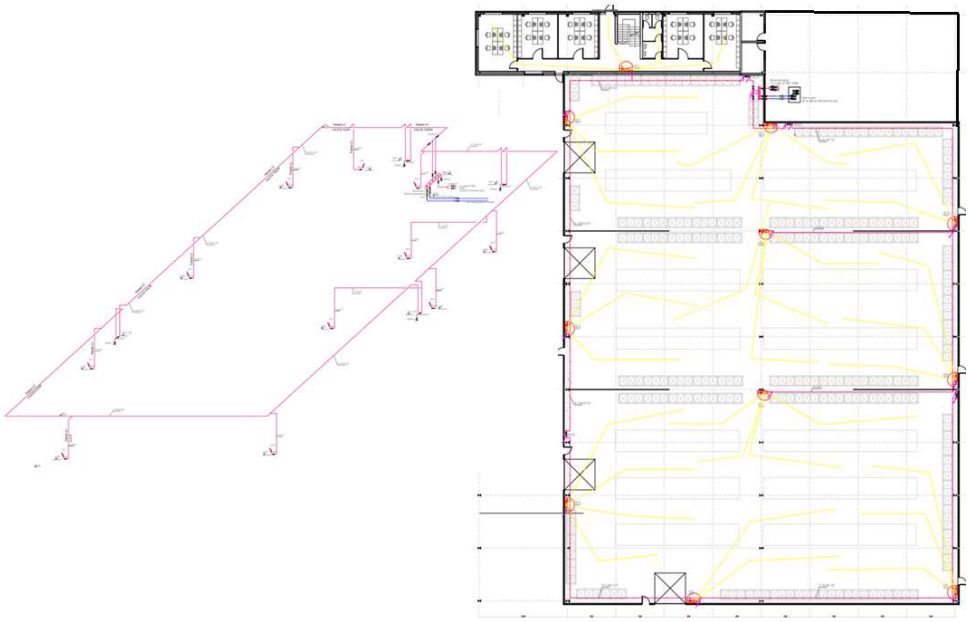

Fig. 2. Positioning of interior hydrants in the warehouse and their external isometry

2.2. Fire suppression installation with sprinklers

The warehouse spaces within the investment objective will be equipped with automatic sprinkler suppression installation. After provisions of normative P 118-2/2013 [8], for buildings classified in category C for fire hazard (high fire risk) having thermal load density less than 840 MJ/m^2, the sprinkler type fire suppression installation will have the following characteristics: i) fire risk class HHS 3 - warehouses with high hazard category III as it results from art. 7.4 paragraph 9 d from[8], ii) installation type: water-water, iii) required density per sprinkler head computed according to table 7.11 from [8] as it shown by table 5, iv) activation time 90 min established by recommendation from [8], v) sprinkler positioning at 9.0 meter height for assuring maximum area covered per sprinkler (table 7,4 from [8]), vi) required pressure at sprinkler head is established to 1.0 bar, vii) sprinkler type for HHS risk class is sprinkler with upward head having nominal factor K 160, viii) sprinkler installations in water-water system must be installed only if an ambient temperature of minimum 4 degrees C is ensured.

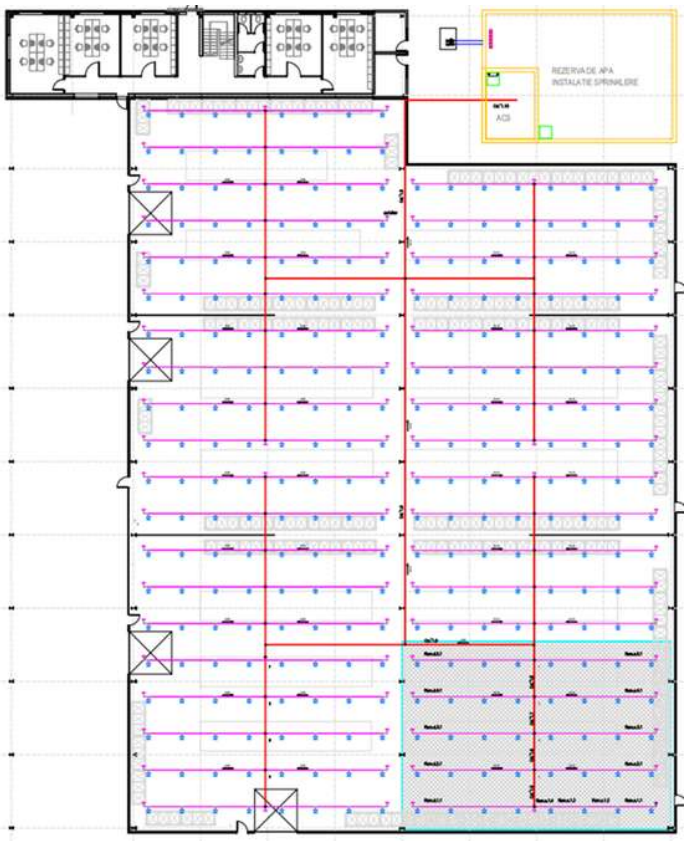

Fig. 3. Sprinklers Positioning and water supplying in the warehouse

To those above given for sprinklers installation we add the below calculation notes for sprinklers exploitation:

- number of sprinkler heads in simultaneous operation $N=N_T/9 = 300/9.0 = 33.3$, so 40 is a good selection,
- flow rate of one sprinkler head $q = K \times P^{1/2} = 80 \times 1^{1/2} = 274.4$ l/min, rounded to 275 l/min
- flow water density due to suppression from table 5 $I_{suppr} = 30/60 = 0.5$ l/(m^{2}s)
- Spraying density $I_{spray} = q/Ac = 275/(60\ 9.6) = 0.52$ l/(m2s), which is over I_{suppr}, as it is recommended [9]
- sprinkler installation flow rate $Q = N \times q = 40 \times 275 = 11\ 000$ l/min = 184 l/s,
- intangible water reserve $V_{sprinklers} = Q * T * 60\ \ 10^{-3} = 993 m^3$

Table 5.

Establishing of sprinkler spraying density according Table 7.11 of [8]

Storage method	Maximum loading height in the warehouse				Spraying density		Protected area when simultaneously triggering sprinklers
	Category I	Category II	Category III	Category IV	l/m/min	l/sm^2	
ST1	5,3 6,5 7,6	4,1 5,0 5,9 6,7 7,5	2,9 3,5 4,1 4,7 5,2	1,6 2,0 2,3 2,7 3,0	7,5 10,0 12,5 15,0 17,5	0,125 0,166 0,208 0,25 0,292	260
			5,7 6,3 6,7 7,2	3,3 3,6 3,8 4,1 4,4	20,0 22,5 25,0 27,5 30,0	0,333 0,375 0,416 0,458 0,5	300
ST2 ST4	4,7 5,7 6,8	3,4 4,2 5,0 5,6 6,0	2,2 2,6 3,2 3,7 4,1	1,6 2,0 2,3 2,7 3,0	7,5 10,0 12,5 15,0 17,5	0,125 0,166 0,208 0,25 0,292	260
			4,4 5,3 6,0	3,3 3,8 4,4	20,0 25,0 30,0	0,333 0,416 0,5	300
ST3 ST5 ST6	4,7 5,7	3,4 4,2 5,0	2,2 2,6 3,2	1,6 2,0 2,3 2,7 3,0	7,5 10,0 12,5 15,0 17,5	0,125 0,166 0,208 0,25 0,292	260

2.3 Automation of the sprinkler extinguishing system

Automatic system for fire extinguishing with sprinklers comprises a network of water pipes, above described, and sprinklers with sensible head, distributed throughout a building (figure 3). The sprinkler heads include heat-sensitive glass phials which expand and shatter when they detect an increase in air temperature. The individual sprinkler activation trigger an alarm and initiate firefighting efforts with/without human intervention. This selective and immediate response protects life and property more effectively by limiting fire growth and reducing damage, and

it can also allow for greater architectural freedom by reducing the need for fire-resistant compartmentation.

3. Conclusions

From past experiences we have found that any building and especially big warehouses can be subject to fire risk, and the best method to save lives, but also to minimize damage caused by a possible fire is the taking prevention measures.
The dimensioning of the suppression installation above represents the optimal system model that reduces to a minimum the possible losses caused by an eventual fire. In dimensioning was applied a computation model which respect all the rules set by the legislation in force [5-11]. Fire detection and suppression systems operate continuously, ensuring permanent monitoring of the protected area. This means they are activated and ready to respond to any sign of fire at any time of day or night, even when there are no people nearby. The advantages offered by automation system are characterized by early fire detection, 24/7 protection, rapid response and immediate intervention, automatic objective protection, reduction of material damage, personal safety and lifesaving. Fire detection and suppression systems are designed to respond independently, with or without requiring human intervention. It is recommended that even in the absence of a person, the system can detect and extinguish the fire, providing protection.

REFERENCES

[1] Stefan Sardqvist, *Water and other extinguishing agents*, Swedish Rescue Services Agency, Stockholm, 2002
[2] Fogarty T., Hansen C. T., *Fire fighting water runoff management for fire safety professionals in the United Kingdom: Effective warehouse and industrial site mitigation and response strategies for Fire Risk Assessment,* University of Applied Research & Development, 2002
[3] Daniel Della-Giustina, *Fire safety management handbook*, 3th Edition, CRC Press,2014
[4] Liu Z, Kim Ak., *A review of water mist fire suppression systems – Fundamental studies*, J. Fire Prot. Eng., 10, 32–50, 1999
[5] Law no. 10/1995 *Regarding quality in construction*, modified by Law no. 163/2016
[6] I9/2015 – *Normative for design and execution of sanitary installations*
[7] STAS 1478/90 – *Sanitary installations. Water supply for civil and industrial buildings*. Fundamental prescriptions
[8] P118-2/2013 – *Normative regarding fire safety of buildings*, with subsequent modifications and additions
[9] SR EN 12845/2015 - *Fixed fire fighting installations. Automatic sprinkler systems*. Design, installation and maintenance
[10] General *Norms for Fire Protection*, approved by MAI order no.163/28.02.2007
[11] SR EN 671-2 2012. *Fixed fire fighting systems* – Hose systems

DYNAMIC ADSORPTION BEHAVIOR OF VOLATILE ORGANIC COMPOUNDS ON A REGENERATIVE CELLULOSE-SILICA GEL COMPOSITE – EXPERIMENTAL INVESTIGATION AND MATHEMATICAL MODELLING

Ionuț-Alexandru POPA[1], Iuliana Mihaela DELEANU[1], Oana Cristina PARVULESCU[1], Timur-Vasile CHIȘ[2], Tănase DOBRE[1,3*]

[1]National University of Science and Technology Politehnica Bucharest, Polizu 1-7, 01161, Bucharest Romania, [2]Petroleum and Gas University of Ploiesti, 39 Bucharest B[ld], Ploiesti, Romania, [3]Technical Science Academy of Romania, 26 Dacia B[ld] Bucharest Romania

Abstract

Building of a breakthrough curve for the adsorption of one volatile organic compounds from air onto a cellulose-silica gel composite adsorbent and use of breakthrough curve to identify the external particle mass transfer coefficient and of interphase equilibrium repartition coefficient.

Key words: Volatile Organic Compounds,Adsorption Dynamics,Adsorption Experimental Investigation, Mathematical Modelling, Breakthrough Curves, Mass Transfer Coefficients

1. Introduction

Volatile organic compounds (VOC) constitute a wide class of organic chemicals with high vapor pressure and low water solubility, many of which are used as solvents or emitted as process-related fugitive emissions; they are important both as pollutants and as occupational hazards in manufacturing environments. Regulatory and health concerns regarding VOC have motivated extensive efforts to reduce emissions at source and to treat exhaust streams prior to release to the atmosphere [1]. The automotive industry is a major emitter of process-related VOC, principally from paint shops and solvent-based surface treatments where coatings, thinners and cleaning agents are widely used. Workplace exposure and factory-level emissions in vehicle manufacturing and repair have been repeatedly documented, highlighting the need for robust abatement and monitoring strategies in both production and maintenance facilities [2, 3]. Adsorption remains one of the most practical and widely applied technologies for VOC abatement due to its operational simplicity, energy efficiency (when coupled with regenerative desorption) and adaptability to a range of contaminants and concentrations. Recent interest has focused on hybrid and composite adsorbents that combine low-cost, sustainable matrices (such as cellulose) with high-surface-area inorganic phases (e.g., silica gel) to yield materials that are both effective and regenerable. Such cellulose–silica composites offer an attractive balance of mechanical stability, tunable porosity and potential for low-cost regeneration cycles [4 -6]. Beyond material development, rigorous

* Corresponding author: Tănase Dobre; Email address: tanase.dobre@upb.ro

quantification of adsorbent performance under realistic process conditions requires experimentally measured dynamic responses (e.g., breakthrough curves, desorption profiles) and a theoretical framework capable of capturing the coupled phenomena of external mass transfer, intraparticle diffusion and adsorption kinetics. Mathematical models — ranging from lumped kinetic descriptions (pseudo-first/second order) to mechanistic, diffusion-limited fixed-bed models — are essential for interpreting experimental data, scaling laboratory observations to pilot and industrial scales, and optimizing regeneration strategies. These models also permit estimation of key design parameters such as mass transfer coefficients and effective diffusivities, which directly determine adsorber size, cycle time and overall process economics [7, 8]. Given the heterogeneous nature of composite adsorbents and the complexity of VOC mixtures typical in automotive operations, an integrated experimental–modeling approach is therefore necessary. Experimental data validate and parametrize mechanistic models, while modeling provides predictive capability and insight into rate-limiting steps (e.g., film resistance versus pore diffusion) that guide material modification and process design. The present study adopts this coupled strategy to characterize the dynamic adsorption behavior of VOC on a regenerative cellulose–silica gel composite, extract mass-transfer parameters from breakthrough curve and develop and validate a mathematical model for these dynamics.

2. Experimental Investigation

The laboratory setup, improved over time in the mass transfer laboratory from UNSTPB, shown in Fig. 1, has consisted of two main sections, i.e. a gas-VOC vapor mixture preparation section and an adsorption-heating section. In the section of gas-VOC vapour mixture preparation, the carrier gas (atmospheric air) was introduced by a compressor (1) into a silica gel column (2), in order to remove the humidity, and then into the bubbler (3), wherein it was bubbled into the liquid VOC (pure IPA, HEX, MDC,etc). The air flow was controlled by a valve (4) and measured by a flow-meter (5). The adsorption-heating section has mainly consisted of the adsorption column (6), coil heater (7), fins heater (8), and fan (9) which were fitted in an enclosure with polystyrene isolating walls (10). The dried adsorbent was packed into the glass column (6), d_c=1.7 cm internal diameter and Hc=29 cm height, which was set into a plastic support (11) and put on a digital balance (12). The mixture of air and VOC vapor from the bubbler (3) was heated in the coil heater (7), was fed into the bottom of adsorption column (6) and up-flowed through the adsorbent fixed bed until the bed was saturated. Air temperature inside the isolating enclosure was raised and maintained at a constant value by the fins heater (8). The thermal agent in the coil and fins heaters was warm water fed by a centrifugal pump (13) from a thermostatic bath (14). The fan (9) intensified the thermal transfer between air and fins as well as provided a uniform distribution of temperature in the system. Air temperature inside the enclosure was measured by a digital thermometer (15). The amount of adsorbed VOC was estimated based on the increase of adsorption column mass, which was continuously measured by the digital balance (12) and registered by a computer (16). It was considered that the saturation state was achieved whenthe column mass did not vary in time for 10 minutes. The bubbler containing the liquid i VOC species was weighted before and after each adsorption experiment in order to determine the VOC

mass which was picked-up by the carrier gas, mi=mi0-mifin. A relative humidity sensor (17) was set at the column outlet in order to register the air relative humidity.

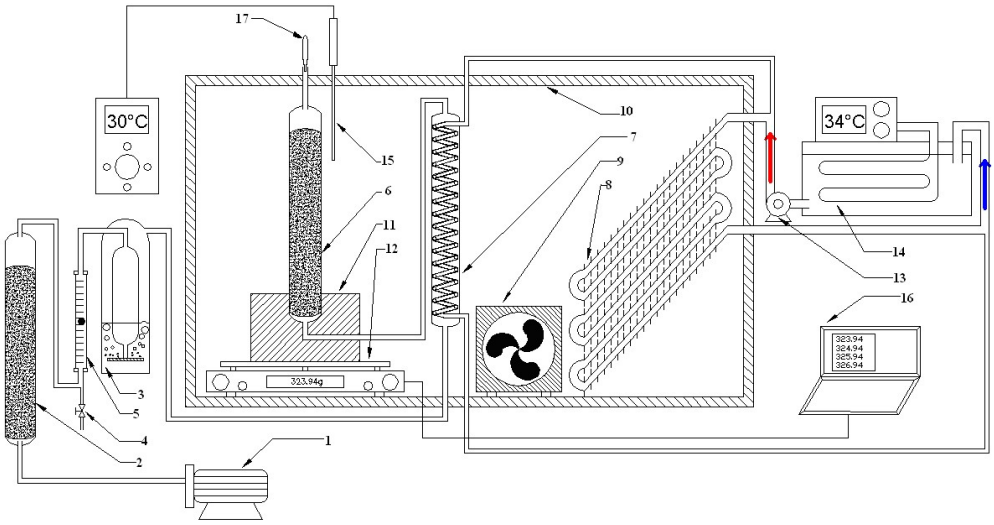

Fig. 1. Experimental setup: (1) compressor; (2) silica gel column; (3) bubbler; (4) valve; (5) flow-meter; (6) adsorption column; (7) coil heater; (8) fins heater; (9) fan; (10) polystyrene isolating layer; (11) plastic support; (12) digital balance; (13) centrifugal pump; (14) thermostatic bath; (15) digital thermometer; (16) computer; (17) relative humidity sensor.

The working procedure consists in the following steps: 1) put in the adsorption column no more than 15 g of cellulose-silica gel composite material; 2) verify the existence of dichloromethane in bubbler and establish the mass of system; 3) select the air flow rate and the working temperature;v 4) start the heating of balance incinte and wait the touching of selected temperature;5) start the online registration and put the adsorption column on the balance platane;6) start the air flow rate at the selected value and note all working parameters;7) give a way in computer for saving the fishier with balance mass dynamic; 8)Verify the keeping of working parameters and wait to obtain the complete saturation of the cellulose-silica gel composite material bed.

Use the registered mass balance dynamics in order to build the bed saturation curve, which give the dynamics of bed mean content in COV (q) versus time.

Materials: A total of 15 g of a cellulose–silica gel composite material, prepared in-house, was used as the stationary phase for column packing. Dichloromethane, CH_2Cl_2 99.8%, analytical grade (VWR Chemicals) was used as the mobile phase. All reagents and solvents were employed without further purification.

3. Experimental data processing

With registered experimental data it can builds the adsorbent saturation curve. It represents the time evolution of concentration of retained COV (q_i) in the fixed bed at time τ_i. At a given τ_i the value of q_i becomes from relation (1) where m_i is the bed registered mass and $\underline{m_0}$ is the bed mass at experiment beginning.

$$q_i = \frac{m_i - m_0}{m_0} \tag{1}$$

A Langmuir monolayer adsorption of VOC molecules onto the surface of cellulose-silica gel composite particles was taking into account in order to describe the chemisorption equilibrium. When the bed is saturates at a fixed working temperature (t) the VOC concentration in the adsorbent, named q_∞ (g/g), is in equilibrium with the VOC concentration from gaseous phase noted as, $c_\infty = c_0$ (g/l) where c_0 is the VOC concentration in gas that input in adsorption column. The values of c_∞ were calculated according to Eq. (2) where $m_{ev} = m_{0b} - m_{finb}$ (g) represents VOC mass picked-up by the carrier gas (the difference between mass of bubbler with COV at input and at finish of experiment) , $\tau_{fin} = \tau_{sat} + 200$ (s) is final operation time, and G_V (l/h) represent the gas volumetric flow rate (in the second part of relation (2) w is gas fictive velocity in m/s)

$$c_\infty = c_0 = \frac{3600\, m_{ev}}{G_V \tau_{fin}} = \frac{m_{0b} - m_{finb}}{w \tau_{fin} \dfrac{\pi d_c^{\,2}}{4}} \tag{2}$$

For adsorption experiments at the same temperature and different values of air flow rate in the column the set values (c_∞, q_∞) can be used in order to obtain values of parameters characterizing the Langmuir isotherm (Q, K_L). In this sense a linearized form of Langmuir isotherm is expressed by Eq. (3). Here Q, as maximum adsorption capacity of adsorbent, and K_L as Langmuir equilibrium constant was identified by use of experimental equilibrium concentrations. The values of Q and K_L, can be determined from the intercept and the slope of the straight line given by a plot of $1/q_\infty$versus $1/c_\infty$.

$$\frac{1}{q_{i\infty}} = \frac{1}{Q_i} + \frac{\rho_b}{\varepsilon_b c_{i\infty} Q_i K_{L,i}} \tag{3}$$

Characteristic saturation data of VOC species adsorption was summarized in table 1 and commentaries about the obtained results is in results and discussion section.

4. Mathematical model

The dynamics of VOC species adsorption from air stream onto fixed bed cellulose-silica gel composite material and M/BC is been predicted by a model including transport and mass balance of VOC species. This model has been based on the following simplifying assumptions: i) flow pattern of gas phase along the column is axially dispersed plug flow, ii) phases densities are invariant due to process operating at constant temperature, iii) pressure drop across the bed is negligible and radial dispersion go to perfect mixing for this direction, iv) the surface reaction of chemisorption is the process rate-limiting step, v) a monolayer adsorption of VOC molecules occurs onto the surface of adsorbent sites , according to the Langmuir model, vi) overall adsorption rate of species is equal to the difference between forward reaction (adsorption) rate, R_a, and backward reaction (desorption) rate, R_d, vii) R_a varies linearly with free surface site ratio, $1-q/Q$, and species concentration in gas phase, *i.e.*,$R_{ai} = k_a \varepsilon_b (1-q/Q) c$, where k_a (s^{-1}) is adsorption rate constant and Q (g/g) maximum adsorption capacity at monolayer level and viii) R_d varies

linearly with species adsorption capacity, i.e., $R_d = k_d \rho_b q$. With above conditions the characteristic mathematical model of fixed bed adsorption of COV species from gas phase, is described by the following system of equations and restrictions [9]:
1) conservation equation of *i* species in bulk gas phase in the fixed bed voids, where *x* (cm) is axial distanceand $D_l = (w d_V)/2$ (cm^2/s) represents axial dispersion coefficient [10], [11]:

$$\varepsilon_b \frac{\partial c}{\partial \tau} + w \frac{\partial c}{\partial x} - \varepsilon_b D_l \frac{\partial^2 c}{\partial x^2} + \rho_b \frac{\partial q}{\partial \tau} = 0 \tag{4}$$

2) overall adsorption rate equation of *i* species:

$$\rho_b \frac{\partial q}{\partial \tau} = k_a \varepsilon_b \left(1 - \frac{q}{Q}\right) c - k_d \rho_b q \tag{5}$$

3) relationship for estimation of mean adsorption capacity at time τ of COV species, where *H* is total height of fixed bed:

$$q_{mn}(\tau) = \frac{1}{H} \int_0^H q(x, \tau) dx \tag{6}$$

4) initial conditions (clean bed in start):

$$\begin{aligned} &\tau = 0 \qquad 0 < x \le H \qquad c = 0, \quad q = 0 \\ &\tau = 0 \qquad x = 0 \qquad c = c_0, \quad q = 0 \end{aligned} \tag{7}$$

5) boundary conditions:

$$\begin{aligned} &\tau > 0 \qquad x = 0 \qquad \frac{\partial c(0,\tau)}{\partial x} = \frac{w}{D_l}(c_0 - c_{0+}) \\ &\tau > 0 \qquad x = H \qquad \frac{\partial c(H,\tau)}{\partial x} = 0 \end{aligned} \tag{8}$$

The equations and restrictions system (4) - (8) can be numerically solved using an adequate finite difference method. Minimizing the root mean squared error, δ, described by Equation (9), where $q_{exp(j)}$ represents experimental adsorption capacity for COV species at dimensionless time $j = \tau/\Delta\tau$ and $q_{mn(j)}$ is the model computed adsorption capacity ($j = 0, 1, , M$), $\Delta\tau = \tau_{fin}/M$ (s) is time step, and *M* a positive integer showing the number of integration steep respect to time is used for identification of kinetic parameters k_a and k_d .

$$\delta(k_a, k_d) = \sqrt{\frac{\sum_{j=0}^{M} \left[q_{mn}(j) - q_{\exp}(j)\right]^2}{M+1}} \tag{9}$$

In concrete the capitalization of one dynamics of cellulose-silica gel composite material saturation with dichloromethane as VOC occurs according to specification as follows: a) import in Matchad the primary data file from the location where it is disposable (keep is initial codification in order to easy identify the obtained results); b) obtain by file help the number of red data, data reading frequency and after that it introduces in computation program the cellulose-silica gel composite material mass, working temperature, bed

height and volumetric flow rate; c) specify the cellulose-silica gel composite material particle radius, the column diameter and it estimates from data file the cellulose-silica gel composite material saturation concentration with VOC; d) computes the column spatial air velocity and particle bed axial dispersion coefficient; e) choose others data to be used into computation program (density of cellulose-silica gel composite material particle, particle fraction void, the initial mass and the final mass of liquid VOC in air bubbler, etc), f) compute the time for bed saturation and initial concentration of VOC in the air entering in adsorption column; g) it computes the mass of column without cellulose-silica gel composite material and then the total amount of retained VOC, the VOC saturation concentration of cellulose-silica gel composite material bed and the vector that gives the dynamics of the bed saturation with VOC; h) plot the curve showing the experimental dynamics of bed saturation respect to selected VOC ad selected adsorbent. Based on experimental plan from Table 1, we present, by Figure 2, for each of the 12 experiments, here described, the saturation dynamics of the modified silica gel adsorbent.

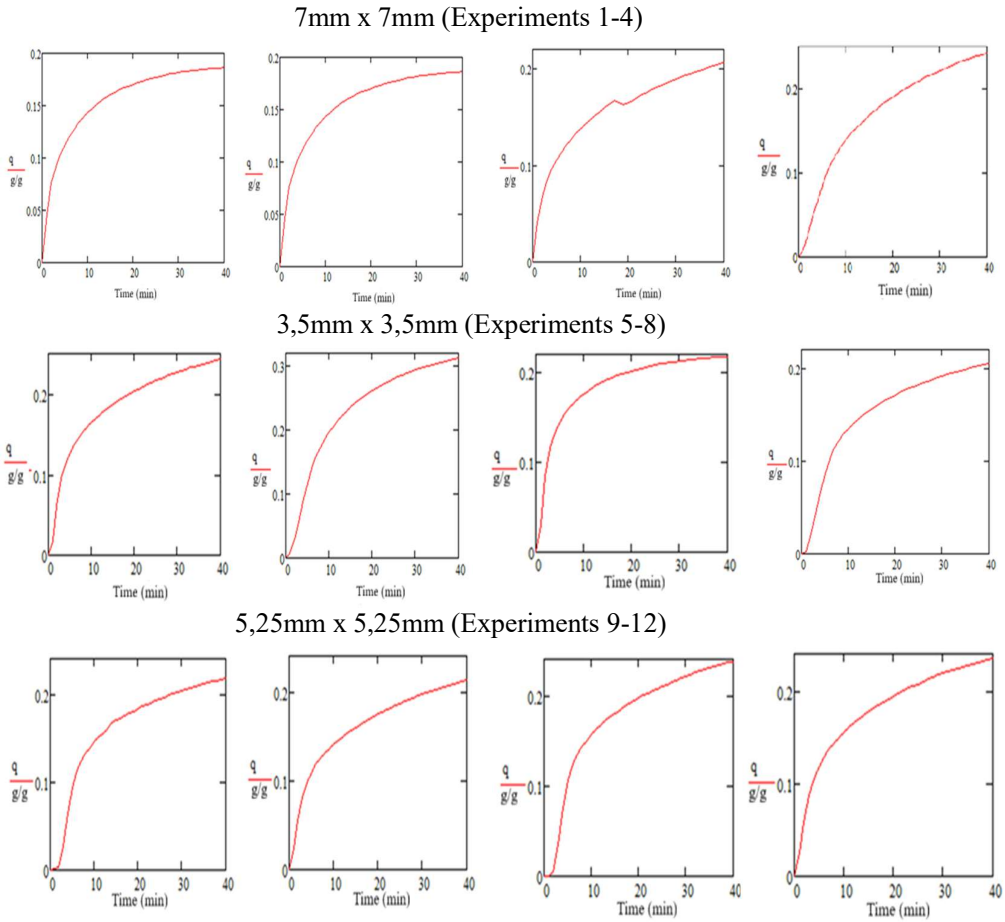

Fig. 2. Experimental dynamics of bed saturation for experiments described with table 1

Based on saturation bed dynamics it prepares to build of numerical integration by mean model function that gives the saturation curve dynamics; choose the number of integration steps along the bed height and the number of time steps and the increments

of space and time integration; enter the numerical function after k_a (k_{11} in the below) and k_d (k_{21} in the below) expressing the theoretical saturation curve of the adsorbent. Figure 3 shows the numerical integration sequence of the mathematical model in which the dynamics of the saturation of the adsorbent layer is expressed, as a function of the adsorption rate constant and the desorption rate.

$$
\begin{aligned}
&CS(k_{11},k_{21}) := \left|
\begin{array}{l}
Cc_{0,0} \leftarrow c_{00} \\
\text{for } i \in 1..N \\
\quad Cc_{i,0} \leftarrow 0 \\
\text{for } j \in 0..(M+1) \\
\quad Cc_{0,j} \leftarrow Cc_{0,0} \\
\text{for } k \in 0..N \\
\quad Sc_{k,0} \leftarrow 0 \\
\text{for } m \in 0..M \\
\quad \text{for } n \in 1..(N-1) \\
\quad\quad Sc_{n,m+1} \leftarrow \left|
\begin{array}{l}
0 \text{ if } \left[k_{11}\cdot\varepsilon\cdot\left(1-\frac{a_1\cdot Sc_{n,m}}{Q_L}\right)\cdot Cc_{n,m}-k_{21}\cdot\rho\cdot Sc_{n,m}\right]\cdot\frac{\Delta t}{\rho}+Sc_{n,m}\le 0 \\
Sc_{n,m} \text{ if } \left[k_{11}\cdot\varepsilon\cdot\left(1-\frac{a_1\cdot Sc_{n,m}}{Q_L}\right)\cdot Cc_{n,m}-k_{21}\cdot\rho\cdot Sc_{n,m}\right]\cdot\frac{\Delta t}{\rho}+Sc_{n,m}\le Sc_{n,m} \\
\left[k_{11}\cdot\varepsilon\cdot\left(1-\frac{a_1\cdot Sc_{n,m}}{Q_L}\right)\cdot Cc_{n,m}-k_{21}\cdot\rho\cdot Sc_{n,m}\right]\cdot\frac{\Delta t}{\rho}+Sc_{n,m} \text{ otherwise}
\end{array}
\right. \\
\quad\quad Cc_{n,m+1} \leftarrow \left|
\begin{array}{l}
Cc_{n,m} \text{ if } \left[-V_l\cdot\frac{Cc_{n+1,m}-Cc_{n,m}}{\Delta z}+D_L\cdot\frac{Cc_{n+1,m}+Cc_{n-1,m}-2\cdot Cc_{n,m}}{(\Delta z)^2}-\frac{(Sc_{n,m+1}-Sc_{n,m})\rho}{\Delta t}\right]\cdot\frac{\Delta t}{\varepsilon}+Cc_{n,m}\le Cc_{n,m} \\
Cc_{0,m} \text{ if } \left[-V_l\cdot\frac{Cc_{n+1,m}-Cc_{n,m}}{\Delta z}+D_L\cdot\frac{Cc_{n+1,m}+Cc_{n-1,m}-2\cdot Cc_{n,m}}{(\Delta z)^2}-\frac{(Sc_{n,m+1}-Sc_{n,m})\rho}{\Delta t}\right]\cdot\frac{\Delta t}{\varepsilon}+Cc_{n,m}\ge Cc_{0,m} \\
\left[-V_l\cdot\frac{Cc_{n+1,m}-Cc_{n,m}}{\Delta z}+D_L\cdot\frac{Cc_{n+1,m}+Cc_{n-1,m}-2\cdot Cc_{n,m}}{(\Delta z)^2}-\frac{(Sc_{n,m+1}-Sc_{n,m})\rho}{\Delta t}\right]\cdot\frac{\Delta t}{\varepsilon}+Cc_{n,m} \text{ otherwise}
\end{array}
\right. \\
\quad Cc_{N,m+1} \leftarrow Cc_{N-1,m+1} \\
\quad SMc_{m+1} \leftarrow \frac{1}{N}\left(\sum_{n=1}^{N} Sc_{n,m+1}\right) \\
(Cc, Sc, SMc) \\
CS \leftarrow SMc
\end{array}
\right.
\end{aligned}
$$

Fig. 3. Numerical integration sequence of the mathematical model of adsorption in a fixed bed from adsorbent particles

The final part of program for experimental data valorisation aims to identify, for each experiment, the adsorption and desorption rate constants. In this sense it establish: i) the function to be minimized after k_{11} and k_{21} in order to minimize the mean square deviation of the experimental and calculated values respect to saturation curve, ii) select the domain in which the k_{11} is searched and the domain in which k_{21} is searched and proceed to calculate the matrix containing the average square deviations (note that the calculation time is likely to be excessively high); iii) indentify inside of matrix the smallest values and from here the corresponding value of k_{11} and respectively k_{21}. With the indentified model parameters builds the matrix containing the computed dynamics of COV sorption on selected adsorbent. Select from this matrix the values of computed COV concentration

in adsorbent (q_c), which correspond with the measured material COV content(q) and shows on the same graphic the both time dependence (q_c vs. τ, respectively q vs.τ)

5. Results and discussions

Experimental investigations were carried out using cellulose–silica gel composite particles characterized by three distinct particle size ranges: large, small, and mixed distributions. The intermediate size fraction, corresponding to approximately half the mean diameter of the largest particles, was selected for detailed analysis to assess the influence of particle dimensions on column performance and mass transfer behavior. The experimental data considered for this particle fraction are summarized in Table 1, presenting the measured parameters and performance indicators relevant to the studied system. The results provide insight into the correlation between particle size, porosity, and solvent–solid interactions under the applied operating conditions.

Table 1.

Process and material parameters considered in the experimental investigation

NC	Particle Size (mm x mm)	Initial Mass of silica gel (g)	Final Mass of silica gel (g)	Initial Bubbler Mass (g)	Final Bubbler Mass (g)	CH_2Cl_2 Mass (g)	Temperature(°C)	Air Flow (L/h)	Column Layer Height (cm)
1	7 x 7	15	19,3	585.8	537.65	48.15	40	30	11.5
2	7 x 7	15	19	537.65	512.15	25.5	40	15	11.5
3	7 x 7	15	20.5	512.15	456.75	55.4	20	30	11.5
4	7 x 7	15	20.8	456.75	427.2	29.55	20	15	11.5
5	3.5 x 3.5	15	20.05	427.2	389.45	37.75	20	30	9.5
6	3.5 x 3.5	15	21.05	579.3	540.8	38.5	20	15	9.5
7	3.5 x 3.5	15	19.5	540.8	502	38.8	40	30	9.5
8	3.5 x 3.5	15	19.55	502.05	469.85	32.15	40	15	9.5
9	5.25 x 5.2	15	19.35	469.85	438.55	31.3	30	22.5	10.5
10	5.25 x 5.2	15	19.1	438.55	410.55	28	30	22.5	10.5
11	5.25 x 5.2	15	20,4	563.5	519.9	43.6	30	22.5	10.5
12	5.25 x 5.2	15	20	519.9	484.25	35.65	30	22.5	10.5
Values of q_∞ (g/g$_s$) and c_∞ (g/l) for experiments 1-9									
	1	2	3	4	5	6	7	8	9
q_∞	0.186	0.25	0.215	0.273	0.261	0.337	0.221	0.234	0.232
c_∞	0.95	1.69	0.589	1.382	0.623	1.044	0.762	1.086	0.938

In addition figure 4 illustrates a comparative visual representation of the cellulose–silica gel composite material for the two extreme particle size ranges. The structure differences are clearly observable, particularly in terms of surface morphology, texture uniformity, and degree of agglomeration. These morphological variations are consistent with the expected size-dependent behavior of the composite material, confirming the reproducibility and reliability of the synthesis and preparation procedure.

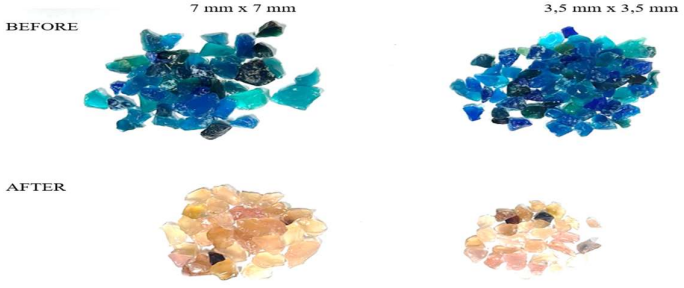

Fig. 4. Comparative visual representation of cellulose–silica gel composite particles showing differences in particle size and color before and after VOC removal.

Taken together, these findings establish a consistent experimental basis for the subsequent analysis and interpretation of mass transfer phenomena, which are further discussed in this section, with emphasis on the influence of process factors, including the particle morphology, on transport dynamics and COV sorption process efficiency.

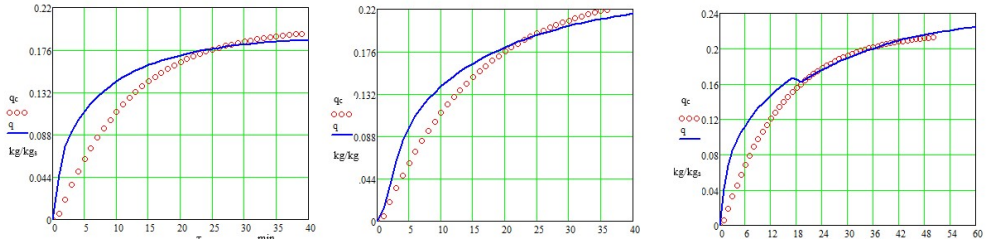

Fig. 5.Computed (red) and experimental (blue) dynamics of adsorbent bed saturation for experiments 1-3, table 1

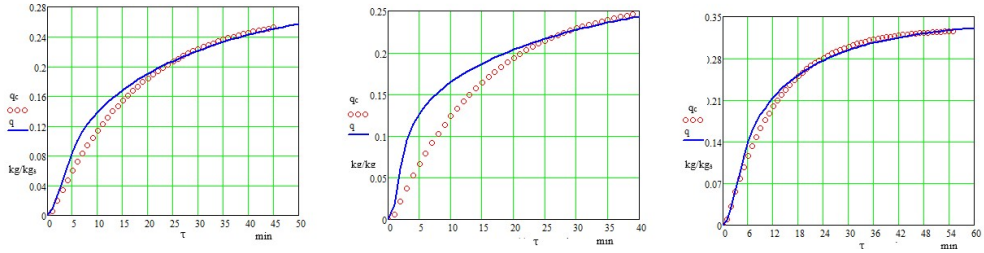

Fig. 6. Computed (red) and experimental (blue) dynamics of adsorbent bed saturation for experiments 4 - 6, table 1

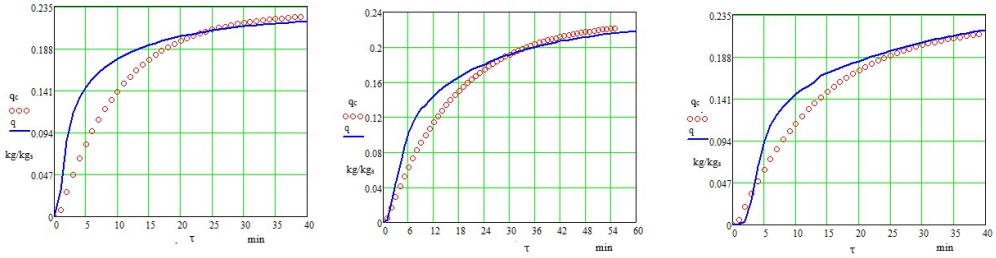

Fig. 7.Computed (red) and experimental (blue) dynamics of adsorbent bed saturation for experiments 7 - 9, table 1

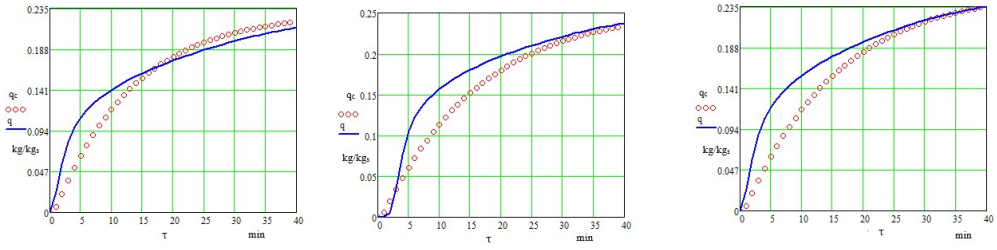

Fig. 8. Computed (red) and experimental (blue) dynamics of adsorbent bed saturation for experiments 10 - 12, table 1

Figure 5, Figure 6, Figure 7 and Figure 8, for which k_{11} and k_{21} are in table 2, illustrate the twelve breakthrough curves obtained from the numerical integration of the mass balance equations describing the adsorption process. Each curve corresponds to a distinct set of operating conditions, varying inlet concentration, flow rate, and adsorbent mass. The comparison between curves highlights the influence of external mass transfer resistance and adsorption kinetics on the overall process dynamics. The observed shapes and slopes of the curves indicate a system predominantly controlled. These results demonstrate a good agreement between the numerical model and the expected theoretical behavior. Consequently, the obtained profiles validate the suitability of the proposed mass transfer model for describing the studied adsorption process. A close agreement between the simulated and experimental breakthrough curves confirms the accuracy of the proposed theoretical model. The numerical predictions successfully reproduce both the breakthrough times and the curvature trends observed experimentally. Minor deviations at higher concentrations may be attributed to non-ideal flow effects or localized mass transfer limitations. Such consistency demonstrates that the assumptions regarding external film resistance and adsorption equilibrium are valid for the studied system. Therefore, the developed model can be confidently employed for process design, optimization, and scale-up of the adsorption unit.

Table 2.

Identified rate constants for sorption (k_{11}) and desorption (k_{21}) kinetics respect to experimental plan

N.C	Particle Size (mm x mm)	CH_2Cl_2 Mass (g)	Temperature, (°C)	Air Flow (L/h)	Bed Height (cm)	k_{11} s^{-1}	k_{21} s^{-1}
1	7 x 7	48,15	40	30	11,5	$3.85*10^{-4}$	$8.55*10^{-6}$
2	7 x 7	25,5	40	15	11,5	$2,15*10^{-4}$	$5.58*10^{-6}$
3	7 x 7	55,4	20	30	11,5	$5,95*10^{-4}$	$6.42*10^{-6}$
4	7 x 7	29,55	20	15	11,5	$2,45\ 10^{-4}$	$4.15\ 10^{-4}$
5	3,5 x 3,5	37,75	20	30	9,5	$6.32\ 10^{-4}$	$4.95\ 10^{-4}$
6	3,5 x 3,5	38,5	20	15	9,5	$5.53\ 10^{-4}$	$4.25\ 10^{-4}$
7	3,5 x 3,5	38,8	40	30	9,5	$6,55*10^{-4}$	$8.93*10^{-4}$
8	3,5 x 3,5	32,15	40	15	9,5	$2,75*10^{-4}$	$5.25*10^{-4}$
9	5,25 x 5,25	31,3	30	22,5	10,5	$3,85*10^{-4}$	$6.62*10^{-4}$
10	5,25 x 5,25	28	30	22,5	10,5	$3,85*10^{-4}$	$6.75*10^{-4}$
11	5,25 x 5,25	43,6	30	22,5	10,5	$4,15*10^{-4}$	$5.85*10^{-4}$
12	5,25 x 5,25	35,65	30	22,5	10,5	$4,05*10^{-4}$	$5.45*10^{-4}$

An analysis reported to Table 2 data regarding the state of VOCs reaction rate constant of adsorption and desorption on silica gel adsorbent shows that particle size, temperature and gas flow rate through the bed are important factors in their determination. If k_{11} and k_{21} were pure reaction constants then they should be influenced only by temperature. Their influence by gas flow rate and by particle size makes k_{11} and k_{21} as apparent reaction constants, which include the effect of COV outside particle mass transfer and particle inside COV diffusion. Table 3 notes the data organization as a matrix with 2 levels and 3 dimensionless factors (X_1-dimensional particle size, X_2-dimensional temperature and X_3 dimensionless gas flow rate) so as to highlight those influence on k_{11} and k_{21}.

Table 3.

Matrix of experimental design 2^3 with dimensionless particle size (X_1),dimensionless temperature (X_2) and respectively dimensikonless gas flow rate (X_3)

N	X_1	X_2	X_3	k_{11} s^{-1}	k_{21} s^{-1}
1	1	1	1	$3.85*10^{-4}$	$8.55*10^{-6}$
2	1	1	-1	$2,15*10^{-4}$	$5.58*10^{-6}$
3	1	-1	1	$5,95*10^{-4}$	$6.42*10^{-6}$
4	1	-1	-1	$2,45\ 10^{-4}$	$4.15\ 10^{-4}$
5	-1	1	1	$6.32\ 10^{-4}$	$4.95\ 10^{-4}$
6	-1	1	-1	$5.53\ 10^{-4}$	$4.25\ 10^{-4}$
7	-1	-1	1	$6,55*10^{-4}$	$8.93*10^{-4}$
8	-1	-1	-1	$2,75*10^{-4}$	$5.25*10^{-4}$
9	0	0	0	$3,85*10^{-4}$	$6.62*10^{-4}$
10	0	0	0	$3,85*10^{-4}$	$6.75*10^{-4}$
11	0	0	0	$4,15*10^{-4}$	$5.85*10^{-4}$
12	0	0	0	$4,05*10^{-4}$	$5.45*10^{-4}$

$$X_1 = \frac{d_p - 5.25}{1.725},\ X_2 = \frac{t - 30}{10},\ X_3 = \frac{G_{vg} - 22.5}{7.5} \quad (10)$$

Using of Table 3 data to obtain the dependencies $k_{11} = f(X_1,X_2,X3)$ and $k_{21} = g(X_1,X_2,X_3)$ [10] leads to the relations (11) and (12) respectively.

$$k_{11} = 4.45610^{-4} - 8.85310^{-5}X_1 + 1.12310^{-4}X_3 - 6.06310^{-5}X_1X_2 - 5.88510^{-5}X_2X_3 \quad (11)$$

$$k_{21} = 6.01610^{-4} + 1.20910^{-4}X_3 + 1.06610^{-4}X_1X_2 \quad (12)$$

If we refer to temperature, we find that k_{11} is high at low temperature, meaning that VOC adsorption is favored by low temperature. High temperature supports desorption, as is normal, meaning that k_{21} increases with temperature. It is also found that small particles favor VOC adsorption (negative coefficient in k_{11} for X_1). The high gas flow rate through the layer influences both VOC absorption and desorption.

6. Conclusions

The present study investigated the adsorption of volatile organic compounds (VOC) on a composite adsorbent based on cellulose and silica gel, focusing on the time dynamics of VOC concentration profiles under various operating conditions. A total of twelve experiments were conducted, varying flow rate, temperature, and adsorbent particle size, to evaluate both kinetic and equilibrium aspects of the process. The proposed theoretical model, developed from the mass balance and transport equations, accurately predicted the experimental breakthrough behavior across all tested conditions. A strong correlation between model predictions and experimental data confirmed the model's reliability, with minor deviations attributed to diffusion and non-ideal flow effects. The analysis highlighted that particle size and flow rate significantly influence mass transfer

efficiency and adsorption capacity. The model parameters demonstrated physical consistency and reproducibility, supporting their applicability in process design. Overall, the cellulose–silica gel composite exhibited high adsorption performance and stability. The validated model can thus serve as a predictive tool for optimizing adsorption systems for VOC removal and for scaling up to industrial applications.

REFERENCES

[1] U.S. Environmental Protection Agency. *What are volatile organic compounds (VOCs)?* EPA Indoor Air Quality (IAQ) — VOCs. (accessed Octomber2025)

[2] Song, M.-Y., et al. *Species and characteristics of volatile organic compounds from industrial and indoor sources.* Sci. Rep. 11, 2021

[3] Ghobakhloo S., et al., *Exposure to Volatile Organic Compounds in Paint Operations: Occupational Assessment and Health Implications.* Int. J. Environ. Res. Public Health 20, 2023

[4] Shi R.-J., et al. *Multifunctional Cellulose and Cellulose-Based (Nano)materials: Applications in Adsorption and Beyond.* Materials, 2022

[5] Song Q., et al. *Silica–bacterial cellulose composite aerogel fibers with enhanced mechanical properties and adsorption capacity.* (Journal), 2021

[6] Kutluay S., et al. *Silica gel based new adsorbent having enhanced VOC adsorption performance*. (Journal), 2021

[7] Vareda J. P., et al. *On validity, physical meaning, mechanism insights and pitfalls of adsorption kinetic models.* Chem. Eng. J., 2023

[8] Zheng J., et al. *Mass Transfer Kinetics of Volatile Organic Compound Desorption and Fixed-Bed Modeling.* Processes 12, 2024

[9] Linek F., Didovic F.M., *Representation of Breakthrough Curves for Fixed Bed Adsorbers or Reactors Using Moments of Impulse Response*, The Chemical Engineering Journal, 23, 31-36, 1982

[10] Dobre T., Sanchez J.M., Chemical Engineering Modelling Simulation and Similitude, Wiley VCH, 2007

[11] Dobre T., Pârvulescu O.C., Jacquemet A., Ion V.A., Adsorption and Thermal Desorption of Volatile Organic Compounds in a Fixed Bed – Experimental and Modeling, Chemical Engineering Communications (2016), 203, 12, 1554-1561

A NUMERICAL MODELS TO OIL WATER EMULSION

Aurelian ȘISINEA[1], Florin BOGDAN[1], Mihai ALBULESCU[2*]

[1]Ph.D. School, Petroleum-Gas University
[2]Oil and Gas Engineering Faculty, Petroleum-Gas University

Abstract

The growing thirst for energy from hydrocarbons leads to the use of all possibilities for the extraction, transport and storage of crude oil from Romanian deposits.That is why viscous crude oils are extracted to be processed in a mixture with freezable crude oils, in order to obtain refining products with a low processing cost.Viscous crude oils are also useful in the production of bitumen and that is precisely why their extraction is necessary. This paper analyzes the possibilities of transporting viscous crude oils in emulsion (both from the point of view of the stability of the emulsions and especially from the point of view of the rheological characteristics of transport). Even if emulsions can create problems in pipeline transport (by separating and decanting the water present in the emulsion), currently it is possible to create installations that do not lead to the deposition of water in the roughness of the pipes and therefore this transport is profitable and useful.

Key words: oil emulsion, pipeline, viscous.

1. Introduction

The viscous crude oils extracted in Romania are of type A3 (asphaltic-non-paraffinic-non-octane-oily).

That is why the extraction from the reservoir is difficult and the following recovery methods have been used:

a. emulsification of crude oils in the well by introducing polymer solutions,

b. extraction of crude oils by displacement with CO_2,

c. extraction using water-in-crude emulsions (water-in-oil).

In order to be processed in a superior way, these crude oils are extracted and transported in a selected manner.

But in order to be transported (these crude oils having high viscosity), the crude oils should be mixed with light crude oils (type B) or with fluid products with low viscosity (gasoline, diesel, diluent).

In practice, the chosen method of delivery for these types of crude oils is pumping as such (without being treated) [1].

That is why the pumping pressure is high (crude oils having a specific gravity above 0.9) and the viscosity is high (high pumping costs).

In this paper I tried to find a cheaper way to pump these types of crude oils by using emulsions as a means of treating them [2].

* Corresponding author: malbulescu@upg-ploiesti.ro

2. Materials and Methods

To observe the influence of water content on crude oil, an experiment was conducted in the laboratory consisting of emulsifying crude oils with various water ratios and measuring the viscosity of these mixtures.
For the study, crude oil samples were collected from the Roata and Ochiuri exploitation areas.
Also, imported Lirkuk type crude oil was used for comparison.
These crude oils were emulsified with reservoir water, network water and distilled water.

Table 1.

Types of crude oils used

Crude Oil	Sampling location	Crude oil type
Roata	Schela Bolintin	A3 selecționat
Ochiuri	Schela Pitești	C

In the first stage, the density of crude oils, distilled water, network water and reservoir water was analyzed.
The density was measured with an aerometer according to the ASTM D1298-12 b standard (Standard Test Method for Density, Relative Density, or API Gravity of Crude Petroleum and Liquid Petroleum Products by Hydrometer Method).
The crude oils were emulsified in proportions of 20, 40, 60, 80 % using a mixer.
Viscosity was determined using an Engler viscometer according to ASTM D 445-15- Standard Test Method for Kinematic Viscosity of Transparent and Opaque Liquids (and Calculation of Dynamic Viscosity).

Table 2.

Density and pH value

Liquid tipe	**Density, kg/dm^3**	**pH**
Ochiuri oil	0,894/22°C	-
Roata oil	0,899/22°C	-
Kirkuk oil	0,851/22°C	-
Salt water	1,0353/22°C	7,5
Distiled water	0,9754/22°C	7
Water production	0,9442/22°C	7

From the analysis of the above data, the following can be deduced:
a. Emulsification leads to a decrease in viscosity only when a ration of 80-20 and 40-60 water-crude oil is used,
b. The data from the specialized literature are confirmed, namely the transport of emulsified crude oil can only be done in an emulsion of the crude oil-in-water type,
c. It is also observed that distilled water ensures better emulsification compared to reservoir water,
d. The relationship used for the conversion from Engler degrees to cSt is [3]:

$$\nu = 7{,}31 \cdot E - 6.31/E \quad (1)$$

3. Results and discussions

The use of emulsions leads to a decrease in viscosity.
To observe the influence of emulsification on the pumping of crude oil, we simulated the pumping of Roata crude oil through the pipeline.

Table 3.

Engler viscosity values measured on various crude oil-water ratios

Blending	Emulsification rate, %	Flow time, s	Viscosity, grad E	Viscosity, cSt
Salt water/ Roata Oil	100-0	45,5	1,101	2,32
	80-20	80	1,93	10,90
	60-40	127	3,07	20,47
	40-60	1070	25,90	189,14
	20-80	418	10,12	73,36
	0-100	261,1	6,32	45,21
Distiled water/ Roata oil	100-0	41,3	1	1
	80-20	130	3,14	21,00
	60-40	150	3,63	24,82
	40-60	490	11,86	86,19
	20-80	302	7,31	52,59
	0-100	261,1	6,32	45,21
Salt water / Kirkuk oil	100-0	45,5	1,10	2,32
	80-20	54	1,30	4,73
	60-40	80	1,93	10,90
	40-60	367,7	8,91	64,37
	20-80	110	2,66	17,10
	0-100	89,2	2,15	12,86
Salt water/Ochiuri oil	100-0	45,5	1,10	2,32
	80-20	37	0,89	0,22
	60-40	48	1,16	3,06
	40-60	865	20,94	152,80
	20-80	400	9,68	70,14
	100-0	224,0	5,42	38,48

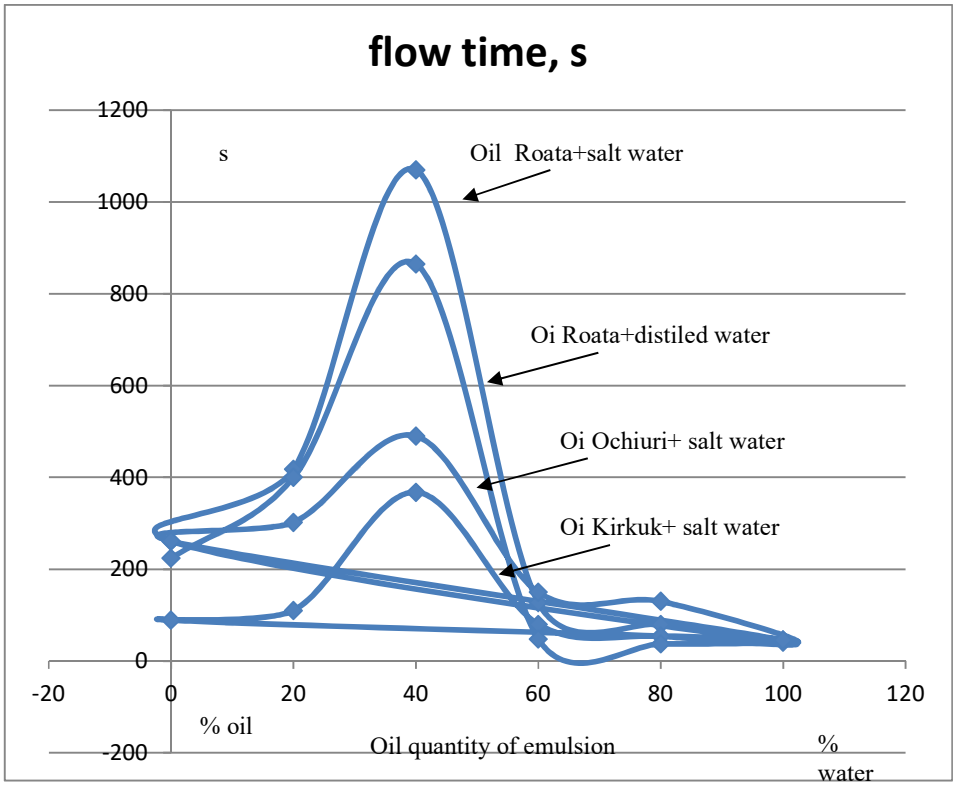

Fig. 1. Variation of viscosity with crude oil content in the emulsion

We compared the obtained data with the previously simulated data, so that we could see the energy consumption per ton for pumping Roata crude oil in the heating variant and in the emulsion delivery variant.

The growing thirst for energy from hydrocarbons leads to the use of all possibilities for the extraction, transport and storage of crude oil from Romanian deposits.

That is why viscous crude oils are extracted to be processed in a mixture with freezable crude oils, in order to obtain low-cost refining products.

Viscous crude oils are also useful in the production of bitumen and that is why their extraction is necessary [4].

This paper analyzes the possibilities of emulsion transport of viscous crude oils (both from the point of view of emulsion stability and especially from the point of view of rheological transport characteristics) [5].

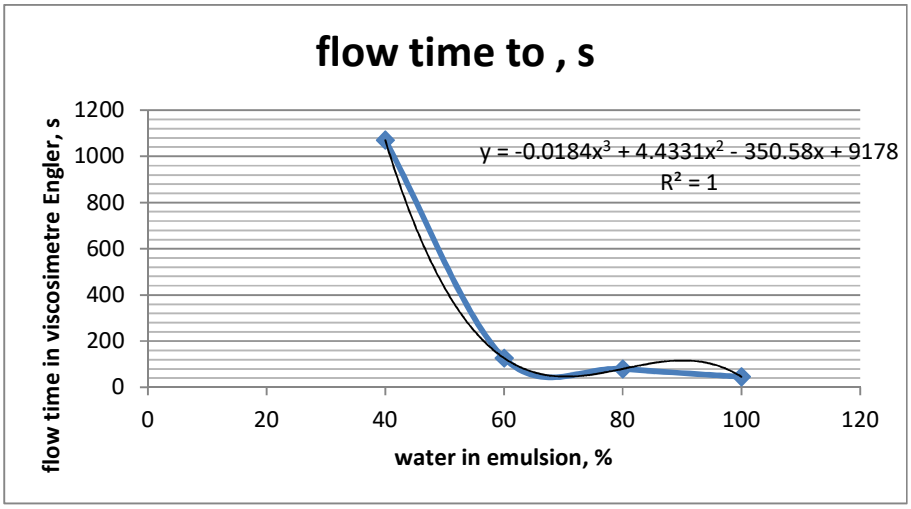

Fig. 2. Relationship between the flow time in seconds of crude oil emulsion in salt water and the amount of water in the emulsion (in percent), Roata Oil

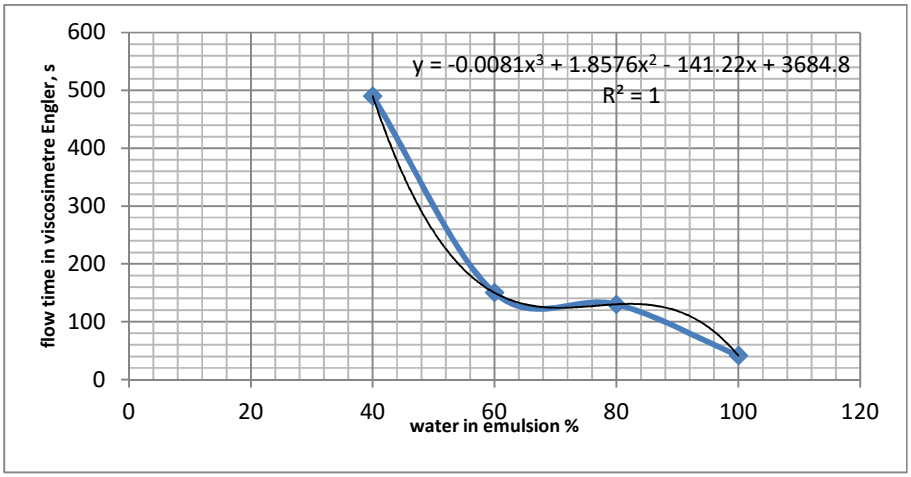

Fig. 3. Relationship between the flow time in seconds of crude oil emulsion in distilled water and the amount of water in the emulsion (in percent)

4. Conclusion

The United States Department of Energy (USA) forecasts an increase in the amount of crude oil in the next 20 years from 60 million barrels per day to 84 million barrels per day [6].

In this context, the oil industry is currently looking for new crude oil deposits and especially the exploitation of unconventional deposits (crude oil stored in clays or sands, crude oil from bituminous shale, etc.).

Solutions are also being sought for the extraction, transport and processing of heavy crude oil (asphaltic and bituminous), which in Romania alone accounts for over 50% of the total crude oil extracted.
In Canada, about 700,000 barrels of crude oil are extracted per day from tar sands and shales.
The decline in medium and light oil reserves and the drop in crude oil prices make the exploitation of heavy (asphaltic) deposits unprofitable using classical methods (solvent extraction, polymer extraction, underground combustion).
Conventional reserves of heavy crude oil are estimated at 6 billion barrels, with Canada, Romania and Venezuela being the main countries that exploit and transport such crude oil through pipelines [7].
That is why over the years various methods have been tried to treat this type of crude oil for transport.
A first option was the heated transport of heavy crude oils, which was difficult to achieve both due to high costs and especially due to technological conditions (separation of water from crude oil after heating, sudden cooling in case of damage, etc.).
Another method often used was mixing with diluents (light crude oils, naphtha, etc.). This process is also unusable due to the deterioration of the quality of the mixed crude oils.
The best solution is to deliver emulsified crude oils because:
a. It does not require heating along the route,
b. Reservoir water can be used as an emulsifier (to be transported to a treatment plant),
c. Energy consumption is greatly reduced, even by 40%,
d. Water-in-crude emulsions can be used for low consumption, but also crude oil-in-water emulsions (only in an 80-20 ratio),
e. It has been observed that asphaltenes have the greatest influence on viscosity, compared to other types of crude oils.
Even though emulsions can create problems in pipeline transport (by separating and settling the water present in the emulsion), currently it is possible to create installations that do not lead to the deposition of water in the roughness of the pipes and therefore this transport is cost-effective and useful.
During this period of time, research is focused on the concentric transport of crude oil mixed with reservoir water.
From the laboratory analyses performed and from the study of the specialized literature, the following conclusions were drawn:
- emulsification leads to a decrease in viscosity only when a mixture ratio of 80-20 and 40-60 water-crude oil is used,
- the data from the specialized literature are confirmed, namely the transport of emulsified crude oil can only be done in an emulsion of the crude oil-in-water type,
- it is also observed that distilled water ensures better emulsification compared to reservoir water,
- it is interesting that at the proportion of 40-60 water in crude oil, the viscosity increases suddenly, beyond the viscosity limits even of the compounds used, this

phenomenon being explained in the specialized literature by the phenomenon of emulsion inversion,

5. Data Availability

The data presented in this article are real and collected from the area of interest. The data can be used by anyone in accordance with applicable international regulations. Data is available in the article and can be provided upon request.

6. Conflicts of Interest

No data or information is presented that could endanger companies or commercial or public companies. There are no conflicts regarding the exposed data. The data taken from the soil samples analyzed and presented in the article are part of oil fields abandoned and handed over to the public domain.

The authors did not benefit from public, private or other resources.

REFERENCES

[1]. Eskin D, Ratuloswski J, Akbarzadeh K, Pan S Modelling asphaltene deposition in turbulent pipeline flows. 2011, Can J Chem Eng 89:421–441,
[2]. Hart A The catalytic upgrading of heavy crude oil in situ: the role of hydrogen. Int J Pet Sci Technol,2012, 6(2):79–96,
[3]. Hasan SW, Ghannam MT, Esmail N Heavy crude oil viscosity reduction and rheology for pipeline transportation. 2010, Fuel 89:1095–1100,
[4]. Hsu C, Robinson P, Practical advances in petroleum processing,2006, vol 1. Springer, New York, pp 1–5,
[5]. Joseph DD, Bai R, Mata C, Sury K, Grant C Self-lubricated transport of bitumen froth.1999, J Fluid Mech 386:127,
[6]. Khan MR, Rheological properties of heavy oils and heavy oil emulsions. Energy Sources, 1996, 18:385–391,
[7]. Lin CY, Chen LW, Emulsification characteristics of three and two phase emulsions prepared by ultrasonic emulsification method. 2006, J Fuel Process Tech 87:309–317.

APPLICATION OF THE GAMMA FUNCTION IN OIL RESERVOIRES POLYMER INJECTION MODELING

Mihai VIRTOPEANU[1], Maria STOICESCU[2*]

[1]Ph.D. School, Petroleum-Gas University
[2]Geological and Oil Engineering, Petroleum-Gas University

Abstract

In this paper we analysis the applicability of the Gamma function in modeling the behavior of polymers injected into reservoirs was studied, having as data for validation the results of the implementation of this process on reservoir X. This reservoir, with well-documented lithological and petrophysical characteristics, provides an adequate framework for testing the validity of theoretical models and for their extrapolation into real operational scenarios. By integrating the Gamma function within advanced modeling, the aim is to obtain a robust analytical tool, capable of contributing to improving technical decisions regarding the selection of operational parameters, the evaluation of recovery efficiency and the prognosis of reservoir performance under polymer injection regime.

Key words: Gamma function, Oil reservoires, Polimer injection

1. Introduction

Enhanced Oil Recovery (EOR) is an essential component in optimizing the recovery factor from mature reservoirs, contributing to extending the economic life of oil fields.

In the context of natural decline in production and increasing economic and environmental pressure, EOR methods are gaining strategic importance in energy resource management.

Among the available EOR technologies, polymer injection has stood out for its efficiency in improving the mobility ratio between the injected fluid and the existing oil in the formation [1].

By increasing the viscosity of the aqueous phase, a more uniform displacement of the oil is ensured and premature channeling phenomena are reduced, which leads to significant additional recovery**.** For the design, control and optimization of this process, it is essential to use mathematical models capable of accurately describing the behavior of polymers in the porous medium. Their transport, dispersion and retention can be described by partial differential equations, whose solutions involve special functions.

In this framework, the Gamma function plays a central role in the formulation and analytical solution of the advection–dispersion equation applied to polymer injection [2].

* Corresponding author: stoicescu.maria@yahoo.com

2. Materials and Methods

The polymer transport process in a fluid-saturated porous medium is governed by advection (movement caused by fluid flow), dispersion (mechanical diffusion due to microscopic heterogeneities of the medium) and, in some cases, adsorption or degradation reactions.

For a homogeneous, isotropic medium without chemical reactions, the transport equation describing the propagation of polymer concentration is [3]:

$$\frac{\partial C}{\partial \mathrm{t}} + \mathrm{v}\frac{\partial C}{\partial \mathrm{x}} = D\frac{\partial^2 C}{\partial x^2} \quad (1)$$

where:

C(x,t), represents the polymer concentration as a function of space (*x*) and time (*t*),

v is the fluid flow velocity,

D is the longitudinal dispersion coefficient.

This equation is known in the specialized literature as the advection–dispersion equation and constitutes the basis for modeling solution transport in porous-permeable media, in soil remediation processes, but also in reservoir engineering, in the case of injection of chemical agents such as polymers.

Under specific conditions, the advection–dispersion equation admits an analytical solution of the gamma distribution type, especially when the injection source is continuous and the initial concentration of the medium is zero.

The analytical solution Gamma is expressed as follows [4]:

$$C(x) = \frac{x^{k-1}e^{\frac{-x}{\theta}}}{\Gamma(\mathrm{k})\theta^k} \quad (2)$$

where: *k* is a shape parameter, related to the structure of the medium and the polymer–rock interaction,

θ is a scale parameter, related to the flow rate and dispersion,

Γ(k) is the Gamma function itself, which generalizes the factorial and is defined as [5]:

$$\Gamma(k) = \int_0^\infty t^{k-1}e^{-t}dt \quad (3)$$

$$\Gamma(k+1) = k\Gamma(k) \quad (4)$$

This function appears naturally in the context of the integration of the differential equation and has the role of normalizing the distribution, ensuring that the total integral of the concentration function is equal to the total amount injected.

The gamma distribution allows the modeling of a wide range of injection front shapes, from fast and concentrated evolutions, to slow and dispersive propagations, depending on the values of the parameters k and θ.

Thus:

- For $k<1$, the distribution is asymmetric and "skewed" towards small values, corresponding to a slow transport, with significant retention.
- For $k=1$, a simple exponential distribution is obtained.

- For k>1, the distribution has a distinct maximum, corresponding to a more homogeneous and faster transport.

The parameter θ controls the width of the distribution and is proportional to the D/v ratio, thus the combined effect of dispersion and flow velocity.

Large values of θ indicate a wide spread of the polymer in space.

Modeling the polymer injection process in an oil reservoir involves integrating the physical parameters of the porous medium, the characteristics of the fluids involved, and the flow conditions imposed by the exploitation regime.

The goal of modeling is to describe, with the highest possible degree of fidelity, how the injected polymer moves through the rock, interacts with the environment, and influences crude oil production.

Starting from the advection–dispersion equation [6]:

$$\frac{\partial C}{\partial \mathrm{t}} + v\frac{\partial C}{\partial \mathrm{x}} = D\frac{\partial^2 C}{\partial x^2} \tag{5}$$

And can apply boundary conditions adapted to the particular case of continuous injection, with a constant concentration at the inlet: $C(0,t)=C_0$; $C(x,0)=0$;

The solution of this problem in the transient regime involves error functions (erf), but in the asymptotic regime (large times) or in heterogeneous environments, generalized Gamma distributions can be used to approximate the polymer propagation front:

This model allows a better adaptation to the real behaviors observed in the field, especially in cases where the polymer front is affected by porosity and permeability heterogeneities.

The parameters k and θ are not chosen arbitrarily, but are determined by calibration methods, starting from:

- experimental data obtained in the laboratory (core flooding tests),
- historical production and reservoir pressure data,
- numerical simulations in modeling environments (e.g. CMG, Eclipse, $TOUGH_2$).

The adjustment methods include nonlinear regressions, genetic algorithms or Bayesian methods.

In practice:

- k is associated with microscopic effects such as pore-throat geometry, adsorption effects or anisotropic dispersion,
- θ is related to the injection rate, effective permeability and polymer viscosity.

An important advantage of the gamma model is the ability to directly incorporate the uncertainty and natural variability of the porous medium, thus providing a more realistic description than classical deterministic models.

The use of the Gamma function instead of classical solutions (based on the error function or on raw numerical solutions) is motivated by:

- the flexibility of the distribution shape: the gamma model can describe asymmetric, steep or diffuse fronts, depending on the value of k,
- the possibility of analytical integration: it allows easy calculation of distributed polymer masses, dislocation rates, etc.,
- the ability to calibrate models based on real data, including for upscaling scenarios from laboratory scale to reservoir scale.

Thus, the model based on the Gamma function becomes a powerful tool in the design, optimization and economic evaluation of polymer injection projects in reservoirs.

3. Results and discussions

Field X is located in the western part of Romania, in the Apuseni Mountains region, within the Zarand Basin.

It is one of the oldest Romanian oil fields, with an exploitation history that dates back to the first half of the 20th century.

The reservoirs are located in Neogene formations, predominantly sandstone, with medium porosity and permeability varying between 10 and 100 mD.

Over time, the field has been subjected to primary and secondary exploitation methods, mainly by water injection. In recent decades, due to the sharp decline in production and the decrease in reservoir pressure, the feasibility of applying EOR methods, in particular polymer injection, has been evaluated as a viable alternative technology.

As part of a pilot project, two productive perimeters in Vața were selected for the implementation of polymer injection.

The polymer used was a high molecular weight polyacrylamide derivative, prepared in concentrations between 500 and 1000 ppm.

The injection regime was continuous, with flow rates between 5 and 15 m^3/day/well, and monitoring was carried out by observing neighboring production wells.

Data collected during injection showed a significant delay in polymer detection at the production wells, followed by a progressive increase in the viscosity of the aqueous phase and an improvement in the oil/water ratio. These observations indicate a complex dispersion phenomenon and a non-uniform spread of the polymer front – aspects that justify the use of a Gamma-type distribution for modeling.

To interpret the spatial spread of the polymer concentration, the following model was used:

$$C(x) = \frac{x^{k-1} e^{\frac{-x}{\theta}}}{\Gamma(k)\theta^k} \quad (6)$$

The model parameters were obtained by fitting to the data from the sampling surveys and concentration measurements:

- k=1,8 (indicating a distribution with a clear maximum, but still slightly asymmetric),
- θ=60 m (indicating moderate dispersion),
- mean relative error of the fitting: below 5%.

The model allowed the estimation of the effective radius of influence of the injection, the identification of areas not covered by the polymer front and the adjustment of the injection regime to optimize the efficiency.

By extrapolation, an increase in the recovery factor of 7–10% compared to simple water injection was estimated, over a period of 3 years.

The integration of the gamma model into the analysis of reservoir X led to:

- a better understanding of the behavior of the polymer in heterogeneous porous media,

- improved decisions regarding the placement of observation wells and injection parameters,

- the possibility of building predictive scenarios in order to extend the injection to other sectors of the reservoir.

The use of the Gamma function has proven to be an effective method of correlating experimental data with real physical behavior, offering a solid alternative to purely numerical simulations and valuable addition to the arsenal of the reservoir engineer.

Here is the plot of the polymer concentration in the reservoir *C(x)* vs. the distance (*x*) of penetration of the polymer solution into the reservoir, which compares different shapes of the Gamma distribution as a function of the parameters *k* and θ, including the calibrated case for reservoir X (*k*=1.8; θ=60).

- The yellow curve (k=1; θ=50) has an exponential shape, typical of simple transport, without significant dispersion.

- The orange curve (k=1.8; θ=60) shows a clear peak and an extended tail – realistic behavior observed in polymer injection at reservoir X.

- The red curve (k=3; θ=70) is more symmetrical, with a more uniform spread – characteristic of more homogeneous media.

This graph helps to compare different injection scenarios and can be integrated into the paper to support the choice of the gamma model.

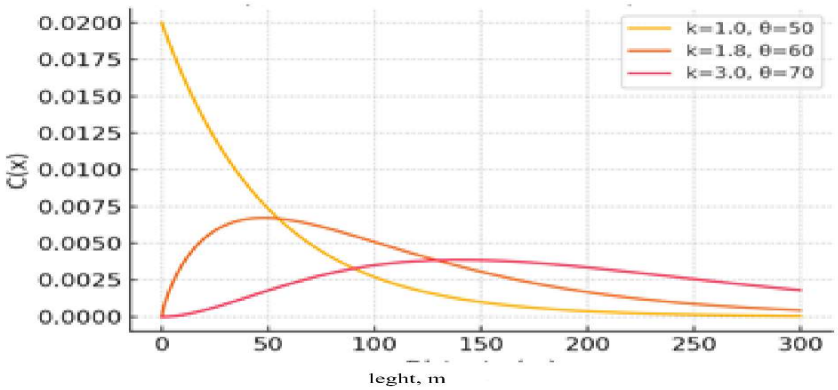

Fig.1. Gama function

The following graph supports the idea that the Gamma function can be a valid tool for modeling polymer transport in a real reservoir.

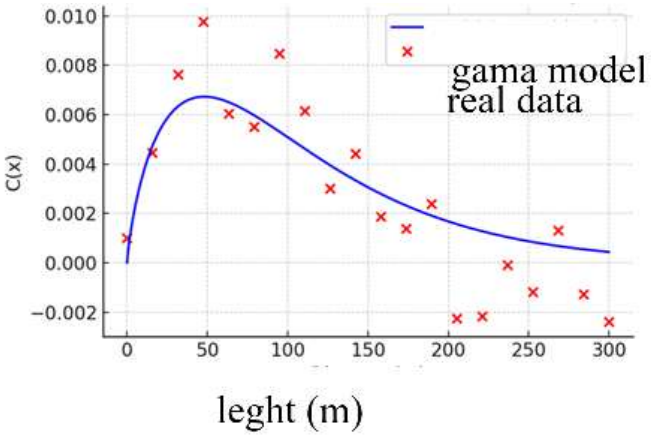

Fig.2. Gamma theoretical model (blue line) and experimental data

The graph represents:

- the calibrated Gamma theoretical model (blue line) and
- the simulated experimental data (red dots) for the observation wells in reservoir X.

A good correspondence between the model and the measured data is observed. Small deviations can be attributed to local variability of the porous medium, measurement errors or adsorption phenomena not explicitly included in the model.

4. Conclusion

The paper demonstrated the applicability of the Gamma function in modeling the polymer injection process in a porous medium representative of a mature oil reservoir.

Starting from the mathematical foundations of the advection–dispersion equation, it was highlighted how the Gamma distribution can be used to approximate the behavior of the polymer concentration in space, taking into account the combined effects of advection, dispersion and medium heterogeneity.

The case study applied to the X reservoir allowed the validation of the model by comparing the theoretical results with real data obtained from observation surveys. The parameters obtained through calibration ($k=1.8$; $\theta=60$) led to a realistic description of the polymer front distribution and provided useful information for optimizing the injection process.

Among the main advantages of using the Gamma model are:

- flexibility in representing various shapes of the concentration distribution;
- possibility of rapid integration into analytical schemes and rapid simulations;
- the ability to fine-tune the model to experimental or field data.

At the same time, this complementary approach to classical numerical simulations allows a clearer conceptual understanding of the physical processes involved

and can serve as a basis for the development of real-time control methods and optimization algorithms.

For further development of this type of modeling, the following can be considered:

• extension of the Gamma model to three-dimensional systems, with radial and vertical variation;
• inclusion of reversible adsorption effects and chemical degradation of the polymer;
• integration into a machine learning framework for automatic calibration on historical data.

Thus, the Gamma function is not just an abstract mathematical tool, but an element with direct applicability in operational decisions of reservoir engineering and in increasing the efficiency of advanced crude oil recovery processes.

5. Data Availability

The data presented in this article are real and collected from the area of interest.

The data can be used by anyone in accordance with applicable international regulations. Data is available in the article and can be provided upon request.

6. Conflicts of Interest

No data or information is presented that could endanger companies or commercial or public companies. There are no conflicts regarding the exposed data. The data taken from the soil samples analyzed and presented in the article are part of oil fields abandoned and handed over to the public domain.

The authors did not benefit from public, private or other resources.

REFERENCES

[1] Lake, L. W. (1989). *Enhanced Oil Recovery*. Prentice Hall.
[2] Shook, G. M., & Lake, L. W. (1995). *Polynomial and power-law solutions to the convection–dispersion equation*. SPE Journal, 10(2), 85–93.
[3] Bear, J. (1972). *Dynamics of Fluids in Porous Media*. Dover Publications.
[4] Gorell, S. B., & van der Poel, C. (1967). *Analytical solutions for polymer flow in porous media*. Journal of Applied Polymer Science, 11(12), 2493–2510.
[5] Peaceman, D. W. (1977). *Fundamentals of Numerical Reservoir Simulation*. Elsevier.
[6] Ravindran, R. K., & Bryant, S. L. (2003). *Use of the gamma distribution to model fluid mixing in porous media*. Transport in Porous Media, 53, 351–369.
[7] Chacón, L., & Lake, L. W. (2006). *Modeling polymer flooding with analytical solutions*. SPE Improved Oil Recovery Symposium.
[8] Abramowitz, M., & Stegun, I. A. (1972). *Handbook of Mathematical Functions*. National Bureau of Standards – Include detalii matematice despre funcția Gamma și funcțiile speciale asociate.

EFFECT OF LASER SURFACE HEAT TREATMENT ON WEAR AND HARDNESS RESISTANCE OF METAL MATRIX COMPOSITE (AL 336.0 ALLOY- Y_2O_3)

Hussein Fawzi HUSSEIN[1,*], Farqad Rasheed SAEED[1], Shaalan Bdaiwi AHMED[1], Iuliana Mihaela DELEANU [2], Murad Majid HUSSEIN[3]

[1] Scientific Research Commission, Baghdad, Iraq
[2] Chemical and Biochemical Engineering Department, Politehnica Bucharest Polizu Str. 1-7, 011061 Bucharest, Romania
[3] Computer Technologies Engineering, AL-Turath University, 10013 Al-Mansour, Iraq

Abstract

Laser surface treatment was applied to enhance the tribological properties of aluminum composite. The study involved varying weight percentages of Y_2O_3 (up to 10 wt%) in a 336.0 aluminum alloy, produced via stir casting. Composites were prepared by adding Y_2O_3 in weight ratios of 2%, 4%, 6%, 8%, and 10% to the aluminum alloy. The effects of laser surface treatment on wear resistance and hardness were examined. Dry sliding wear and micro hardness tests were conducted, and the treated surfaces were analyzed using optical microscopy. Results showed that laser-treated surfaces were free of voids and large cracks. Hardness increased due to the formation of a dense layer in the laser-treated region. Both wear resistance and hardness improved with higher reinforcement percentages, peaking at 6 wt% Y_2O_3 before declining. The treated surface layer exhibited superior tribological properties compared to the untreated surface.

Key words: laser treatment, dry sliding wear, reinforcement

1. Introduction

Metal matrix composites (MMCs) are extensively used in industries due to their high strength-to-weight ratio, toughness, low density, and resistance to harsh environments such as corrosion and high temperatures. However, when MMCs are produced by combining hard reinforcement particles with a metallic matrix, voids often form around the reinforcement due to poor wettability during production [1]. These surface defects, such as irregular textures and voids, degrade material performance and limit their practical applications [2]. High-energy beams, such as lasers, can be used to control surface melting, minimizing defects and potentially improving tribological properties. The laser beam melts the base metal, creating a pool of re-melted material. The microstructure, chemical composition, and porosity of the base material are influenced by the properties of the formed layer [3]. Laser surface treatment can produce a treated layer with thicknesses ranging from less than a millimeter to several millimeters, offering high wear resistance and hardness while preserving the substrate's properties. This technique enables the creation of various material combinations for scientific research

* Corresponding author: Email address: hussein.f.hussein@src.edu.iq

[4]. Recently, laser surface treatment of composite materials has gained attention as a high-functionality technique. By adjusting laser parameters (pulse width, wavelength, and power), the physical and chemical behavior of the surface can be altered, resulting in a uniform surface. Laser treatment offers advantages over traditional methods, including faster processing, precision, cost-effectiveness, and localized treatment [5]. Studies by Gadudasu Babu Rao et al. demonstrated that laser treatment increases hardness by eliminating porosity and refining grain particles [6]. Arvind Sankhla and Kaushik M Patel found that laser treatment improves hardness and wear resistance in aluminum matrix composites [7]. V. Cannillo et al. reported that laser treatment enhances microhardness and tribological properties by improving wettability between reinforcements and the aluminum matrix, filling voids, and increasing strength [8]. Yilbas et al. observed that laser-treated aluminum bronze with B4C exhibited a void-free surface with improved hardness [9].

2. Material Preparation

The aluminum alloy used in this study was sourced from discarded minibus pistons purchased locally. The chemical composition of the alloy was analyzed using an ARL3460 spectrometer, confirming it as 336.0 alloy according to the Aluminum Association standard [10], and as shown in table 1. The pistons were cut into small pieces, cleaned, and melted in a ceramic crucible using a gas furnace. The furnace temperature was maintained at 750°C for 30 minutes to ensure complete melting. Sodium hydroxide (1 wt%) and aluminum chloride (1 wt%) were added to reduce porosity. The molten metal was poured into a cylindrical carbon steel mold to produce ingots for composite preparation.

Table 1.

Chemical Composition of Al-Alloy Mini Bus Piston (ASM, 1992)[10]

Elements	*Si*	*Cu*	*Mg*	*Mn*	*Fe*	*Zn*	*Ti*	*Al*
Standard Alloy	*11-13*	*0.5-1.5*	*1.3 max*	*0.35 max*	*1.2 max*	*0.35 max*	*0.25 max*	*Bal.*
Actual Alloy	*12.5*	*1.19*	*0.8*	*0.23*	*0.5*	*0.08*	*0.07*	*Bal.*

The aluminum alloy used in this study was sourced from discarded minibus pistons purchased locally. The chemical composition of the alloy was analyzed using an ARL3460 spectrometer, confirming it as 336.0 alloy according to the Aluminum Association standard [10], and as shown in table 1. The pistons were cut into small pieces, cleaned, and melted in a ceramic crucible using a gas furnace. The furnace temperature was maintained at 750°C for 30 minutes to ensure complete melting. Sodium hydroxide (1 wt%) and aluminum chloride (1 wt%) were added to reduce porosity. The molten metal was poured into a cylindrical carbon steel mold to produce ingots for composite preparation.

2.1. Al-Mg alloy /Y_2O_3 composite preparation

The Al-Mg alloy / Y_2O_3 composites were prepared by melting 445-485 grams of aluminum alloy with 5 grams of magnesium and varying amounts of Y_2O_3 (10-50 grams) to achieve a total weight of 500 grams according to Table 2. Yttrium oxide powder (99% purity, particle size < 53 microns) was preheated to 350°C to remove moisture and enhance wettability. The aluminum alloy was melted at 750°C for 30 minutes, then cooled to 680°C, and magnesium flakes were added to improve wettability. The preheated Y_2O_3 powder was added in two batches at 630°C and 640°C, with manual stirring. The mixture was heated to 780°C and stirred at 500 rpm for 5 minutes before being poured into a preheated carbon steel mold. The resulting ingots were cooled to room temperature and cut into samples for testing [11, 12].

Table 2.

Al – Mg alloy / Y_2O_3 Composite

Sample No.	***Composition***
Al – Mg alloy	
1	*Al – Mg alloy + Y_2O_3*
2	*Al – Mg alloy + 2 wt.% Y_2O_3*
3	*Al – Mg alloy + 4 wt.% Y_2O_3*
4	*Al – Mg alloy + 6 wt.% Y_2O_3*
5	*Al – Mg alloy + 8 wt.% Y_2O_3*
6	*Al – Mg alloy + 10 wt.% Y_2O_3*

2.2. Laser surface treatment

Laser surface treatment was performed using a fiber laser with an average power of 30W, pulse duration of 120 seconds, frequency of 20 kHz, wavelength of 1064 nm, and a scan speed of 100 mm/s.

2.3. Hardness test

Hardness tests were conducted according to ASTM E384 standards. Cylindrical samples (10 mm height, 12 mm diameter) were prepared, and micro-Vickers hardness was measured using a 490-gram load for 20 seconds. The average of five readings was taken for each sample.

2.4. Wear tests

Wear tests were performed using a pin-on-disc apparatus (Model: ED-201) to measure dry sliding wear. Tests were conducted at loads of 5N, 10N, 15N, and 20N for 15 minutes at 480 rpm. The wear rate was calculated using the weight loss method.

2.5. Microstructure characterization

The microstructure of the composites was examined using an optical microscope (Nikon ME600) with a digital camera. Keller's reagent was used for etching, and X-ray diffraction (Shimadzu XRD-6000) was performed to analyze the phases present.

3. Results and Discussion

3.1. X-ray characterization

X-ray diffraction of the Al-Mg alloy showed distinct peaks for Al, Si, and $FeAl_2$ phases as shown in figure 1. Minor phases included $MgAl_2O_4$, Al_2CuMg, and Al_8Fe_2Si. The addition of Y_2O_3 to the Al-Mg alloy matrix produced intermetallic compounds such as Al_3Y, which is stable below 1253 K. The major phase was aluminum, with minor phases including Al_4MgY, $Al_2Y_4O_9$, Al_3Y, Al_3Mg_2, and $Al_8Si_6Mg_3Fe$.

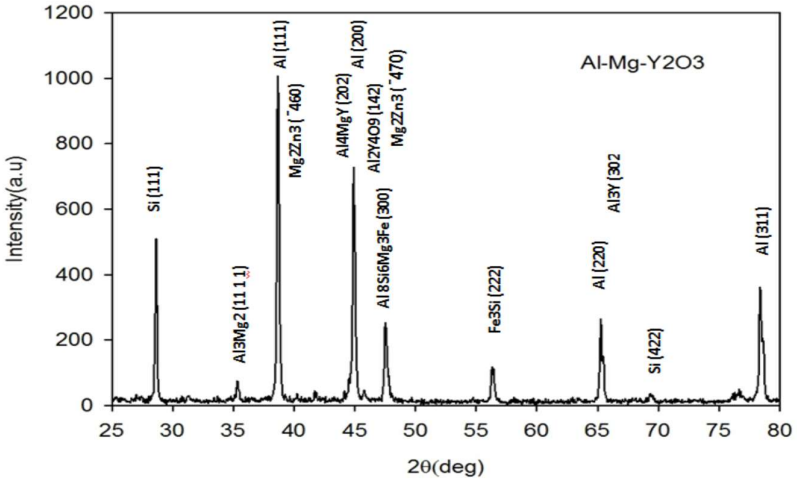

Fig. 1 XRD of Al-Mg Alloy/ Y_2O_3 Composite

3.2. Microstructure of Al-Mg alloy/ Y_2O_3 composite

As Shown in figure 2, the microstructure of the laser-treated composites showed three distinct zones: the base metal, heat-affected zone (HAZ), and molten zone. The molten zone exhibited a fine dendritic structure with uniform Y_2O_3 particle distribution. Agglomeration of Y_2O_3 particles between dendrites resulted in finer dendrite spacing.

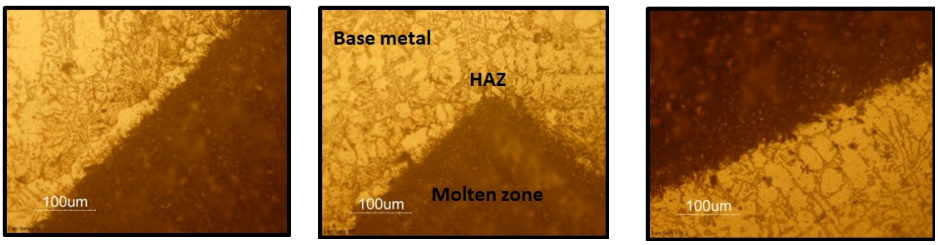

Fig. 2 The surface layer microstructure of composite after laser surface treatment (a) Al-Mg alloy/ 2 wt% Y_2O_3 composite (b) Al-Mg alloy/ 6 wt% Y2O3 composite (c) Al-Mg alloy/ 10 wt% Y_2O_3 composite

3.3. Hardness

The hardness of the Al-Mg / Y_2O_3 composites increased with the addition of Y_2O_3, peaking at 6 wt% before decreasing due to increased porosity. Laser treatment further enhanced hardness by improving bonding between reinforcement particles and the matrix. As illustrated in Table 3.

Table 3.

Results of hardness measurement before and after laser treatment [Average Hardness]

No	Composition of MMC	Untreated MMC	Laser treated MMC	Improvement in hardness
1	Al-Mg / 2% Y_2O_3	38	40	5%
2	Al-Mg / 4% Y_2O_3	43	46	7%
3	Al-Mg / 6% Y_2O_3	49	53	8%
4	Al-Mg / 8% Y_2O_3	45	48	6.6%
5	Al-Mg / 10% Y_2O_3	41	43	4.8%

3.4. Wear Rate

Figures [3, 4] and Table [4] explain that the wear rates increased with higher applied loads for both treated and untreated composites. Laser-treated composites exhibited lower wear rates due to improved bonding and hardness. The minimum wear rate was observed at 6 wt% Y_2O_3, beyond which wear rates increased due to higher porosity.

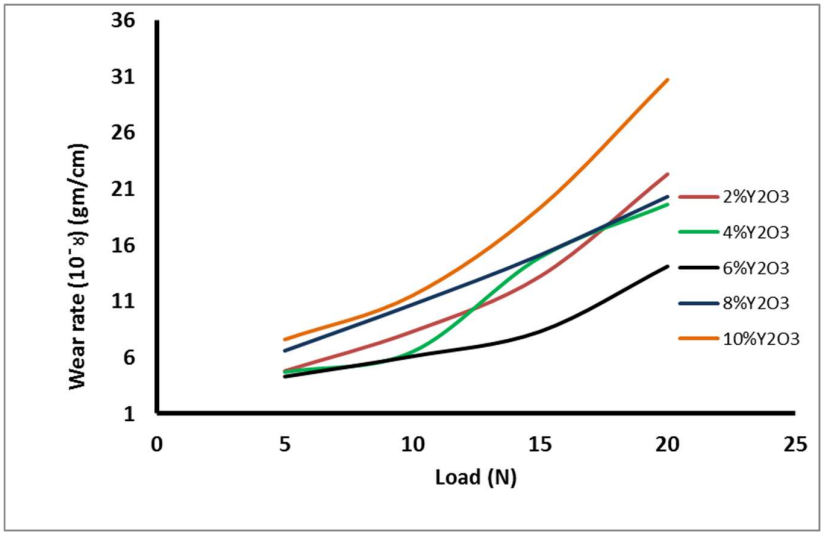

Fig. 3 Variation of wear rate with applied loads for Aluminum composites before laser treatment

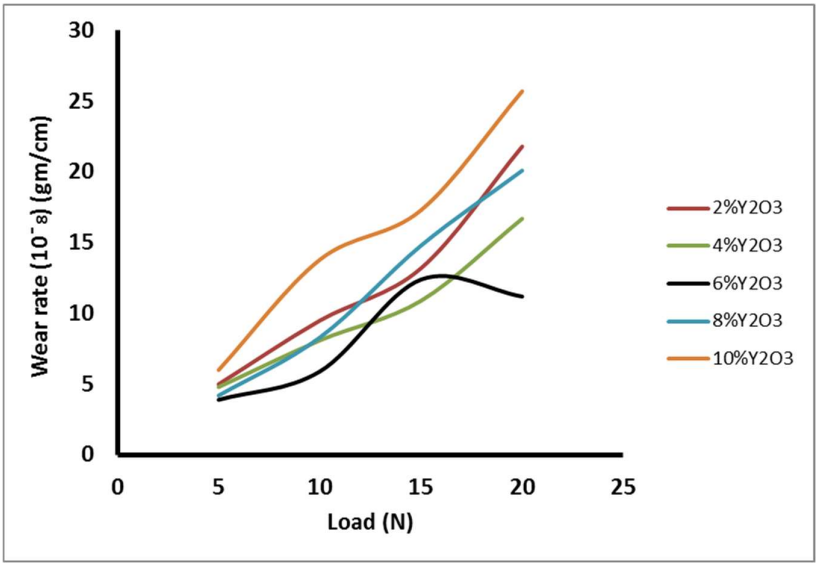

Fig. 4 Variation of wear rate with applied loads for Aluminum composites before laser treatment

Table 4.

Wear rate of Al- Mg alloy/ Y_2O_3 composites before and after laser treatment [Wear Rate (10^{-8}) (gm/cm)]

Sample	Composition of MMC	Laser treated MMC				Untreated MMC			
		5N	10N	15N	20N	5N	10N	15N	20N
1	Al-Mg / 2% Y_2O_3	5	9.5	13.2	21.8	5.3	8.3	19.7	24.3
2	Al-Mg / 4% Y_2O_3	4.8	8.1	10.9	16.7	4.7	6.5	14.9	19.6
3	Al-Mg / 6% Y_2O_3	3.9	5.9	12.4	11.2	4.3	6.1	8.3	14.1
4	Al-Mg / 8% Y_2O_3	4.2	8.3	14.8	20.1	6.6	10.7	15.1	20.3
5	Al-Mg / 10% Y_2O_3	6	13.8	17.3	25.7	7.6	11.5	19.3	30.7

4. Conclusions

The study investigated the effects of laser surface heat treatment on the wear resistance and hardness of aluminum matrix composites reinforced with varying weight percentages of Y_2O_3. The results demonstrated that laser surface treatment significantly improved the tribological properties of the composites. One of the key findings was the uniform distribution of Y_2O_3 reinforcement particles within the aluminum matrix, achieved through the stir casting method. Although some agglomeration of particles was observed, the overall distribution was consistent, contributing to the enhanced mechanical properties of the composites.

Laser surface treatment played a crucial role in improving the hardness of the composites. The formation of a dense, re-melted layer on the surface, free from voids and large-scale cracks, was a major factor in this improvement. The hardness values increased with the addition of Y_2O_3 up to 6 wt%, after which a decline was observed due to increased porosity. This porosity, caused by air entrapment during the casting process, acted as a source of micro-cracks, reducing the overall hardness at higher reinforcement levels. However, the laser-treated samples consistently exhibited higher hardness compared to untreated ones, highlighting the effectiveness of laser treatment in enhancing the bonding between the reinforcement particles and the aluminum matrix.

Wear resistance was another critical property that showed significant improvement after laser treatment. The treated composites exhibited lower wear rates compared to untreated samples, particularly at higher loads. This improvement can be attributed to the formation of a hard surface layer, which reduced friction and localized welding between the mating

surfaces during wear tests. The wear resistance was optimal at 6 wt% Y_2O_3, beyond which the wear rate increased due to the higher porosity and reduced hardness. The laser treatment not only improved the surface hardness but also enhanced the bonding between the reinforcement particles and the matrix, leading to better load transfer and increased wear resistance.

Furthermore, the laser-treated surfaces showed a remarkable reduction in surface defects such as cracks and porosity. This improvement in surface integrity contributed to the enhanced tribological properties of the composites. The fine dendritic structure observed in the molten zone of the laser-treated samples indicated a refined microstructure, which further supported the improved mechanical properties. The heat-affected zone (HAZ) and the base metal also exhibited distinct microstructural changes, contributing to the overall performance of the composites.

In summary, laser surface treatment proved to be an effective method for enhancing the hardness and wear resistance of aluminum matrix composites reinforced with Y_2O_3. The treatment not only improved the surface properties but also minimized defects such as cracks and porosity, leading to better tribological performance. The optimal reinforcement level was found to be 6 wt% Y_2O_3, beyond which the benefits of reinforcement were offset by increased porosity. These findings suggest that laser surface treatment, combined with an appropriate reinforcement ratio, can significantly improve the mechanical and tribological properties of aluminum matrix composites, making them more suitable for industrial applications requiring high wear resistance and hardness.

REFERENCES

[1] Yilbas B. S., Toor I., Malik J., Laser surface treatment of aluminum composite: surface characteristics, Sci. Eng. Compos. Mater., 23(5), 495-503, (2016).
[2] Sroka M., Jonda E., Pakiela W., Laser surface modification of aluminum alloy Al-Mg with B4C powder, Materias, 13, 402, (2020).
[3] Moshayok A. A., Gerashchenkov D. A., Gerashchenkov E. Yu., Davydov V. V., Laser surface treatment of aluminum: correlation between thermal modeling and experimental study, St. Petersburg Polytechnic University Journal: Physics and Mathematics, 15(3.2), (2022).
[4] Li S., Sun T., Liu C., Yang W., Tang Q., A study of laser surface treatment in bonded repair of composite aircraft structure, The Royal Society, (2018).
[5] Yilbas B. S., Karatas C., Karakoc H., Abdul Aleem B. J., Khan S., Al-Aqeeli N., Laser surface treatment of aluminum based composite mixed with B4C particles, Opt. Laser Technol., 65, 129-137, (2015).
[6] Roa G. B., Bannaravuri P. K., Birru A. K., Effect on corrosion behaviour of the surface of aluminum 4.5Cu with bamboo leaf ash composites by laser treatment, Mater. Res. Express, (2020).
[7] Ren Y., Wang L., Li J., Cheng W., Ma X., The surface properties of an aviation aluminum alloy after laser cleaning, Coatings, 12, 273, (2022).
[8] Cannillo V., Sola A., Barletta M., Gisario A., Surface modification of Al-Al_2O_3 composites by laser treatment, Opt. Laser Eng., 48, 1266-1277, (2010).
[9] Yilbas B. S., Matthews A., Leyland A., Karatas C., Akhtar S. S., Aleem B. J., Laser surface modification treatment of aluminum bronze with B4C, Appl. Surf. Sci., 263, 804-809, (2012).
[10] ASM Handbook, Nonferrous Alloys and Special-Purpose Materials, Vol. 2, ASM International, (1992).
[11] Prasad D. S., Krishna A. R., Production and mechanical properties of A356.2/RHA composites, Int. J. Adv. Sci. Technol., 33, 51-58, (2011).

[12] Alaneme K. K., Adewale T. M., Influence of rice husk ash–silicon carbide weight ratios on the mechanical behavior of Al-Mg-Si alloy matrix hybrid composites, Tribol. Ind., 35(2), 163-172, (2013).
[13] ASM Handbook, Mechanical Testing and Evaluation, Vol. 8, ASM International, (2000).
[14] Prasad N., Sutar H., Mishra S. Ch., Sahoo S. K., Acharya S. K., Dry sliding wear behavior of aluminum matrix composite using red mud an industrial waste, Int. Res. J. Pure Appl. Chem., 3(1), 59-74, (2013).
[15] Bouaeshi W. B., Li D. Y., Effects of Y_2O_3 addition on microstructure, mechanical properties, electrochemical behavior, and resistance to corrosive wear of aluminum, Tribol. Int., 40, 188-199, (2007).
[16] Hashim J., Looney L., Hashmi M. S. J., Metal matrix composites: production by the stir casting method, J. Mater. Process. Technol., 92-93, 1-7, (1999).
[17] Prasad D. S., Shoba Ch., Ramanaiah N., Investigation on mechanical properties of aluminum hybrid composites, J. Mater. Res. Technol., 3(1), 79-85, (2014).
[18] Aigbodion V. S., Development of Al-Si-Fe/Rice husk ash particulate composites synthesis by double stir casting method, Usak Univ. J. Mater. Sci., 2, 187-197, (2012).
[19] Sankhla A., Patel K. M., Experimental investigations on effect of surface treatment of aluminum based metal matrix composites using laser, J. Phys.: Conf. Ser., (2021).
[20] Sharma R., Sharma P., Singh G., Dry sliding behavior of aluminium alloy reinforced with hybrid ceramic particles, Int. J. Multidiscip. Res. Dev., 2(10), 485-491, (2015).
[21] Prasad D. S., Krishna A. R., Tribological properties of A356.2/RHA composites, J. Mater. Sci. Technol., 28(4), 367-372, (2012).

VALORIZATION OF LIVESTOCK AND POULTRY MANURE THROUGH BIOCHAR PRODUCTION AND ITS AGRICULTURAL APPLICATIONS

Zhong CUI[1,2*], Alexandru OZUNU[2], Jun MENG[1]

[1] Institute of Eco-environmental Research, School of Environmental and Natural Resources, Zhejiang University of Science & Technology, Hangzhou 310023, China
[2] Babeş-Bolyai University of Cluj-Napoca, Faculty of Environmental Science and Engineering, Doctoral School of Environmental Science - 30 Fantanele Street, RO-400294, Cluj-Napoca, Romania.

Abstract

Livestock and poultry manure is an abundant by-product of intensive farming, but its improper disposal often leads to nutrient loss and environmental pollution. Converting manure into biochar through thermal treatment provides an effective green-chemistry pathway for resource valorization. In this study, manure-derived biochars were prepared by slow pyrolysis at different temperatures (300-700 °C), and their physicochemical characteristics and agricultural benefits were evaluated. Results showed that pyrolysis temperature strongly affected biochar pH, ash content, and specific surface area. Higher temperatures increased carbon stability but reduced nitrogen content, while moderate temperatures (400-500 °C) produced biochar with balanced nutrient retention and surface functionality. When applied to acidic soils, manure biochar significantly increased soil pH, cation exchange capacity (CEC), and available phosphorus, leading to better plant growth and yield compared with untreated soil. Moreover, biochar application reduced the mobility of heavy metals and enhanced soil carbon sequestration potential. Overall, manure-derived biochar represents a sustainable strategy for nutrient recycling, soil improvement, and waste reduction in agriculture. Future work should optimize pyrolysis conditions and field application rates to achieve stable agronomic performance and minimize potential risks.

Key words: Manure; Biochar; Pyrolysis, Soil Fertility, Nutrient Recycling, Sustainable Agriculture

1. Introduction

The global livestock and poultry sector is a cornerstone of food security, yet it generates enormous quantities of manure. In the EU, about 1.3–1.8 billion tonnes (wet weight) of manure is produced each year [1]. This discharge needs to be urgently disposed of to mitigate its environmental and ecological impact (Fang et al., 2018). Historically, this nutrient-rich resource was directly applied to farmland. The use of commercial additives in feeds has increased due to the antibacterial properties, improved feeding efficiency, and promotion of animal growth [2]. However, commercial fertilizer is usually rich in heavy metals (HMs) that are poorly absorbed, with more than 95%

∗ Corresponding author: Email address: Zhonghua.cui@ubbcluj.ro

excreted into the environment via stool and urine [4]. Therefore, manure contains a high concentration of organic matter (OM), pathogens, and toxic HMs (HMs, e.g., Cu, Cd and Zn) that pose risks to human health and the environment with improper handling and application [5]. Thus, the treatment and disposal of waste and the development of practical and efficient waste treatment technologies have become key concerns attracting scientific attention. For the moment, anaerobic digestion and aerobic composting has been commonly used to dispose animal manure. Nevertheless, after being treated by above two methods, organic pollutants and pathogens cannot be completely eliminated, and heavy metal bioavailability is still high [6]. Therefore, more effective measures are urgent for proper reutilization of animal manure.

In the quest for sustainable waste management strategies, the concept of a circular bioeconomy has gained prominence, aiming to transform waste into valuable resources. In this context, the thermochemical conversion of biomass into biochar through pyrolysis has emerged as a leading-edge solution. Biochar is attracting increasing attention due to its potential benefits in improving soil fertility, remediating polluted soils [7] and sequestering carbon for long-term [8] and wastewater treatment.

While extensive research has been conducted on biochar from lignocellulosic biomass (e.g., wood, crop residues), manure-derived biochars present unique characteristics due to their high nutrient and ash content. The conversion of manure to biochar effectively addresses several challenges simultaneously: it reduces waste volume, eliminates pathogens and odor, stabilizes carbon, and concentrates most nutrients into a more plant-available and slow-release form[9]. This review aims to synthesize the current state of knowledge on the valorization of livestock and poultry manure through biochar production. It will elaborate on the production process, the critical role of pyrolysis conditions in tailoring biochar properties, and the subsequent agronomic and environmental benefits of its application, concluding with perspectives on future research needs.

2. Production of Manure-Derived Biochar and The Role of Pyrolysis Conditions

The properties and functionality of biochar are predominantly determined by the feedstock and the pyrolysis parameters, with temperature being the most influential factor. Slow pyrolysis is the most common method for producing manure-based biochar, characterized by heating the feedstock (typically dried and ground) to a target temperature (300-900 °C) under oxygen-limited conditions with a slow heating rate and a long solid residence time. This process maximizes the solid biochar yield while producing liquid (bio-oil) and gaseous by-products.

A substantial body of literature confirms that pyrolysis temperature fundamentally shapes the physicochemical properties of manure-derived biochar[10,11]. The following trends are consistently observed: pH and Ash Content: Biochar pH increases markedly with rising pyrolysis temperature. This is attributed to the enrichment of alkaline functional groups and the formation of inorganic carbonates and oxides within the ash fraction. The ash content itself also increases as volatile organic matter is driven off, concentrating the inherent minerals present in the manure[12].

Surface Area and Porosity: Low-temperature biochars (e.g., <400 °C) typically possess a low specific surface area (SSA). As the temperature increases (500-700 °C), the decomposition of volatile matter and the development of microporous structures lead to a significant expansion of SSA, which is crucial for adsorption capacity.

Nutrient Composition and Stability: The fate of nutrients during pyrolysis is a critical consideration. While carbon is progressively condensed into a stable aromatic structure, nitrogen is highly volatile. Studies show that nitrogen recovery in the solid biochar decreases substantially with increasing temperature, with significant losses as NH_3 and HCN gases [13]. In contrast, phosphorus and potassium are effectively retained and concentrated in the ash, often in more plant-available forms. The carbon stability, indicated by a lower H/C and O/C atomic ratio, increases at higher temperatures, enhancing its carbon sequestration potential.

Surface Functionality: Fourier Transform Infrared (FTIR) spectroscopy studies reveal that biochars produced at lower to moderate temperatures (300-500 °C) retain a greater density of oxygen-containing functional groups (e.g., carboxyl, hydroxyl, carbonyl) on their surfaces. These functional groups are vital for cation exchange capacity (CEC) and interactions with soil microbes and contaminants.

This temperature-dependent property trade-off suggests that an "optimal" temperature does not exist universally but depends on the primary application goal. For instance, a biochar intended primarily as a liming agent and nutrient source might be best produced at 400-500°C, while one aimed at pollutant adsorption or maximum carbon sequestration would benefit from higher temperatures (>600°C).

3. Agricultural Applications and Benefits

The application of manure-derived biochar to soil offers a suite of interconnected benefits, transforming it from a waste product into a powerful soil amendment.

3.1. Soil Amendment and Fertility Enhancement

Soil pH Amelioration: The alkaline nature of most manure biochars makes them highly effective liming agents for acidic soils. Their application consistently raises soil pH, which in turn can reduce aluminum toxicity and increase the availability of essential nutrients like phosphorus and molybdenum [14].

Improved Nutrient Retention and Availability: Biochar enhances the soil's CEC, allowing it to retain more cationic nutrients (e.g., NH_4^+, K^+, Ca^{2+}, Mg^{2+}), reducing leaching losses. Furthermore, the direct addition of nutrients, especially phosphorus and potassium, from the biochar itself provides a valuable nutrient source for crops.

Enhanced Soil Physical and Biological Properties: The incorporation of porous biochar can improve soil structure, water-holding capacity, and aeration. This improved habitat, coupled with the provision of a carbon source, can stimulate the activity and diversity of beneficial soil microorganisms [15].

3.2. Plant Growth and Yield

Numerous pot and field studies have reported increased plant growth and yield following the application of manure biochar. These positive effects are typically attributed to the combined improvements in soil physical, chemical, and biological properties mentioned above. The growth promotion is often more pronounced in degraded, acidic, or nutrient-poor soils.

3.3. Environmental Remediation and Safety

Heavy Metal Immobilization: Manure can contain traces of heavy metals (e.g., Cu, Zn, As) from animal feed. Pyrolysis can concentrate these metals in the biochar. However, the resulting biochar often possesses a strong capacity to immobilize these and other soil contaminants through mechanisms such as precipitation, surface complexation, and adsorption, thereby reducing their bioavailability and uptake by plants[16].

Pathogen Reduction: The high temperatures involved in pyrolysis (>400°C) effectively eliminate pathogens and weed seeds present in raw manure, mitigating a significant risk associated with direct land application.

3.4. Carbon Sequestration and Climate Change Mitigation

By converting labile organic carbon in manure into a highly stable aromatic form, biochar production creates a carbon sink. When applied to soil, this stable carbon can persist for centuries to millennia, thereby contributing to the mitigation of atmospheric CO_2 levels [17]. The exceptional stability of biochar carbon stems from the thermochemical transformation during pyrolysis. Raw manure contains organic carbon in labile forms (e.g., cellulose, hemicellulose, and other volatile compounds) that are readily decomposed by soil microorganisms, leading to the rapid release of CO_2 or, under anaerobic conditions, methane (CH_4) a greenhouse gas with a global warming potential 28-36 times that of CO_2 over 100 years. Pyrolysis fundamentally alters this carbon structure. As the temperature increases, the biomass undergoes a series of reactions including dehydration, depolymerization, and aromatization.

The carbon sequestration potential of manure biochar is twofold: Waste Stream Diversion: By converting manure to biochar, the natural decomposition pathway that would release CO_2 and CH_4 is interrupted. This avoids the "default" greenhouse gas emissions associated with manure storage and land application. Positive Carbon Addition: The stable carbon in biochar is added to the soil, creating a net gain in the terrestrial carbon stock. While the carbon sequestration efficiency (percentage of feedstock carbon converted into stable biochar carbon) varies, it is significantly higher than composting or direct application. Studies suggest that over 50% of the initial carbon in the feedstock can be fixed into a stable form through slow pyrolysis, compared to only 10-20% that may remain after a few years in a composted system [18].

Beyond direct carbon sequestration, the application of manure biochar can indirectly reduce emissions of other potent greenhouse gases from agricultural soils. Reduction of Nitrous Oxide (N_2O) Emissions: N_2O is a major GHG with a global

warming potential approximately 265-298 times that of CO_2. Agricultural soils are a primary source, largely due to nitrogen fertilization. Biochar can suppress N_2O emissions through several mechanisms: Aeration: Improving soil porosity and reducing water-filled pore space, which discourages the anaerobic conditions favorable for denitrification (a major N_2O-producing process). Adsorption: Retaining NH_4^+ and NO_3^- ions on its surface, making them less available for microbial nitrification and denitrification processes. Altering Microbial Communities: Shifting the microbial population towards N_2O-reducing bacteria that convert N_2O into inert N_2 gas[19]. Reduced CH_4 Emissions from Soils: In well-aerated soils, biochar application has been shown to reduce methanogenesis (CH_4 production) by improving drainage and oxygen availability. Furthermore, methanotrophic bacteria (CH_4 consumers) can colonize the biochar's porous structure, potentially enhancing CH_4 oxidation.

The pyrolysis process is not only about producing biochar; it is a integrated biorefinery concept. The syn-gas and bio-oil co-produced can be captured and used as renewable energy sources to offset fossil fuel consumption, creating a net negative carbon emission technology. A Life Cycle Assessment (LCA) of manure management systems often reveals that the biochar pathway has a significantly lower global warming potential compared to conventional practices like composting, anaerobic digestion, or stockpiling, due to the combined benefits of avoided emissions, carbon sequestration, and fossil fuel displacement [20].

4. Challenges and Future Perspectives

Despite the promising potential, several challenges and research gaps remain before the widespread adoption of manure-derived biochar can be realized.

Optimization and Standardization: There is a need to develop tailored pyrolysis protocols for different manure types to produce "designer biochars" with specific properties for targeted applications (e.g., nutrient-focused vs. remediation-focused).

Long-Term Field Studies: Most evidence comes from short-term laboratory or greenhouse studies. Long-term, large-scale field trials are essential to validate the agronomic benefits, understand the aging process of biochar in soil, and assess its long-term impact on soil ecosystems.

Risk Assessment and Life Cycle Analysis (LCA): A comprehensive assessment of potential risks, including the long-term stability of immobilized heavy metals and the emission of particulate matter during production, is necessary. Furthermore, LCA studies are needed to quantitatively evaluate the net environmental benefits of the entire manure-to-biochar system compared to conventional management practices.

Economic Viability and Policy Support: The economic feasibility of centralized or on-farm biochar production systems needs to be improved. Supportive policies and carbon credit mechanisms could play a pivotal role in incentivizing this technology.

5. Conclusions

The valorization of livestock and poultry manure through biochar production represents a paradigm shift from waste disposal to resource creation. This review underscores that pyrolysis temperature is a master lever for controlling the properties of manure biochar, allowing for customization based on intended use. The application of this material in agriculture offers a synergistic solution to multiple challenges: it improves soil health and fertility, enhances crop productivity, reduces environmental pollution, and contributes to climate change mitigation through carbon sequestration. While technical challenges remain, the integration of manure-derived biochar into agricultural systems holds immense promise for building more sustainable, productive, and resilient farming practices in a circular economy framework. Future research should focus on bridging the gap between laboratory promise and field-scale reality to unlock the full potential of this transformative technology.

REFERENCES

[1]J. De Vrieze, G. Colica, C. Pintucci, J. Sarli, C. Pedizzi, G. Willeghems, A. Bral, S. Varga, D. Prat, L. Peng, M. Spiller, J. Buysse, J. Colsen, O. Benito, M. Carballa, S.E. Vlaeminck, Resource recovery from pig manure via an integrated approach: A technical and economic assessment for full-scale applications, Bioresource Technology 272 (2019) 582–593.

[2]M.K. Awasthi, Y. Duan, S.K. Awasthi, T. Liu, H. Chen, A. Pandey, Z. Zhang, M.J. Taherzadeh, Emerging applications of biochar: Improving pig manure composting and attenuation of heavy metal mobility in mature compost, Journal of Hazardous Materials 389 (2020) 122116.

[3]H. Fang, L. Han, H. Zhang, Z. Long, L. Cai, Y. Yu, Dissemination of antibiotic resistance genes and human pathogenic bacteria from a pig feedlot to the surrounding stream and agricultural soils, J Hazard Mater 357 (2018) 53–62.

[4]Y. Yin, J. Gu, X. Wang, K. Zhang, T. Hu, J. Ma, Q. Wang, Impact of copper on the diazotroph abundance and community composition during swine manure composting, Bioresource Technology 255 (2018) 257–265.

[5]J. Meng, S. Liang, M. Tao, X. Liu, P.C. Brookes, J. Xu, Chemical speciation and risk assessment of Cu and Zn in biochars derived from co-pyrolysis of pig manure with rice straw, Chemosphere 200 (2018) 344–350.

[6]N. Wu, S. Xie, M. Zeng, X. Xu, Y. Li, X. Liu, X. Wang, Impacts of pile temperature on antibiotic resistance, metal resistance and microbial community during swine manure composting, Science of The Total Environment 744 (2020) 140920.

[7]L. He, H. Zhong, G. Liu, Z. Dai, P.C. Brookes, J. Xu, Remediation of heavy metal contaminated soils by biochar: Mechanisms, potential risks and applications in China, Environmental Pollution 252 (2019) 846–855.

[8]S. Majumder, S. Neogi, T. Dutta, M.A. Powel, P. Banik, The impact of biochar on soil carbon sequestration: meta-analytical approach to evaluating environmental and economic advantages, Journal of Environmental Management 250 (2019) 109466.

[9]Q. Liu, L. Huang, Z. Chen, Z. Wen, L. Ma, S. Xu, Y. Wu, Y. Liu, Y. Feng, Biochar and its combination with inorganic or organic amendment on growth, uptake and accumulation of cadmium on lettuce, Journal of Cleaner Production 370 (2022) 133610.

[10]W.-T. Tsai, C.-N. Huang, H.-R. Chen, H.-Y. Cheng, Pyrolytic Conversion of Horse Manure into Biochar and Its Thermochemical and Physical Properties, Waste Biomass Valor 6 (2015) 975–981.

[11]X. Shen, J. Zeng, D. Zhang, F. Wang, Y. Li, W. Yi, Effect of pyrolysis temperature on characteristics, chemical speciation and environmental risk of Cr, Mn, Cu, and Zn in biochars derived from pig manure, Science of the Total Environment 704 (2020) 135283.

[12]S. Caro, O. Dahl, Thermochemical valorisation of waste: Pyrolytic conversion of horse manure, Cleaner Engineering and Technology 4 (2021) 100181.
[13]H. Xia, M. Riaz, M. Zhang, B. Liu, Y. Li, Z. El-Desouki, C. Jiang, Biochar-N fertilizer interaction increases N utilization efficiency by modifying soil C/N component under N fertilizer deep placement modes, Chemosphere 286 (2022) 131594.
[14]M.A.-A. Baquy, J.-Y. Li, J. Jiang, K. Mehmood, R.-Y. Shi, R.-K. Xu, Critical pH and exchangeable Al of four acidic soils derived from different parent materials for maize crops, J Soils Sediments 18 (2018) 1490–1499.
[15]S. Bolan, D. Hou, L. Wang, L. Hale, D. Egamberdieva, P. Tammeorg, R. Li, B. Wang, J. Xu, T. Wang, H. Sun, L.P. Padhye, H. Wang, K.H.M. Siddique, J. Rinklebe, M.B. Kirkham, N. Bolan, The potential of biochar as a microbial carrier for agricultural and environmental applications, Science of The Total Environment 886 (2023) 163968.
[16]J. Major, M. Rondon, D. Molina, S.J. Riha, J. Lehmann, Maize yield and nutrition during 4 years after biochar application to a Colombian savanna oxisol, Plant Soil 333 (2010) 117–128.
[17]K.N. Shoudho, T.H. Khan, U.R. Ara, M.R. Khan, Z.B.Z. Shawon, M.E. Hoque, Biochar in global carbon cycle: Towards sustainable development goals, Current Research in Green and Sustainable Chemistry 8 (2024) 100409.
[18]N. Blenis, N. Hue, T.M. Maaz, M. Kantar, Biochar production, modification, and its uses in soil remediation: A review, Sustainability 15 (2023) 3442.
[19]I. de Oliveira Paiva, E.G. de Morais, K. Jindo, C.A. Silva, Biochar N content, pools and aromaticity as affected by feedstock and pyrolysis temperature, Waste Biomass Valor 15 (2024) 3599–3619.
[20]J. Li, W. Sun, E. Lichtfouse, C. Maurer, H. Liu, Life cycle assessment of biochar for sustainable agricultural application: A review, Science of The Total Environment 951 (2024) 175448.